The synthesis, characterization, and electrochemical analysis of structured polymer electrolytes having strong ionic interactions

Sebastian Thomas Russell

Submitted in partial fulfillment of the
requirements for the degree of
Doctor of Philosophy
of the Graduate School of Arts and Sciences

COLUMBIA UNIVERSITY

2020

Abstract

The synthesis, characterization, and electrochemical analysis of structured polymer electrolytes having strong ionic interactions

Sebastian Thomas Russell

Polymer electrolytes, ionic monomers catenated into a macromolecule, have received a considerable attention in the past decade as they combine the mechanical benefits of flexible chain with the ionic properties of liquid electrolytes. For this reason, they have been widely accepted as potential ion conducting membrane candidates for electrolyzers, energy storage devices, and desalination applications. In efforts to improve the efficiency of polymer electrolyte separators a block copolymer paradigm has been employed. This material's strategy allows for a spatial separation of the components that control the mechanical and electrochemical properties and thus enables independent engineering of each. Charge – neutral block copolymers (CN-BCPs), a diblock copolymer containing a polyelectrolyte block, attempt to leverage this paradigm, however, to date, the impact ions have on the CN-BCP self-assembly is still an open question. In this dissertation, we are devoted to uncovering the fundamental impact of ionic interactions on CN-BCP self-assembly in bulk and thin-films. First, we survey the literature and compile a list of thoroughly investigated CN-BCPs (derived from imidazolium, quaternary ammonium, and phosphonium motifs) with known dielectric properties. The ionic interaction strength for each CN-BCP was determine using the polyelectrolyte block's static dielectric constant (ε_r) and the definition of the Bjerrum length ($l_B = e^2/4\pi\varepsilon_0\varepsilon_r k_b T$). The CN-BCPs studied in the literature, copolymers containing polyelectrolytes blocks with a high ε_r, display a morphology diagram akin

to what is expected from the traditional block copolymer self-assembly. However, using a suite of experiment characterization techniques we show that CN-BCPs that contain a polyelectrolyte block with a low static dielectric constant ($\varepsilon_r = 2.5$) produce an asymmetric morphology diagram. In this case, we find morphologies that would assemble the polyelectrolyte block into a discrete phase are suppressed if not completely absent. To explain this usual result, we invoke a simple free energy argument, geometric analysis, and a packing parameter model derived from small molecule surfactant principles to rationalize the asymmetry in the morphology diagram on a basis of long-range ionic correlations. Utilizing the packing parameter model we were able to quantitively capture the morphology diagrams of all known CN-BCPs using a single interaction energy parameter. Next, we explore the impact of film thickness on CN-BCP self-assembly via solvent vapor annealing thin-films. A complimentary CN-BCP morphology diagram is constructed for a constant film thickness ($h = 40$ nm) and compared to the bulk phase behavior. Similar to the bulk morphology mapping, we found an asymmetric thin-film morphology diagram with only a singular ordered morphology – cylinders. The influences of film confinement are discussed and utilized to reversibly switch the CN-BCP domain orientation on demand. Finally, we use *in-situ* grazing incidence small angle x-ray scattering to explore the CN-BCP thin-film structural evolution during the solvent vapor annealing process. We find quantitively different processing pathways when nonselective or selective solvents are used to vapor anneal CN-BCPs. A wide range of annealing solvents spanning a $\varepsilon_r = 4.8 - 32.7$ range was chosen to vapor anneal CN-BCP thin films and a relationship between CN-BCP periodicity (d) and ε_r was determined. We find $d \sim 1/\sqrt{\varepsilon}$ relationship suggesting the CN-BCP periodicity can be engineer by choice of annealing solvent.

Additionally, in this dissertation, we explore the broader impact of morphology on the ion transport through polymer electrolyte membranes. In this vien, we propose structure – property relationships that will enable a rational design of single-ion conducting separators. Using in-house electrochemical techniques, nanoindentation, and gravimetric analysis we explore the relationship between ionic selectivity, quantified through the counterion transference number (t_c^m), the ionic conductivity (κ), and the separator hardness with respect to separator water volume fraction (ϕ_{H_2O}). We find t_c^m increases with increasing separator swollen-state charge density which is consistent with a donnan repulsion perspective. Additionally, as ϕ_{H_2O} increases we find κ increases by orders of magnitude indicting that hydration plays an intimate role in improving ion diffusion in polymer electrolytes. Finally, we present a summary of the permselectivity, $\Psi^m = (t_c^m - t_c^{aqu})/(1 - t_c^{aqu})$, where $t_c^{aqu}$is equivalent to the aqueous transference number, to κ for a series of polymer electrolytes characterized in literature. We find that separators derived from polymers with rigid backbones (*e.g.* poly(phenyl sulfone) and poly(2,6-dimethyl-1,4-phenylene oxide)) tend to have a small tradeoff between Ψ^m and κ yet cannot access ideal counterion selectivity ($\Psi^m = 1$) when $\kappa \to 0$. As the backbone flexibility increases the $\Psi^m - \kappa$ tradeoff is more dramatic yet a $\Psi^m = 1$ when $\kappa \to 0$ is recovered suggesting the importance of molecular packing in this regime. We thus conclude that designing separators with an ideal $\Psi^m - \kappa$ relationship will require a simultaneous manipulation of molecular architecture, separator hydration state, and morphology.

Table of Contents

List of Figures

List of Tables

Acknowledgments

First and foremost, I would like to express my utmost gratitude to my advisor Prof. Sanat Kumar for the incredible opportunity to work in his research group. Over the course of my Ph.D., Prof. Kumar has continuously supported my development and provided me the strength the push forward when times were tough. Prior to my graduate career a Columbia University, I suffered a major knee accident that abruptly ended my career as a division 1 athlete and detrimentally impacting my studies. Prof. Kumar took a chance taking me under his wing and I will forever be in his debt for allowing me to pursue a doctoral degree in his group. In his group, I received an incredible training in polymers science and met some of the greatest people I know. Prof. Kumar for carrying me through some very difficult times during my Ph.D. including a lab accident and another major knee surgery that turned into a serious staph infection. I lost almost a year of work due to the hospitalization, antibiotic treatments, and rehabilitation, so it is fair to say that I did not make things easy and thank you very much for pushing me to the finish line.

I had an additional benefit of having incredible co-advising from Prof. Luis M. Campos and Prof. Alan C. West. Coming to Columbia, I had practically no experience in synthetic organic chemistry or electrochemistry, so I cannot begin to express how much I appreciate their patience with me over the past five years. I want to especially thank Prof. Campos for his support, guidance, and flexibility to allow me to work in his labs to learn polymer synthesis. Coming to Columbia, one of goals was to develop some synthetic tools and, through working in his group, I received much more than I had ever anticipated. As for Prof. West, I still remember you gave me the hardest question on my qualifying exam which of course I was unable to answer, and I really want to thank you for always pushing me to see the big picture questions in my research. Looking back now, taking your class in the fall semester second year altered the course of my Ph.D. and sparked an

incredible collaboration. I really want to thank Prof. West, from the bottom of my heart, for all the support, mentorship, and guidance throughout the past five years, and for your interest in pursuing research endeavors in polymers.

I want to thank my other committee members, Prof. Kyle Bishop and Prof. Oleg Gang, despite their busy schedules they were able to make time to participate on my thesis defense committee. I would also like to especially Prof. Oleg Gang for teaching me surfactant self-assembly theory and helping acquire the tools I needed to publish my first manuscript. Additionally, I want to thank Prof. Christopher Durning and Prof. Jeffery Koberstein for teaching polymer courses at Columbia and passing on pieces of their vast knowledge in the field to me. Prior to starting my Ph.D. Prof. Koberstein took me on as a summer student in his research lab to investigate the lower critical solution temperature of polyacetals. This was my first experience in polymer physics research and under his tutelage I developed a passion for the field. Thank you, Prof. Koberstein, for your mentorship and helping approach research topics with a critical lens.

I also want to give a special thanks to Prof. Triantafillos Mountzaris and Prof. Dimitrios Mardoudas for their guidance and advising during my time at the University of Massachusetts, Amherst. If not for both of their efforts I would not have had the courage to pursue a degree in chemical engineering. Prof, Mountzaris developed my interests in research and gave me my first opportunity to work in a research laboratory. Prof. Mardoudas was my undergraduate chemical engineering academic advisor and played an important role in getting me to this point. I still remember the day when I schedule an impromptu meeting with him to change my major. I had just suffered my knee accident and I was unsure about my place in life and of my abilities to continue on in the major. He listened to me, dismissed my insecurities, and then reassured me that I had the ability to succeed in this field and help me continue on to get a degree in chemical

engineering. If not for his kind words of encouragement I would not be a proud chemical engineer today.

Over the course of my Ph.D. and had the incredible opportunity to collaborate with brilliant researchers including Prof. Monica olvera De la Cruz, Dr. Boran Ma, Dr. Spencer Brucks, Dr. Ramya Raghunathan, Prof. Makoto Asai, Prof. Kai Zhang, Dr. Ciprian Iacob, Dr. Nicholas Brady, and Jonathan Vardner. I want to thank Prof. De la Cruz and her student Dr. Boran Ma for their simulation expertise and immense knowledge in polymer electrolyte physics and self-assembly. Dr. Spencer Brucks was my first student mentor and taught me everything I know about solvent vapor annealing of polymer thin films. I want to give a special thank you to Prof. Ralph Coby for hosting me at Penn. State University so I could conduct dielectric spectroscopy with the help of Dr. Ciprian Iacob. Prof. Asai and Prof. Zhang provided an immense amount of technical and theoretical support that completely elevated my research on the self-assembly of charge – neutral diblock copolymer thin films. Dr. Ramya Raghunathan was great friend and provided an incredible amount of help in the synthesis of the materials used for this dissertation. Dr. Nicholas Brady and Jonathan Vardner are both members of the West research group and made an excellent team in developing electrochemical methods for the accurate characterization of polymer electrolyte transference numbers. Without their efforts, a substantial portion of this dissertation would not have been possible.

I would like to thank all the current and past graduate students in the Campos and Kumar research groups that I had the pleasure of interacting with including, Dr. Helen Tran, Dr. Samuel Sanders, Dr. Jonathan Low, Dr. Jessica Freyer, Dr. Spencer Brucks, Rachel Starr, Lauren Yablon, Dr. Andrew Pun, Emily Churchill, Kaia Parenti, Dr. Dan Zhao, Dr. Mayank Misra, Dr. Thi Vo, Dr. Connor Bilchak, Andrew Jimenez, Sophia Chan, Mayank Jhalaria, Clement Koh, Alejandro

Krauskopf, Sophia Chan, Husam Alkhodairi, Abdullah Altorbaq, Deboleena Dhara, and Robert Tannenbaum. You all made working at Columbia an absolute pleasure and I really appreciate all the help you've provided over the past five years.

Finally, I would like to thank my family. Mom, words cannot describe how grateful I am for all the times you came to visit me in New York despite your busy schedule, for all the late-night talks, and for you taking time off work to take care of me in NYC after my knee surgery. Together we have been through thick and thin and my only goal is to make you proud. Katie, Justin, and Alexander, thank you so very much for all your support and love over the years. You three were always in my thoughts. I want to thank my father for always being a lifeline to call when things seemed down. You supported me emotionally through my Ph.D. and provided a guiding light through some difficult times. I especially appreciated our weekly talks when we could talk about life, work, and the family. You always gave me the courage and extra push I need to move forward. Finally,, I want to thank my stepmother, Prof. Ting Xu, for your honesty and support. Having you in my life has been a blessing and I cannot say if I would be where I am today if you had not helped me put myself together. You always told me what I needed to hear and helps me mature an individual and develop as a researcher. You showed me that the instantaneous result is not everything and helped me see that the integration is what is important. Thank you all so very much, I love all of you.

Dedicated to my family

Chapter 1: Introduction.

1.2 Charge – neutral diblock copolymers (CN-BCP) self-assembly

1.1.1 Bulk CN-BCP microphase segregation

Polymer electrolytes offer a unique platform to tune ion transport for a wide variety of applications, such as transistors, energy storage and water/gas purification.[1–4] A key objective for these polymer electrolyte membrane-based technologies is to enhance ion mobility while maintaining mechanical integrity.[5–7] A widely used strategy to achieve these conflicting requirements is to spatially separate the chemical functionality responsible for mechanical properties and ionic conduction within a single system. This general paradigm allows for each phase to be engineered separately, while successfully building composites with tailored properties. A good example of such a construct is an A-B linear diblock copolymer (BCP), which offers predictable morphology behavior described by the Flory interaction parameter, χ, the total degree of polymerization, N, and the volume fraction of component A, ϕ_A. Considerable effort has been devoted to the creation of new classes of materials that leverage the predictable BCP morphology behavior, while incorporating chemical motifs to tune transport properties, such as ions[8–10], metals[11–14], and semiconductors[15].

Recently, charge-neutral diblock copolymers (CN-BCPs), BCPs with a polyelectrolyte block that facilitates ionic transport while the other, a neutral block that provides mechanical reinforcement, have been studied extensively for energy storage and water desalination applications. One method to prepare materials akin to CN-BCPs is to selectively dope salts or ionic liquids into conventional BCPs. This method has been shown to increase the effective χ between the two blocks yet minimally impact the overall shape of the BCP morphology diagram.[16] Another

explored route to forming CN-BCPs is to covalently append the ions to the backbone of one of the blocks. However, the majority of these systems are in the limit where electrostatic interactions play a secondary role in determining morphology, as we shall elaborate below. Thus, to date, experimental observations suggest microphase segregation in CN-BCPs can be understood as systems with minimal perturbation about the uncharged linear BCP analogs.

We investigate the types of CN-BCP morphologies that emerge in the limit where electrostatics dominate behavior (*i.e.* they are much stronger than traditional van der Waals interactions).[17] To quantify the importance of electrostatic interactions we define a cohesion parameter, $\Gamma = l_B/a$, where l_B is the Bjerrum length ($l_B = e^2/4\pi\varepsilon_0\varepsilon_r k_b T$), and a is the average ion pair spacing; this quantity is used to delineate the range of electrostatic interactions.[17] Here, ε_0 and ε_r are the permitivity of vacuum and of the medium of interest, respectively; e is the strength of point-charges, T is the temperature, and k_B is the Boltzmann constant. Theoretical models have suggested that increasing Coulombic cohesion to values where $\Gamma \gg 1$ can drastically alter CN-BCP phase behavior. While the highly asymmetric morphology diagrams predicted by this approach have not been experimentally observed, Γ provides insights into which types of materials might display these unique morphologies, *i.e.* CN-BCPs containing a charged block with a low dielectric constant, ε_r.

To experimentally investigate how Γ impacts self-assembly, we recently developed a new family of CN-BCPs with pendent trisaminocyclopropenium (TAC) ions, which are soft, highly delocalized, and stable. TAC salts crystallized from solution form counterintuitive structural motifs, where the TAC moieties form face-to-face stacks with no intervening counterions, implying an attractive interaction between objects of nominally the same charge. This phenomenon is driven by the atypical electron density distribution of the TAC ion.[18,19] In polymeric form, TAC-

containing polyelectrolytes have demonstrated unusual behavior[20–22] and, in a previous report, a symmetric block volume fraction TAC-containing CN-BCPs formed an anomalous, hexagonally packed, cylindrical morphology. This puzzling result appears to contradict the traditional BCP paradigm (where lamella may be expected) and indicate that these polymers may potentially exhibit complex morphological behavior.

To understand this unexpected, emergent morphological behavior in polymers with strong electrostatic interactions, we carried out a detailed study of the microphase segregation of polystyrene-*b*-poly(trisaminocyclopropenium chloride) (PS-*b*-PTAC) as a function of copolymer composition and chain length. Specifically, we focused on a TAC derivative bearing cyclohexyl groups (TACCy) for its facile processability in various organic solvents. We determined the temperature dependence of the static dielectric constant for the PTACCy block to be remarkably low (ranging between ε_r = 2.5 – 3) indicating that this family of CN-BCPs may fall in a range of Γ values that has, to date, not been experimentally probed. Indeed, we find a striking asymmetry in the morphology diagrams from this family of PS-*b*-PTACCy – drastically different than most other CN-BCPs studied. As a result, we often find that the minority component (the PTACCy block) forms the matrix over a broad range in composition. Using a suite of experimental (transmission electron microscopy, TEM, small angle x-ray scattering, SAXS) and theoretical arguments we assess the hypothesis that the asymmetry of the morphology diagram is related to the high Coulombic cohesion ($\Gamma \gg 1$) of these materials in Chapter 2 and Chapter 3 of this dissertation respectively. The observed percolating charge-containing phases, even when the ionic block content is as low as 40% by volume, offers the opportunity to explore new structure-property relationships driven by confined polyelectrolyte matrices. In addition to expanding the library of

accessible CN-BCP nanostructure the rational design of these materials can lead to morphologies with efficient ion conduction which is facilitated by a percolating ionic matrix.

1.1.2 Thin-film CN-BCP self-assembly

Controlling molecular organization of molecules at the nanoscale underpins the majority of commercial technologies available today. Self-assembly, a means of molecular organization, can occur thermodynamically via intrinsic chemical incompatibility between the molecular constituents or kinetically using physical directors (stress, electric and magnetic fields) or dynamic processes that trap the system in an ordered nonequilibrium state. Block copolymers (BCPs) are attractive class materials because the size of the copolymer (N) and the manner of monomer connectivity determine the sizes of the domains in the assembly, and, if the degree of incompatibility (χN) and the respective volume fractions of each component are known, then bulk morphology can be determined *a priori*. Recently, the BCP framework has undergone expansion with the inclusion of new functional motifs (*i.e.* hydrogen bonding, ions, metals, conjugation and peptides) and molecular architectures (*i.e.* rigid, dendrite, bottlebrush, branched backbones) in order to create multifunctional structured materials. While bulk materials have been the primary area of focus, thin films can be advantageous because reducing the film thickness can compensate for non-ideal transport properties.

Incorporating electrolytes into polymer thin films (either physically or chemically) have been used widely to create anti-microbial coatings, ion-conducting thin films, and flexible photovoltaics. Although, structuring charge-neutral block copolymers (CN-BCPs) in thin-films is an area research that has been relatively untouched. To enhance the processability of these materials, researchers have focused on ion doped BCPs, post-assembly ionized BCPs, or CN-BCPs with a reduced ion density (ionomer block[s]). As the thickness of polymeric material reduces the

influence of interfacial interactions become increasing more relevant. Preferential segmental interactions with an interface can lead to increased domain registry along with the promotion of a single domain orientation. However, the influence of ionic interactions on CNBP microphase segregation in thin films remains an open question.

In Chapter 5 of this thesis we discuss the implications of film thickness on the self-assembly of solvent vapor annealed PS-b-PTACCy thin-films. Using a combination of atomic force microscopy and grazing incidence small angle x-ray scattering we present a detail thin film morphology diagram that covers the same compositional phase space as the bulk morphology diagram discussed in Chapter 2. Similar to the bulk morphology diagram we observe an extended C_N morphology window yet a lack of both the LAM and S_N morphologies. We postulate that these stark differences arise from the contribution of interfacial energies on the PS-*b*-PTACCy self-assembly. Additionally, we probe the thickness dependence of PS-*b*-PTACCy CN-BCPs and find the cylinder domain oscillates between perpendicular and parallel orientation near the order – disorder transition ($\phi_{CN-BCP} = 0.4$). Control over the CN-BCP morphology opens the door for the investigation of ion transport through structure thin-films and can lead to the discovery of new structure – property relationships.

1.1.3 Solvation effects on CN-BCP self-assembly

Decoding charge – neutral diblock copolymer (CN-BCP) microphase segregation has been a central theme for this thesis, and one outstanding facet yet to be explored is the influence of solvent on the PS-b-PTACCy self-assembly which is discussed in Chapter 6 of this thesis. Wel utilize solvent vapor annealing to kinetically trap the PS-b-PTACCy CN-BCP thin films in morphologies that reflect the influence of solvent interactions. *In-situ* grazing incidence small angle x-ray scattering techniques was employed to track the PS-*b*-PTACCy thin-film morphology

through the solvent vapor annealing process. We identified two quantitatively different processing pathways facilitated by nonselective and selective solvation of the PS-*b*-PTACCy thin film. Solvent vapor annealing with nonselective solvents, solvents that solvate both the PS and PTACCy block, infiltrated the PS-b-PTACCy film and facilitate an order – disorder transition with increasing solvent volume fraction. Selective solvents, *i.e.* methanol, produce a ordered swollen state morphology at large solvent volume fraction. Across all solvent systems using to vapor anneal we observed a singular PS-*b*-PTACCy CN-BCP thin-film morphology – C_N. However, subtle differences in the PS-*b*-PTACCy periodicity and average crystalline grain were observed that are thought to reflect differences ionic interaction strength during the vapor annealing. Modification to the ionic interaction strength was achieve by changing the dielectric constant (ε_r) of the annealing solvent. We found the PS-b-PTACCy periodicity increased with decreasing ε_r where a larger domain spacing arises from stronger ionic interactions. Additionally, increasing the solvent ε_r increases the average crystalline grainsize indicating that reducing the ionic interaction strength allows the PS-b-PTACCy CN-BCP to approach an equilibrium morphology. Overall, exploring the effect of solvation on the PS-b-PTACCy self-assembly provides more evidence to deciphering the origins of the asymmetric thin film and bulk PS-*b*-PTACCy morphology diagrams.

1.2 Ion transport through polymer electrolyte separators

Polymer electrolytes, flexible chains comprised of catenated ions, combine the mechanical properties of polymers with high ionic and low electronic conductivity of liquid electrolytes[4–7]. In contrast with most liquid electrolytes, polymer electrolytes offer more convenient processing strategies since they do not require hazardous organic solvents to enable ion transport[23]. As a result, a significant effort has been devoted to studying the intricate structure-property relationships governing ion transport through polymer electrolyte melts. In this situation, the ionic mobility is

inversely correlated to the material mechanical modulus due to the intrinsic coupling between ionic conductivity and the polymer electrolyte's segmental relaxation[24–30]. However, other technologies such as electrodialysis[31,32], redox flow batteries[33,34], and water desalination[35,36] require polymer electrolyte separators swollen with water, ionic liquids, or organic solvents. In these applications, a quantitative description of the separator counterion transference number (t_c^m) ($i.e$ ionic selectivity), ionic conductivity (κ), concentration of ions in the separator, and ion diffusion coefficients is imperative for a complete description of ion transport. The t_c^m provides the fraction of the current across the polymer separator carried by counterions in the absence of concentration gradients. For all the mentioned applications, $t_c^m \to 1$, corresponding to perfect counterion selectivity, is desired. Neat polymer electrolytes achieve $t_c^m = 1$ due to ion connectivity with the polymer backbone[5], however, in solvated polymer electrolytes t_c^m has a strong dependence on separator hydration state.[37] Therefore, the relationship between κ and t_c^m and their dependence on separator hydration state and must be determined for an accurate assessment of separator performance.

Studies conducted on swollen polymer electrolytes show an inverse relationship between ionic conductivity (κ) and the separator ionic permselectivity (Ψ^m)[37]. The Ψ^m is defined as the difference between t_c^m and in an aqueous electrolyte (t_c^{aqu}) normalized by the transference number of a coion in an aqueous electrolyte $(1 - t_c^{aqu})$.

$$\Psi^m = \frac{t_c^m - t_c^{aqu}}{1 - t_c^{aqu}} \tag{1.2.1}$$

For an electrolyte solution t_c^{aqu} can be determined using dilute solution theory with knowledge of the aqueous salt diffusion coefficients and solution concentrations.

$$t_c^{aqu} = \frac{z_c^2 D_c^{aqu} c_c}{\sum_i z_i^2 D_i^{aqu} c_i} \quad (1.2.2)$$

Where z_c, D_c^{aqu}, and c_c correspond to the counterion charge, aqueous diffusion coefficient and solution concentration, and the denominator is a summation over all ions in solution. For electrolyte solutions, Eq 1.2.2 can be simplified since the electrolyte concentrations are usually known, however, for swollen polymer electrolytes, the concentrations of ions in the separator are often difficult parameters to determine. A permselectivity $\Psi^m = 1$ indicates the separator is perfectly selective for the separator counterion. The minimum is likely to be $\Psi^m = 0$, meaning the separator transference number is $t_c^m = t_c^{aqu}$ and a complete loss of ion fidelity. Similarly, polymer membrane-based technologies for gas separation[38–40] have reported a similar trade-off between permeability and selectivity. The membrane separation quality has been linked to a size sieving mechanism related to the molecular rigidity of the polymeric material.[41–43] However, for swollen polymer electrolyte separators the underlying cause for the $\Psi^m - \kappa$ tradeoff is still unknown.

Separator water volume fraction (ϕ_{H_2O})[2,37,44] and ion exchange capacity (IEC) have been proposed as potential candidates for causing the $\Psi^m - \kappa$ tradeoff. The IEC, defined as the equivalent units of ions per gram of dry polymer, has been traditionally used to describe trends in transport data. However, accounting for ϕ_{H_2O} in the separator charge density, *i.e.* the swollen-state charge density, has proven to correlate better with trends in Ψ^m[37]. Increasing the swollen-state charge density in sulfonated poly(sulfone) cation exchange, poly(phenylene oxide)[37] cation exchange, and methacrylate-based anion exchange membranes[45] produced separators with higher Ψ^m. On the other hand, increasing ϕ_{H_2O} dilutes the fixed charge density but increases the measured κ presumably through increasing the counterion diffusion coefficient. Thus, the $\Psi^m - \kappa$ tradeoff may arise through an interplay between improving ion mobility while reducing the fixed charge

density. Unfortunately, the relationship between ϕ_{H_2O} and charge density for a given polymer electrolyte is difficult to predict, making materials development challenging. To add a layer of complexity, the solution salt concentration can influence the separator ϕ_{H_2O} through osmotic swelling/deswelling[46] may lead to inconsistent separator performance depending on the separation process requirements – dilute or concentrated salt streams.

Recent theoretical treatments of ion transport in polymer electrolytes highlight the material properties that might effect the $\Psi^m - \kappa$ tradeoff (i.e. ϕ_{H_2O}, separator charge density, separator thickness, and electrostatic interactions)[47–49], but offer minimal insight into what experimental handles can be turned to mitigate these properties. The literature contains a library of chemically different separators, yet quantitative structure – property relationships connecting chemical architecture to separator performance are missing. Additionally, manipulating the morphology of ionic materials has proven to be an effective method to tune the ionic conductivity[27,50–52] but the influence of structure on Ψ^m is still an open area of research. Guler et al. studied crosslinked polyepichlorohydrin anion exchange membranes blended with polyacrylonitrile, an inert and mechanically reinforcing component, as acid blocking separators in electrodialysis.[53] Increasing the amount polyacrylonitrile incorporated into the anion exchange membrane enhanced the Ψ^m with a minimal impact to the area resistance and suggests that inert heterogeneities within ionic separators may play a role in ion transport. Additionally, simulations on dielectric heterogeneous separators arising from phase separator from immiscible components find surface polarization originating from a dielectric contrast between two immiscible phases can influence the ion distribution and mobility near the interface.[54–57] On the other hand, Geise et al. measured no effect of morphology on salt sorption in pentablock copolymer cation exchange separators.[58] Thus, the complex relationship between separator structure and ion transport properties in swollen polymer

electrolytes has yet to be fully determined. In fact, setting morphology aside, the vast polymer electrolyte materials space has yet to be thoroughly explored, as the impact of parameters such as molecular weight, chain architecture, and cross-linking density on the $\Psi^m - \kappa$ tradeoff are unknown. Therefore, in order to rationally design more advanced swollen polymer electrolytes separators, it is advantageous to understand which material considerations have the highest impact on the $\Psi^m - \kappa$ tradeoff.

In Chapter 4 of this thesis, we present a summary of the literature and an extensive description of the $\Psi^m - \kappa$ trade-off. We chose to study randomly sulfonated polystyrene homopolymers (PS-*r*-sPS) at a constant molecular weight to compliment the trends observed in state-of-the-art separators such as functionalized main chain aromatic containing polymers [*i.e.* (poly(sulfone), poly(phenylene oxide) or poly(ether etherketone)] or chemically cross-linked polymer electrolyte networks. The influence of separator morphology, molecular weight, hydration state, and counterion identity on ion conductivity in sulfonated polystyrene (PS-*r*-sPS) separators have been studied extensively[26,59–61], and in this thesis, PS-*r*-sPS was chosen a model polymer electrolyte to probe how these parameters influence Ψ^m. We prepared a variety of different PS-*r*-sPS charge densities from commercially available polystyrene and characterized the mechanical properties, ϕ_{H_2O}, Ψ^m, and κ. Additionally, we examine the role of ϕ_{H_2O} on the counterion diffusion coefficient and find quantitative agreement with tortuosity models in highly swollen sPS separators ($\phi_{H_2O} = 0.83$). For low to moderately swollen PS-*r*-sPS separators, the discrepancies between theoretical predictions for the counterion diffusion coefficient and the values experimentally determined can be rationalized through electrostatic considerations. Finally, we rationalize the decrease in Ψ^m to be intimately related to the dilution of fixed charge density and the breakdown of Donnan exclusion. The development of quantitative structure – property relationships that

enable a facile navigation of the $\Psi^m - \kappa$ trade-off will provide the foundation for the rational design of inexpensive, robust single ion conducting polymer electrolyte separators.

Chapter 2: Role of ionic interactions in charge – neutral diblock copolymer self-assembly.

The self-assembly of diblock copolymers (BCP) comprising flexible polymer chains, driven by a balance of enthalpic and entropic forces, is well understood. If one of the blocks is a polyelectrolyte, forming a charge-neutral diblock copolymer (CN-BCP), Coulombic interactions can play a significant role in the self-assembly. Here, electron microscopy and small angle x-ray scattering, in combination with free-energy arguments and a scaling model inspired by surfactant self-assembly are used to investigate the microphase segregation of CN-BCPs having pendent trisaminocyclopropenium (TAC) ions. We find that the TAC polymer electrolytes have an unexpectedly low dielectric constant (~2.5) and that CN-BCPs containing a TAC polymer electrolyte block exhibit highly asymmetric morphology diagrams. These CN-BCP morphology diagrams have an unexpectedly large range of CN-BCP compositions where cylinders form, with the TAC block forming the continuous matrix, and in contrast to conventional BCPs these cylindrical phases form even when the charged block is a minority constituent. These unusual morphologies observed in CN-BCPs with strong electrostatic interactions may thus provide a foundation for the exploration of new modes of ion transport in block copolymer self-assemblies.

2.2 Material synthesis, experimental methods, and instrumentation

In this section we will briefly discuss the synthetic strategy for preparing PS-*b*-PTACCy CN-BCPs and the relevant experimental methods/instrumentation for their characterization. All materials were purchased from Sigma-Aldrich and were used without further purification except as noted below. Methylene chloride (CH_2Cl_2) and N,N-dimethylformamide (DMF) were dried using a J.C. Meyer solvent purification system. Deuterated solvents used for NMR spectroscopy were purchased from Cambridge Isotope Laboratories, Inc. Eluents for column chromatography were HPLC grade and purchased from Fisher Scientific. Organic solutions were concentrated by use of a Buchi rotary evaporator. All polymerizations were carried out with temperature control via an oil bath under an argon atmosphere in Schlenk flasks. ^{1}H NMR spectra were recorded in $CDCl_3$ (except where noted in experimental section) on a Bruker AMX-300, AMX-400, or AMX-500 spectrometer.

2.2.1 The synthetic procedure for preparing PS-b-PTACCy CN-BCPs

The first step in the PS-b-PTACCy CN-BCP synthesis is preparing the polystyrene macroinitiator using atom transfer radical polymerization (ATRP) technique. A complete description of the polymer synthesis can be found elsewhere[21] and here we provide a general procedure for the polymerization of styrene. Copper (I) bromide (13.8 mg, 9.6×10^{-2} mmol, 0.5 equiv) and tris(2-pyridylmethyl)amine (39 mg, 1.3×10^{-1} mmol, 0.7 equiv) were added to a dry Schlenk flask and the material was deoxygenated via five vacuum-argon cycles. Degassed styrene (10g, 96.1 mmol, 500 equiv) was added to the flask and allowed to stir for 10 minutes under argon until the solution turned light green, indicating that the Cu complex formed. The Schlenk flask was closed under argon and degassed ethyl α-bromoisobutyrate (37.7 mg, 1.9×10^{-1} mmol, 1 equiv) was injected. The reaction mixture was heated to 90 °C and allowed to react overnight.

Aliquots were taken at different times and examined by ^{1}H NMR and gel permeation chromatography (GPC) to determine conversion and dispersity (Đ). The polymer was dissolved in tetrahydrofuran (THF), filtered through an alumina column, precipitated twice into a stirred solution of cold methanol, and vacuum dried overnight. The molecular weights and Đ of the final material were determined using GPC in THF calibrated with polystyrene standards.

Before moving on to the chain extension reaction, a necessary step for making the PTACCy block, we discuss the preparation of the desired polymerizable monomer, tert-butyl methyl(4-vinylbenzyl)carbamate, using an established procedure[21]. N-methyl-4-vinylbenzylamine (10.07 g, 68.4 mmol, 1 equiv) and THF (300mL) were added to a 1 L round bottom flask (RBF) and the flask was sealed with a septum secured with copper wire under argon with a gas outlet. Triethylamine (10.4 mL, 74.8 mmol, 1.1 equiv) was added to the RBF, the system was cooled to 0 ºC, and ditertbutyl dicarbonate (16.42 g, 74.8 mmol, 1.1 equiv) was slowly injected. The RBF was warmed to room temperature and allowed to stir overnight. The solution was concentrated under vacuum, and the translucent, crude product was dissolved in 300 mL of CH_2Cl_2 and transferred to a 1 L separatory funnel. The solution was washed with 1 M HCl (3 x 100 mL) followed by a single brine wash. The solution was then dried with magnesium sulfate, filtered, and concentrated under vacuum. The crude material was finally purified by silica gel chromatography (100% hexanes then 95% CH_2Cl_2/5% hexanes) to yield the desired product a translucent, colorless liquid. The ^{1}H NMR chemical shifts and integrations have been reported elsewere.[21]

Following the preparation of the tert-butyl methyl(4-vinylbenzyl)carbamate (NBoc) we conducted an ATRP chain extension reaction to prepare a PS-*b*-P(NBoc) diblock copolymer. The chain extension polymerizations were carried out as follows. Copper (I) bromide (1.0 mg, 7.54×10^{-3} mmol, 0.5 equiv) and tris(2-pyridylmethyl)amine (3.0 mg, 7.54×10^{-3} mmol. 0.7

equiv) were added to a dry Schlenk flask and the material was deoxygenated via five vacuum-argon cycles. Degassed tert-butyl methyl(4-vinylbenzyl) carbamate (1g, 4.45 mmol, 300 equiv) was added to the flask and allowed to stir for 10 minutes under argon until the solution turned light green, indicating the Cu complex formed. The mixture was subjected to three freeze-pump-thaw cycles to ensure all oxygen was removed from the reaction vial. The Schlenk flask was closed under argon and degassed polystyrene macroinitiator anisole solution (174 mg, 1.488×10^{-2} mmol, 1 equiv) was injected, the reaction mixture was heated to 90 °C and allowed to react overnight. Aliquots were taken at different times and examined by ^{1}H NMR to determine conversion. The polymer was dissolved in tetrahydrofuran (THF), filtered through an alumina column, precipitated three times into a stirred cold methanol/water solution, and vacuum dried overnight. The molecular weight and Đ of the final material were determined using GPC in THF using polystyrene standards. The ^{1}H NMR chemical shifts and integrations have been reported elsewere.[21]

Once the PS-b-P(NBoc) is purified, it is then necessary to remove the tert-butyl ester protecting group and expose the polystyrene-*b*-poly(4-methylamino)styrene (PS-*b*-PMAS). The PMAS motif can be readily functionalized with the bisaminocyclopropeniumdicyclohexyl chloride salt. The deprotection step proceeds as follows. The PS-b-P(NBoc) (200 mg, 0.44 mmol amine-containing monomer, 1 eq amine monomer) was dissolved in a 50/50 dichloromethane:methanol solution (15 mL) in a round bottom flask under argon. The flask was cooled to 0˚C and trimethylsilyl chloride (337.5 mg, 3.125 mmol, 7 eq) was added. The reaction was allowed to stir at room temperature overnight and concentrated under vacuum to yield a white powder. The powder was then re-dissolved in DMSO and 1 M NaOH was added dropwise, with stirring, until the polymer precipitated from solution. The resulting slurry was centrifuged, and the

supernatant decanted. The polymer was washed two more times with DI water, and collected by centrifugation. The resulting polymer was dried under vacuum, yielding a fluffy, white powder. The ^{1}H NMR chemical shifts and integrations have been reported elsewhere.[21]

The final set of PS-*b*-PTACCy synthesis is the preparation of Polystyrene-*b*-Poly(trisaminocyclopropeniumdicyclohexyl chloride)styrene (PS-b-PTACCy) via the post polymerization functionalization of PS-b-PMAS**.** This procedure was performed in atmospheric conditions. PS-*b*-PMAS (100 mg, 0.27 mmol amine unit, 1 equiv amine unit) was dissolved in chloroform (4 mL) in a scintillation vial. *N,N*-diisopropylethylamine (105.3 mg, 0.53 mmol, 3 equiv) was added to the vial, followed by a solution of TACCy (137 mg, 0.3 mmol. 1.1 equiv) in 4 mL of Chloroform. The reaction mixture was heated to 65 °C and allowed to react overnight. The resulting solution was concentrated *in vacuo*, dissolved in methanol, transferred into a 3.5 kDa MWCO Spectrum Labs dialysis bag, and allowed to dialyze in a methanol bath for three days where the bath was replaced with fresh methanol twice per day. The resulting colloidal solution was concentrated under vacuum to yield a light brown powder. The ^{1}H NMR chemical shifts and integrations have been reported previously.[21,22]

2.2.2 The characterization of PS-*b*-PTACCy CN-BCPs physical properties.

To accurately determine the volume fraction of the PTACCy block for each prepared PS-b-PTACCy (ϕ_{CN-BCP}) we first need to acquire key physical information about the material – i.e. block chain lengths and bulk polymer densities. Fortunately, the molecular weight (M_n) of the PS macroinitiators used can be measured routinely using GPC and the bulk PS density is known ($\rho_{PS} = 1.04\ g/cm^3$). However, for the PTACCy block, GPC only provides a means to determine the CN-BCP dispersity index (Đ) and is not calibrated to measure the PS-b-PTACCy CN-BCP M_n. Fortunately, once the PS molecular weight is determined, the PTACCy block M_n can be

determined using ^{1}H NMR. Additionally, the PTACCy bulk density was also unknown and measured using helium pycnometry. Figure 2.2.1.1 are density measurements made using helium gas pycnometry. The experiments were conducted at the Penn. State University Materials Characterization Laboratory using the Micrometrics Accupcy II 1340. For this measurement 283 mgs of PTACCy homopolymer was crushed, loaded into the pycnometer crucible, and subjected to characterization. The open black circles are 10 different measurements made on the material, and average PTAC density was measured to be 1.0766 g/cm^3.

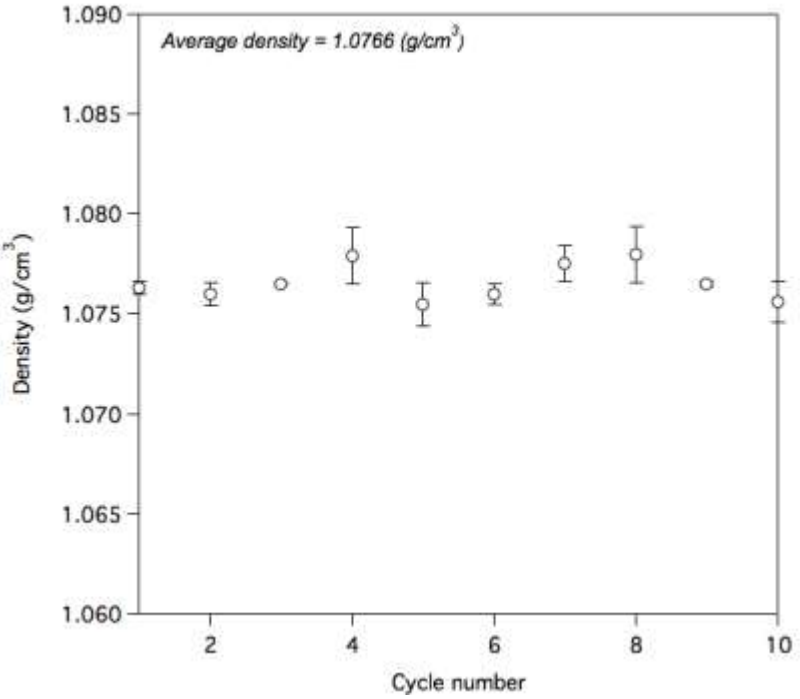

Figure 2.2.2.1. Measurement of the PTACCy bulk density. The PTACCy bulk density measured ten separate times using helium pycnometry. The average bulk density is provided as an insert, $1.0766\ \mathrm{g/cm^3}$.

As mentioned previously, the PS macroinitiators were characterized using GPC to quantify their M_n and dispersity (Đ) on a Waters Alliance 2695 separation module equipped with a PL-aqua gel-OH 8-micron Mixed-M column (300 x 7.5 mm), a Waters 2998 Photodiode Array Detector, and a Waters 2414 Refractrometer Detector. Tetrahydrofuran stabilized with

dibutylhyrdroxytoluene (5 mg/mL) was used as the eluent at a flow rate of 1mL/min. Prior to every run, the instrument was calibrated to polystyrene standards to ensure an accurate determination of the macroinitiator M_n. An accurate measurement of the PS M_n is crucial part of this study as a lot of import physical properties depend on the accurate measurement of this quantity. For example, since the we do not have standards for PS-b-PTACCy CN-BCPs we must use an alternative method for measuring the PTACCy M_n – ^{1}H NMR. We compared the area under isolated chemical shifts that correspond to protons only on TACCy monomers to the integrated area of the aromatic protons yielding the TACCy:styrene monomeric ratio, and if the PS M_n (*i.e.* the average number of PS monomer) is known, we can obtain the PTACCy block M_n. Additionally, to calculate ϕ_{CN-BCP} the PS block M_n, the PTACCy block M_n, and the bulk densities must be known.

After the PS-*b*-PTACCy physical parameters were known we set out to measure the structural characteristics of their assemblies using transmission electron microscopy (TEM) and small angle x-ray scattering (SAXS). The TEM was performed on a Philips CM12 TEM at an accelerating voltage of 120 kV at NYU Langone's Microscopy Laboratory. The samples were prepared by curing them in EMbed 812 Resin (Electron Microscopy Sciences) at 80 °C for 12 hours. Sectioning of the samples was performed on a Leica Ultracut UCT microtome with thicknesses of 60 nm then placed on a formvar coated copper grid. Droplets of 1% OsO_4 were left on the grids for one hour, then thoroughly washed with DI water, in order to stain the samples and increase the contrast between the two phases. Images were acquired in bright field mode using an objective aperture with a Gatan 4k x 2.7k digital camera at a variety of magnifications across the samples. The SAXS was performed at the Advance Light Source Lawrence Berkeley National laboratory on the 7.3.3 beam line with a constant X-ray energy of 10 keV. The sample to detector distance was calibrated using a silver behenate standard. The scattering profiles were recorded

using a Pilatus 1M 2-D area detector. Additionally, samples were also run at the National Synchrotron Light Source II, Brookhaven National Laboratory on the 11-BM beamline with a constant X-ray energy of 10 keV.

Table 2.2.1.1 A summary of PS-b-PTACCy CN-BCPs.

Polymer Name	PS M_n (kg/mol)	Charge Fraction ($\phi_{CN\text{-}BCP}$)	Charge Fraction ($\phi_{CN\text{-}BCP}$)	Degree of Polymerization (N)	Dispersity (Đ)
PS_{175}-*b*-$PTAC_{25}$	18	0.44	0.43	200	1.08
PS_{175}-*b*-$PTAC_{60}$	18	0.66	0.64	235	1.14
PS_{175}-*b*-$PTAC_{90}$	18	0.74	0.75	265	1.2
PS_{130}-*b*-$PTAC_{10}$	14	0.31	0.40	140	1.07
PS_{130}-*b*-$PTAC_{20}$	14	0.38	0.39	150	1.07
PS_{130}-*b*-$PTAC_{40}$	14	0.61	0.61	170	1.07
PS_{130}-*b*-$PTAC_{60}$	14	0.72	0.75	190	1.18
PS_{130}-*b*-$PTAC_{90}$	14	0.77	0.81	220	1.08
PS_{90}-*b*-$PTAC_{25}$	9.5	0.60	0.62	115	1.04
PS_{90}-*b*-$PTAC_{60}$	9.5	0.78	--	150	1.07
PS_{90}-*b*-$PTAC_{75}$	9.5	0.82	--	165	1.09
PS_{90}-*b*-$PTAC_{90}$	9.5	0.85	--	180	1.09
PS_{90}-*b*-$PTAC_{130}$	9.5	0.89	0.88	220	1.11
PS_{60}-*b*-$PTAC_{60}$	6.5	0.85	--	120	1.08

Table 2.2.1.1 provides a comprehensive list of all prepared PS-*b*-PTACCy CN-BCPs examined in this Chapter. Each table entry is listed as PS_x-*b*-$PTACCy_y$ where the subscripts x and y indicate the average number of monomeric repeat units in the PS and PTACCy block respectively. The ϕ_{CN-BCP} was obtained using ^{1}H NMR, the bulk density of PS (ρ_{PS}= 1.04 g/cm^3), the bulk density of PTACCy (ρ_{PTACCy}= 1.07 g/cm^3), and assuming no volume change upon

mixing. A second measure of the ϕ_{CN-BCP} fraction was calculated using a combination of TEM image analysis and small angle x-ray scattering to obtain the size of the PS domain and CN-BCP domain spacing respectively. Any spaces that have a (--) correspond to materials that we were unable to be imaged via TEM. The total degree of polymerization (N) was calculated using a combination of gel permeation chromatography calibrated with polystyrene standards and ^{1}H NMR. Specifically, GPC was used to obtain the number of styrene monomers in the PS macroinitiator and ^{1}H NMR to determine the number of PTACCy monomers relative to the PS monomers in the macroinitiator. The dispersity was measured using gel permeation chromatography calibrated to polystyrene standards using THF as the mobile phase.

2.3 PTACCy homopolymer thermal and dielectric properties

2.3.1 PTACCy thermal properties

Before we can attempt to thermally anneal the PS-*b*-PTACCy CN-BCPs we first established two important thermal benchmarks, (1) PTACCy degradation temperature (T_d) and (2) PTACCy glass transition temperature (T_g). The PS T_d and T_g are known and are $> 300^{\circ}C$ and $\sim 105^{\circ}C$ respectively. To measure the PTACCy T_d we preformed thermal gravimetric analysis (TGA) a technique designed to measure a sample mass loss as a function of increasing temperature. The PTACCy mass fraction (%) is calculated using Eq (2.3.1.1) and plotted in Figure 2.3.2.1 as a function of temperature.

$$mass\ fraction = \left[\frac{m_{T=i}^{PTACCy} - m_{T=T}^{PTACCy}}{m_{T=i}^{PTACCy}}\right] \times 100 \qquad (2.3.1.1)$$

The PTACCy mass at temperature T, $m_{T=T}^{PTACCy}$, is subtracted from the initial PTACCy mass, $m_{T=i}^{PTACCy}$, then normalized by $m_{T=i}^{PTACCy}$. Three separate experiments were conducted to probe the PTACCy thermal stability under inert conditions, in the presence of oxygen, and a thermal

processing mimic where the PTACCy sample is held isothermally at an elevated temperature for a long period of time. Figure 2.3.2.1 presents the results of these experiments using the light blue, blue, black traces respectively. The light blue trace, the inert condition experiment, we observe two separate degradation events occurring at $\sim 250^{\circ}C$ and $\sim 410^{\circ}C$ corresponding to the thermal decomposition of the TACCy pendant and the polymer backbone respectively. As the temperature exceeds $700^{\circ}C$ the PTACCy mass fraction does not go to zero indicating a complete decomposition in the inert N_2 environment. The blue trace is an identical experiment as the light blue trance except the PTACCy sample is exposed to an oxygen containing environment. Again, we observe the same two degradation events, however, there is no residual carbon coking at high temperatures. To this point, as the temperature exceeds $\sim 500^{\circ}C$ we find a complete loss of all PTACCy mass. For both experiments, the experimental temperature was increased with a constant ramp rate of $10^{\circ}C/min$ starting at $40^{\circ}C$ and finishing at $700^{\circ}C$.

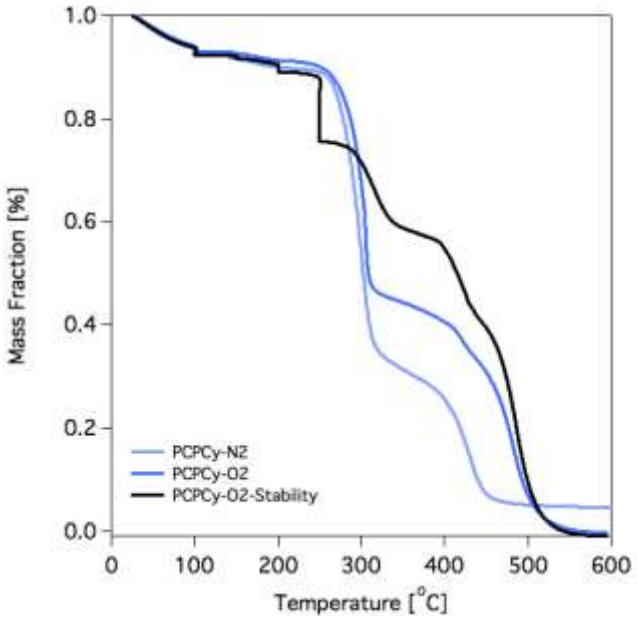

Figure 2.3.1.1. A summary of PTACCy homopolymer TGA results. Thermal degradation profiles for PTACCy under a variety of different conditions. The light blue, deep blue, and black traces were conducted using a pure N_2, a mixture of N_2/O_2, and a mixture of N_2/O_2.

The final thermal stability experiment was done in the presence of oxygen and conducted to mimic a thermal processing of PTACCy (Figure 2.3.2.1 black trace). In this experiment, the temperature was set to a constant ramp rate of $10^{\circ}C/min$ ramp of starting at $40^{\circ}C$ and finishing at $700^{\circ}C$ with the addition of 30 minute isothermal idling at $100^{\circ}C, 150^{\circ}C, 200^{\circ}C$, and $250^{\circ}C$. Hold the sample idly at a fixed temperature and monitoring the PTACCy mass fraction is used to mimic sample processing procedures and determine if there is any significant sample degradation after a prolonged exposure. From the blue traces, we deduced the TACCy $T_d \sim 240^{\circ}C$, the temperature corresponding to ~5% mass loss. The mass loss at low temperatures were attributed to the loss of residual solvents and water trapped in the PTACCy homopolymer. However, the 30-minute isothermal idling steps at $200^{\circ}C$ and $250^{\circ}C$ indicate that the PTACCy will degrade at temperature lowers than T_d over a short period of time. As a result, the maximum temperature for thermal processing is limited to between $150 - 180^{\circ}$ and depending on the T_g may limit the accessibility of thermal annealing for the PS-*b*-PTACCy CN-BCPs.

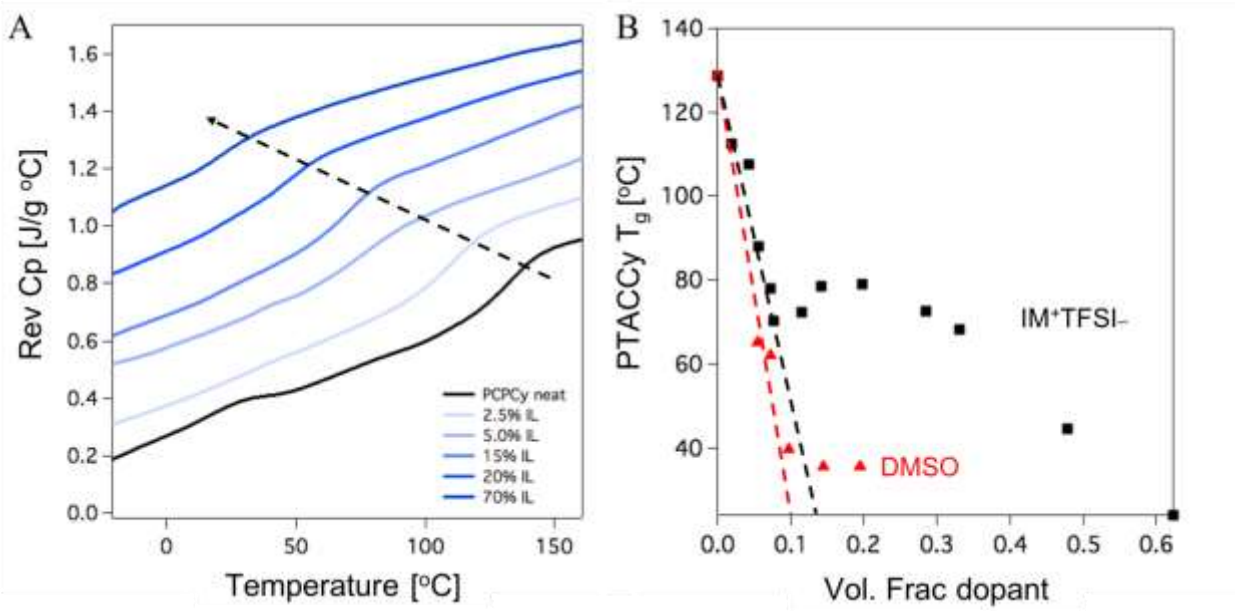

Figure 2.3.1.2. A summary of neat and doped PTACCy homopolymer DSC results. (A) the reversive heat capacity (Rev Cp) vs. temperatures taken from of the second cool for PTACCy homopolymers doped with various amounts of ionic liquids. (B) a master curve plotting the apparent PTACCy T_g as a function of dopant volume fraction.

To probe the PTACCy T_g we utilized differential scanning calorimetry (DSC). By modulating the temperature (T_{mod} $= 1.27^{\circ}C/min$) we extracted out the reversible part of the measured heat capacity (Rev Cp) and it is plotted in Figure 2.3.1.2A as function of temperature. From these traces we located the polymer T_g, indicated by a step in the Rev Cp, and the T_g is determined by the midpoint of the transition. Figure 2.3.2.2A plots the Rev Cp vs. temperature for a neat PTACCy homopolymer (black trace) and a variety of PTACCy homopolymers doped with ionic liquids (1-methylimidazolium bis(trifluoromethanesulfonyl)imide) at increasing dopant volume fraction. As the dopant volume fraction increases the apparent PTACCy T_g decreases indicating the polymer segmental relaxations increase from the solvation. The glass transition for all doped samples were computed and plotted in Figure 2.3.2.2B. Note that the black squares and red triangles correspond to PTACCy homopolymers doped with the ionic liquid and

dimethylsulfoxide (DMSO) dopants respectively. Both dopants display qualitatively similar effects on the apparent PTACCy T_g. In both cases, as the dopant volume fraction approaches zero both mixtures approach the same glass transition temperature indicated by the provided straight dotted lines. Therefore, the definitive PTACCy T_g is $130^{\circ}C$ and in very close proximity to our maximum thermal processing temperature. The importance of this analysis is hidden in the first $50^{\circ}C$ of Figure 2.3.2.1 – polyelectrolytes readily uptake water and solvents. As shown in Figure 2.3.2.2B, the PTACCy T_g is extremely sensitive to moisture and residual amounts of solvent, thus it is imperative to remove the solvent influence on $T_g$and obtain a zero point extrapolation to get the true PTACCy T_g. This method provides an accurate determination the PTACCy T_g but suggests the neat PTACCy T_g is near the T_d making PS-*b*-PTACCy CN-BCPs thermal annealing an impossible.

2.3.2 PTACCy dielectric properties

We made an extensive effort to characterize the dielectric properties of the PTACCy block. The key insight into this fundamental study was the direct comparison between CN-BCP morphology and the strength of ionic interactions across CN-BCPs with various polyelectrolyte and neutral block chemistries to draw a relationship. To do this, we first conducted dielectric spectroscopy to measure the PTACCy ionic conductivity (σ_0) frequency (ω) dependence and the static dielectric constant (ε_r) at various temperatures. The PTACCy homopolymer was dissolved in tetrahydrofuran (300 mg/mL), cast onto a Teflon dish, and allowed to evaporate overnight into a film. The film was lifted, placed onto a Pt electrode (D = 6 mm) and then vacuum annealed at $180^{\circ}C$. Multiple $50\,\mu m$ thick silicon oxide fiber spacers were placed on top of the vacuum annealed PTACCy film followed by a second Pt electrode. The stack was hand pressed under vacuum using a custom-built vacuum chamber at 180 °C to form a uniform $50\,\mu m$ sample

thickness. The dielectric measurements of PTACCy were performed over a wide frequency (10^{-1}–10^{7} Hz) and temperature (303–493 K) range under a dry nitrogen atmosphere using a Novocontrol dielectric analyzer. Dielectric experiments were conducted with low applied voltage (0.1V) in order to avoid any electrochemistry at electrode interfaces.

The electrode polarization (EP) fitting procedure pioneered by Klein et al[62] we employed. To perform this analysis, we apply the following transformation $tan(\delta) = \varepsilon^{"}/\varepsilon'$ where $\varepsilon^{"}$and ε' are the imaginary and real components of the dielectric permittivity respectively. Fitting the $tan(\delta)$ frequency dependence is advantageous because the conductivity is suppressed, the peak $tan(\delta)$ maximum is at higher frequencies, and the static dielectric constant is removed from the fitting procedure. Expressions for $tan(\delta)$, $\varepsilon^{"}$and ε' to describe EP are given:

$$\varepsilon'_{EP} = \varepsilon_r + \frac{\Delta\varepsilon_{EP}}{1+\omega^2\tau_{EP}^2} \tag{2.3.3.1}$$

$$\varepsilon^{"}_{EP} = \frac{\Delta\varepsilon_{EP}\omega\tau_{EP}}{1+\omega^2\tau_{EP}^2} \tag{2.3.3.2}$$

$$tan(\delta) = \varepsilon^{"}/\varepsilon' = \frac{\Delta\varepsilon_{EP}\omega\tau_{EP}+\sigma_0/\varepsilon_{EP}\omega(1+\omega^2\tau_{EP}^2)}{\Delta\varepsilon_{EP}+\varepsilon_r(1+\omega^2\tau_{EP}^2)} \tag{2.3.3.3}$$

Where σ_0, τ_{EP}, ε_r, ω, and $\Delta\varepsilon_{EP}$ are the PTACCy conductivity, characteristic relaxation time for electrode polarization, static dielectric constant, frequency, and the low frequency dielectric constant in the presence of EP ($\Delta\varepsilon_{EP} = \varepsilon_{r,EP} - \varepsilon_r$). Here, the PTACCy conductivity is low $\sigma_0 < 10^{-5}\ \frac{S}{cm}$ and the $\tau_{EP} > 1s$ therefore the following simplification is applicable.

$$tan(\delta) = \frac{\omega\tau_{EP}}{1+\omega^2{\tau_{EP}}^2/M} \tag{2.3.3.4}$$

M is defined as the ratio of the sample thickness to twice the Debye length[62]. For confirmation, Figure 2.3.3.1A plots the measured $\sigma'(\omega)$ vs. ω for a range of temperatures spanning 303 –

$493K$. The σ_0 can be located in the $\sigma'(\omega)$ frequency dependence by the characteristic plateau and the σ_0 is equivalent to the $\sigma'(\omega)$ plateau value. Figure 2.3.3.1B plots the PTACCy σ_0 temperature dependence, and strikingly, we observe an Arrhenius-type behavior across the entire temperature regime.

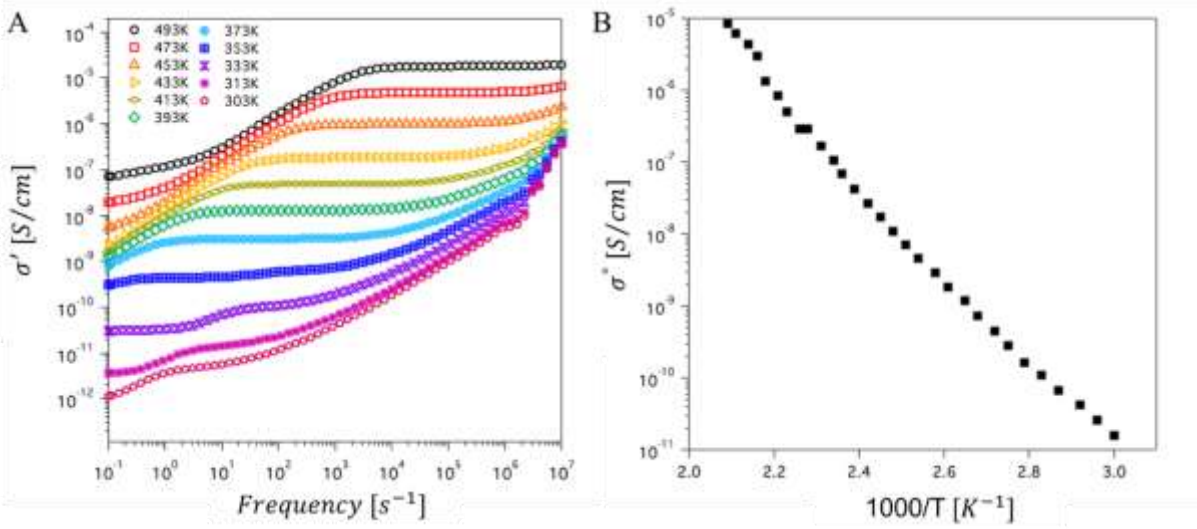

Figure 2.3.3.1. Neat PTACCy homopolymer conductivity frequency and temperature dependence. (A) the PTACCy ionic conductivity frequency dependence plotted for a range of experimental temperatures $(303 - 493K)$. (B) The PTACCy σ_0 plotted vs. $1000/T$ where T is experimental temperature.

In addition to the sample conductivity, we determined the PTACCy $\varepsilon'(\omega)$ and $\varepsilon''(\omega)$ frequency dependence across a wide temperature window $(303 - 493K)$. Figure 2.3.3.2A and Figure 2.3.3.2B plot the PTACCy $\varepsilon'(\omega)$ and $\varepsilon''(\omega)$ frequency dependence.

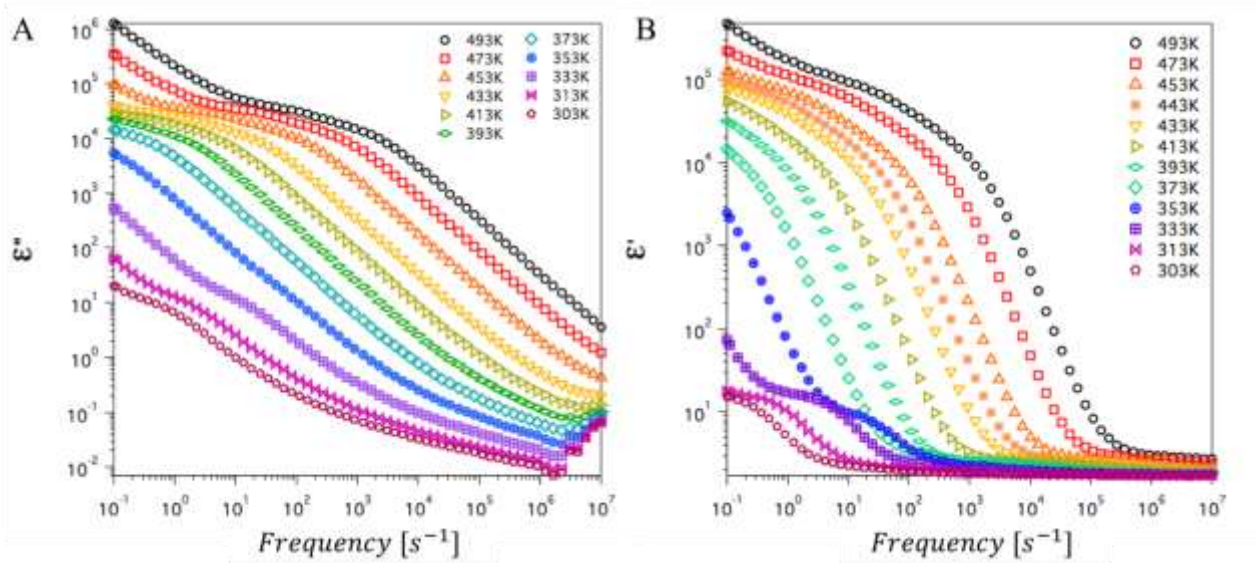

Figure 2.3.3.2. The PTACCy ε' and $\varepsilon^{"}$ frequency dependence. The PTACCy (A) ε' and (B) $\varepsilon^{"}$ frequency dependence plotted for a range of experimental temperatures $(303 - 493K)$.

Each of these curves were transformed into $tan(\delta)$ using the $tan(\delta) = \varepsilon^{"}/\varepsilon'$ transformation for each temperature. Figure 2.3.3.3 plots an example of this transformation for $T = 353K$. The open blue, red, and black circles are the PTACCy $\varepsilon^{"}(\omega)$, $\varepsilon'(\omega)$, and $\tan\delta$ respectively. The solid black and blue lines are fits to the $tan(\delta)$ and $\varepsilon'(\omega)$ with a single Debye relaxation and an electrode polarization procedure outline in greater detail elsewhere and briefly described in this section[62].

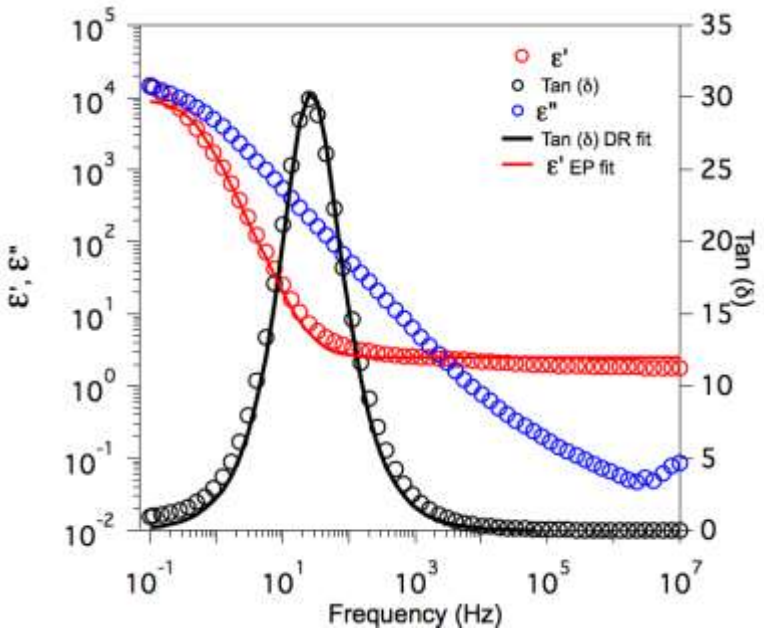

Figure 2.3.3.3. An example calculation of electrode polarization analysis. A Plot of the PTACCy ε', $\varepsilon^{"}$, and $\tan\delta$ frequency dependence plotted in open red, blue and black circles for $T = 353K$). The solid black and blue lines are a single Debye relaxation and electrode polarization fits to the $\tan\delta$ and ε' data.

The $tan(\delta)$ is then modeled as a single Debye relaxation process for temperatures ranging from 303 – 493K and the obtained values were substituted into Eq (2.3.3.5) and fit the $\varepsilon'(\omega)$.

$$\varepsilon'_{EP} = \varepsilon_r + \Delta\,\varepsilon_{EP}/(1+\omega^2\tau_{EP}) = \varepsilon_r + (\mathrm{M}-1)\varepsilon_r/(1+\omega^2\tau_{EP}) \qquad (2.3.3.5)$$

The value ε_r was used as a fitting parameter to obtain agreement at the high frequency plateau before the onset of electrode polarization. This procedure was used to determine the temperature dependence of the static dielectric constant (ε_R). The obtained ε_r values from the electrode polarization analysis are plotted in Figure 2.3.3.4 (red circles). A black straight dotted line is fit through all temperatures that were amenable for this fitting procedure, *i.e.* the full electrode polarization was observed within the experimental frequency window. Across the entire temperature range probed we obtained a relatively constant static ε_r at $\varepsilon_r = 2.5 - 3$. For

comparison, a second approach was utilized to measure ε_r. Since the $\sigma_o < 10^{-5}\ \frac{S}{cm}$ the observed high frequency plateau in $\varepsilon'(\omega)$ can be taken as a direct measurement of ε_r and extracted from the experimental data. This method, although only an approximation, is shown in Figure 2.3.3.4 (black squares). Both methods agree within a reasonable margin of error, however, using the high frequency plateau produces a slight increasing trend in ε_r with increasing experimental temperature is observed.

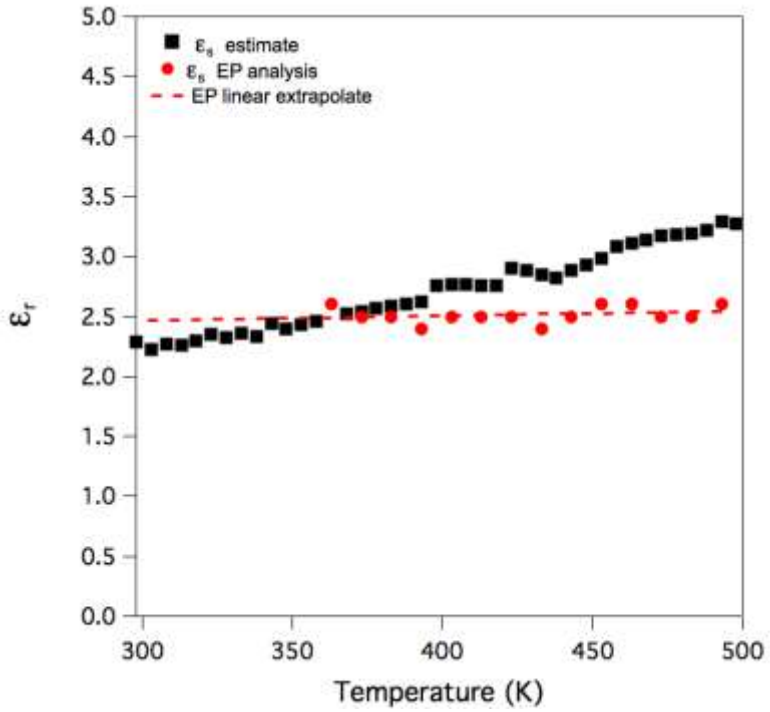

Figure 2.3.3.4. The neat PTACCy homopolymer ε_r temperature dependence. The temperature dependent static dielectric constant. The open blue circles were obtained through fitting ε' and then extrapolated to room temperature. The open pink triangles were obtained from reading the ε' high frequency plateau.

From the dielectric analysis we find the PTACCy homopolymer has unusual dielectric properties[63] determined using a previously described procedure.[62] We determined the dielectric constant across all experimentally accessible temperatures to be significantly lower ($\varepsilon_r \sim 2.5 – 3.0$) than the reported values for most other cationic polyelectrolytes ($\varepsilon_r \sim 12 – 120$)[64–67]. Figure 2.3.3.5

explicitly shows that PTACCy is outside the conventional range (black circle) when compared to the dielectric constants of other cationic polyelectrolytes (blue = imidazolium-based polymers, IM; green = ammonium-based polymers, AM). A large difference in size ($m_b/m_c \gg 1$) and delocalized nature of TAC ions may be related to its exceptionally low ε_r which translates to a large Bjerrum length (l_B ~ 22 nm at room temperature). The m_b and m_c parameters represent the mass of the ion bound to the polymer electrolyte backbone and counterion respectively.

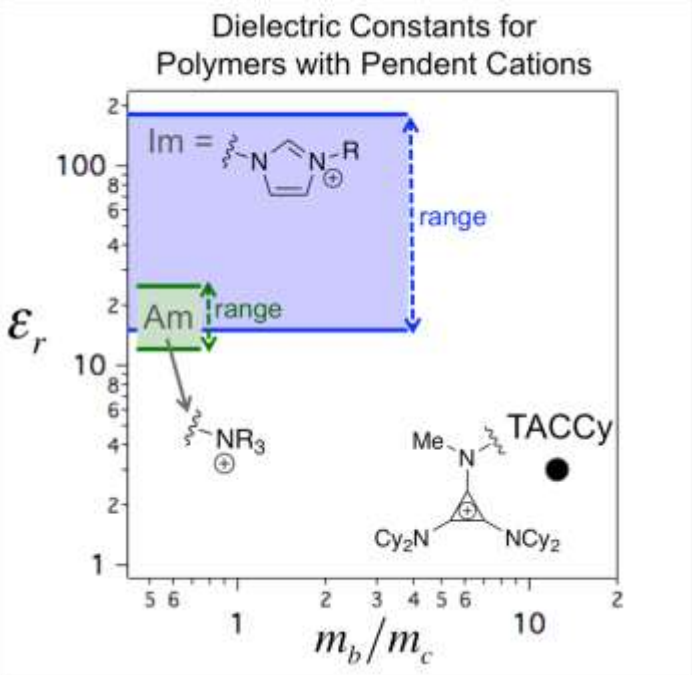

Figure 2.3.3.5. The relationship between ion size and dielectric constant for cationic polymer electrolytes. A Summary of cationic polymer electrolyte dielectric constants. The dielectric constant, ε_r, is plotted as a function of the ratio between the masses of the ion covalently bound to the polyelectrolyte backbone (m_b) to the associated counterion (m_c). The blue and green regions correspond to reported ε_r values of various imidazolium and quaternary ammonium polymer electrolytes respectively, and the black circle marks the PTACCy location[64,65,67,68]

Additionally, the PTACCy glass transition temperature (T_g = 130 °C) is higher than that of the neutral PS block, and the ionic conductivity (σ_0) is exceptionally low (σ_0~10^{-7} S/cm at 130 °C). These characteristics are indicative of ion aggregation, which is consistent with strong electrostatic interactions ($l_B \gg 1$) arising from the low PTACCy dielectric constant. While the low

static dielectric constant is not ideal for ion-transport applications, the fundamental contributions of this work reveal is enunciating the role of ion correlations on CN-BCP microphase segregation.

2.4 Summary of PS-*b*-PTACCy bulk self-assembly – generalization of CN-BCP morphology diagrams.

To characterize the PS-*b*-PTACCy morphology behavior we synthesized a series of CN-BCPs of various volume fractions. All prepared materials can be found in Table 2.2.1.1 along with a compressive list all PS-b-PTACCy CN-BCP physical properties. The CN-BCPs were dissolved in methylethylketone (100 mg/mL), cast from solution, and dried to form freestanding films. The films were subjected to thermal annealing under vacuum (up to 1 week at 150 °C); however, this annealing has no measurable effect on the CN-BCP morphology, presumably due to the strong ionic interactions that hamper ready equilibration. Thus, at the very least, it is apparent that these structures cannot be viewed as thermal equilibrated morphologies as they are possibly affected by the presence of solvent during casting. Nevertheless, each material was subjected to the same processing pathway and will be characterized to examine relative changes across the entire set. Each PS-b-PTACCy free standing film was encased in epoxy, microtome into ~100 nm thick slices, and imaged using transmission electron microscopy (TEM).

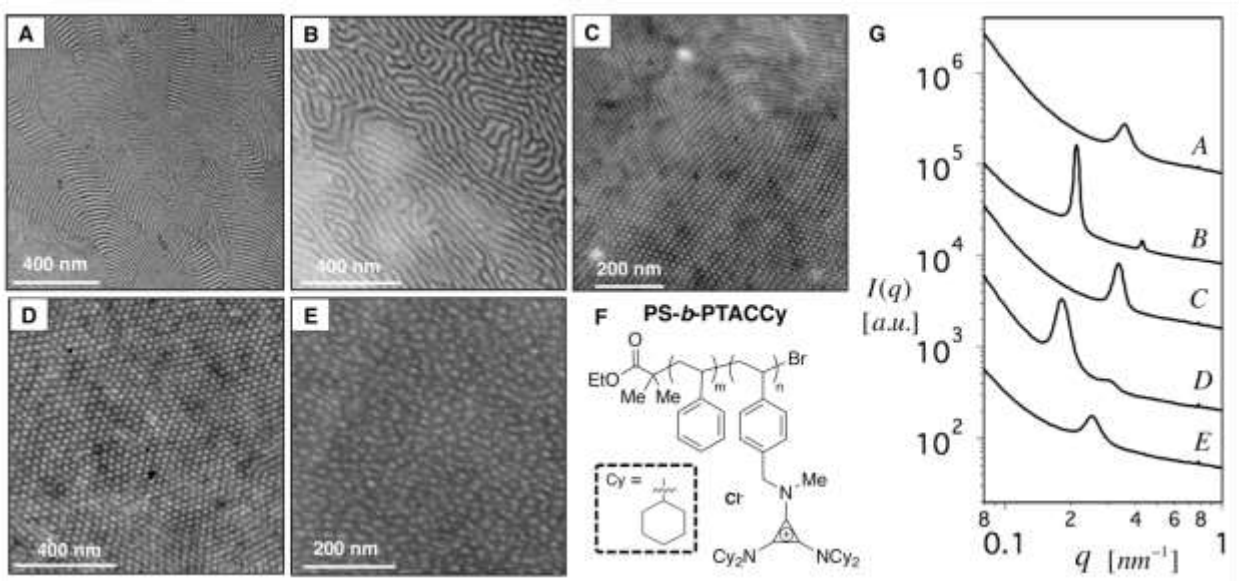

Figure 2.4.1. The morphology of PS-*b*-PTACCy bulk films. TEM images of (A & B) LAM, (C & D) C_N, and (E) S_N forming PS-*b*-PTACCy CN-BCPs. (F) A schematic of the PS-*b*-PTACCy chemical structure. (G) SAXS curves corresponding to the presented TEM images of the observed PS-*b*-PTACCy morphologies. Note: All the physical data corresponding to the presented PS-*b*-PTACCy samples are labeled in Table 1.

In each case, the uncharged PS block forms the discrete phase, as confirmed by selective staining with OsO_4 and imaging by TEM (Figures 2.4.1A-E). The morphologies labeled with a subscript N (*i.e.* $cylinder_N$) correspond to structures that have the polyelectrolyte block forming the continuous matrix. For PS-*b*-PTACCy CN-BCPs we employed two complementary methods to quantify the PTACCy block volume fraction (ϕ_{CN-BCP}): (1) combining information gathered from SAXS and TEM image analysis and (2) ^{1}H-NMR spectroscopy in conjunction with the known bulk densities for each block. We found excellent agreement between both methods, confirming our assignments (see Table 2.2.1). It is important to note that ϕ_{CN-BCP} quantifies the fraction of volume occupied by the PTACCy block (including the chlorine counterion) of the total CN-BCP volume, and used generally to describe the polyelectrolyte block volume fraction for all examined CN-BCPs examined.

Returning to the morphological analysis, while the PS-*b*-PTACCy CN-BCPs TEM micrographs provide compelling structural information, we confirmed all assignments using SAXS. Figure 2.4.1 includes TEM micrographs for a selected set of samples and their corresponding SAXS curves (Figure 2.4.1G). All lamellar-forming CN-BCPs display higher order reflections corresponding to peak ratios of q^*: $2q^*$ consistent with the lamellar structure factor, and peak ratios of q^*: $\sqrt{3}q^*$ for all cylinder$_N$-forming (C_N) CN-BCPs, indicating the domains are hexagonally close packed. In both cases q^* is defined as the q position of the primary reflection peak intensity. The SAXS patterns only contain a few higher order reflections presumably due to the lack of persistent long-range ordering. This is illustrated in Figure 2.4.1E which corresponds to a PS-b-PTACCy sphere$_N$-forming (S_N) CN-BCP and the corresponding SAXS curve only contains a single structural reflection. Why the data corresponding to Figure 2D, for example, which show much more order have only two peaks remains unclear to us, except that the lack ordering might occur at much larger scales

Having synthesized PS-*b*-PTACCy polymers with varying compositions, we compiled a morphology diagram, shown in Figure 2.4.5A, for this class of materials. Figure 2.4.2B has data for corresponding systems, but ones where the dielectric constant of the media are typically >10. For convenience, the morphological data provided in Figure 2.4.5A and Figure 2.4.5B are color-coded based on CN-BCP cation identity, and the cation structure is provided underneath each plot respectively. In Figure 2.4.5A, the black data points correspond to the PS-*b*-PTACCy CN-BCPs where the TEM and SAXS characterization for each sample. Figure 2.4.2A-J provides example TEM images for all PS-b-PTACCy CN-BCPs examined in this section.

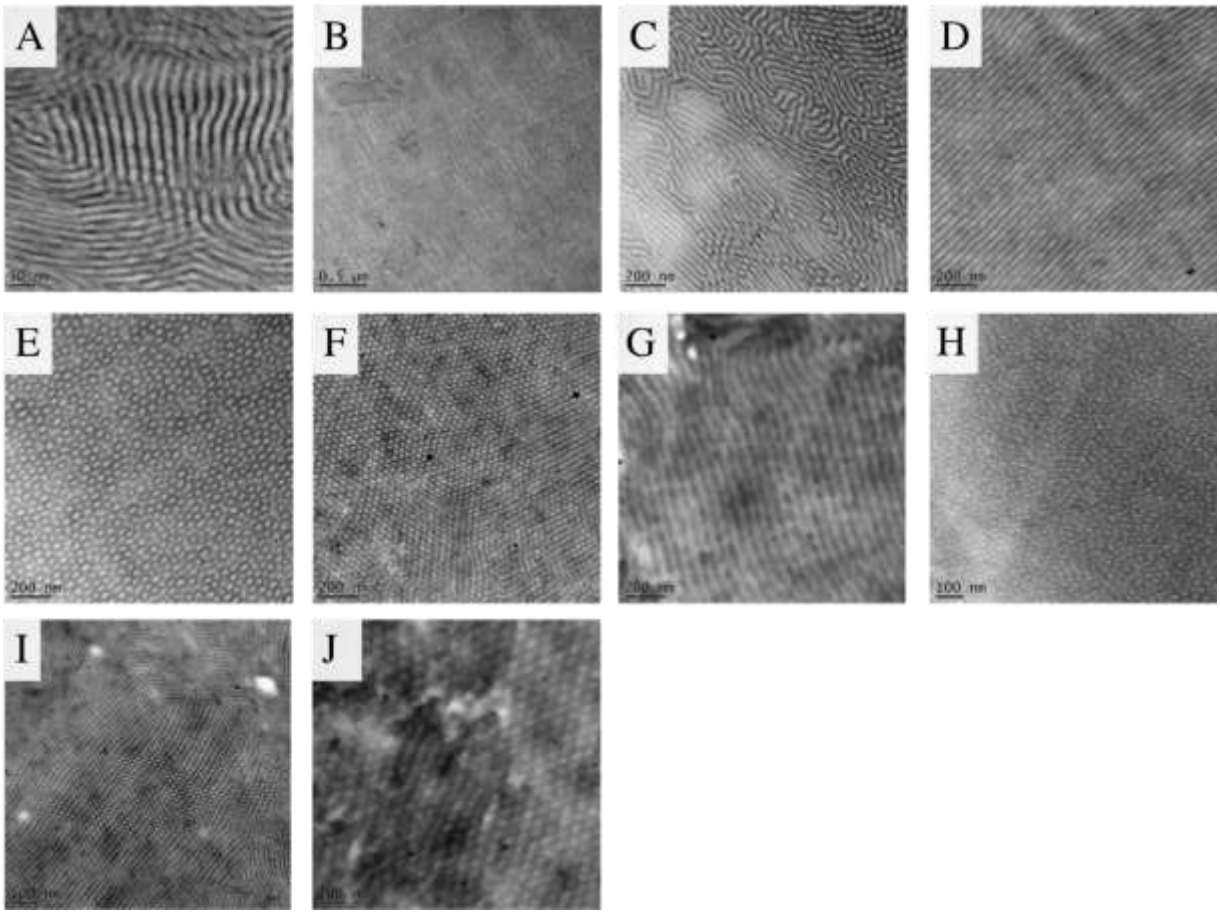

Figure 2.4.2. A Summary of the TEM micrographs taken for all PS-*b*-PTACCy bulk films. The TEM micrographs taken of PS-b-PTACCy CN-BCP bulk self-assembly after casting and annealing for (A) $N = 140, \phi_{CNBP} = 0.31$, (B) $N = 150, \phi_{CNBP} = 0.38$, (C) $N = 200, \phi_{CNBP} = 0.44$, (D) $N = 175, \phi_{CNBP} = 0.61$, (E) $N = 235, \phi_{CNBP} = 0.66$, (F) $N = 195, \phi_{CNBP} = 0.72$, (G) $N = 220, \phi_{CNBP} = 0.77$, (H) $N = 220, \phi_{CNBP} = 0.89$, (I) $N = 115, \phi_{CNBP} = 0.60$, (J) $N = 265, \phi_{CNBP} = 0.74$.

As stated previously, across all the prepared PS-*b*-PTACCy CN-BCP samples we observed only three unique morphologies: LAM, C_N, and S_N. However, it is important to note that identifying and labeling morphologies using only TEM images can lead to incorrect assignments. For example, Figure 2.4.2B could be the LAM morphology due to the characteristic fingerprint nature of the planar domains, however, it could also appear be C_N demonstrated by the circular PS domains. With the level of ambiguity, it is paramount to confirm the assignments using and complimentary technique – small angle x-ray scattering (SAXS). SAXS probes a much large

sample cross-section and will provide a statistical average of PS-b-PTACCy morphology within the scattering cross-section. SAXS was conducted for all PS-b-PTACCy CN-BCPs and the results are present in Figure 2.4.3A-C and Figure 2.4.4.

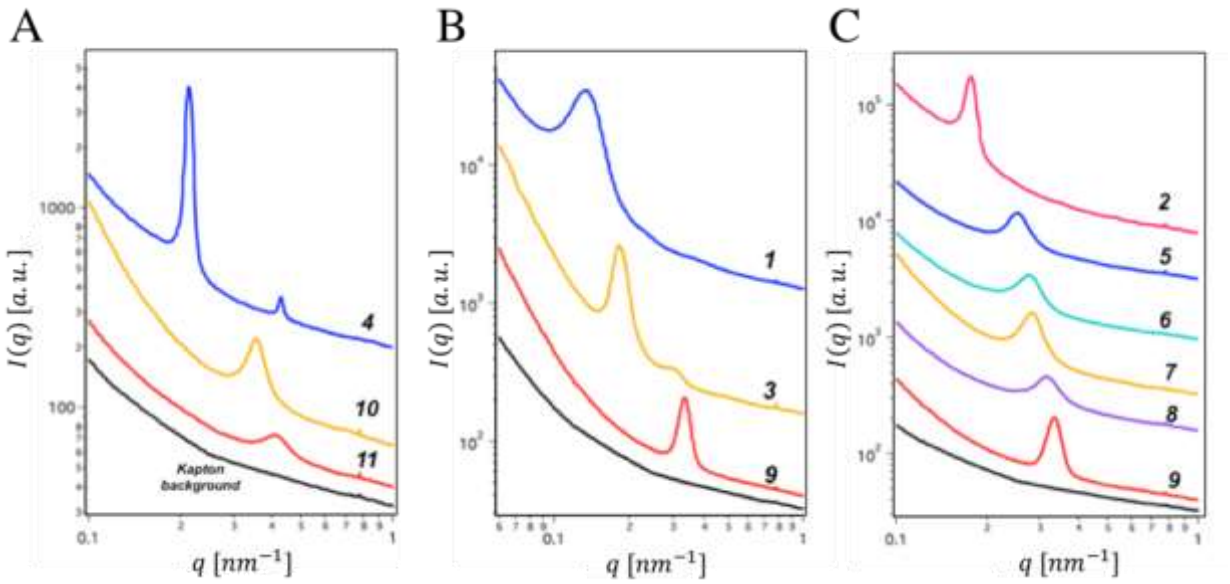

Figure 2.4.3. A Summary of the SAXS taken on all PS-*b*-PTACCy bulk films. The SAXS intensity $I(q)$ vs. the scattering vector q for self-assembled PS-*b*-PTACCy bulk CN-BCPs (1)$N = 265, \phi_{CNBP} = 0.74$, (2)$N = 235, \phi_{CNBP} = 0.66$, (3)$N = 220, \phi_{CNBP} = 0.77$, (4)$N = 200, \phi_{CNBP} = 0.44$, (5)$N = 220, \phi_{CNBP} = 0.89$, (6) $N = 165, \phi_{CNBP} = 0.82$, (7) $N = 150, \phi_{CNBP} = 0.78$, (8) $N = 120, \phi_{CNBP} = 0.85$, (9)$N = 115, \phi_{CNBP} = 0.60$, (10)$N = 150, \phi_{CNBP} = 0.38$, (11)$N = 140, \phi_{CNBP} = 0.31$.

The Figure 2.4.3 and Figure 2.4.4 summarize all SAXS experiments conducted on the PS-*b*-PTACCy CN-BCPs which were done at Brookhaven National Lab (BNL) on the 11-BM complex materials scattering beamline and using the Columbia soft matter lab source respectively. In Figure 2.4.3, the plots are separated by PS-*b*-PTACCy morphological structure where Figure 2.4.3A-C correspond to LAM, C_N, and S_N forming PS-b-PTACCy CN-BCPs respectively. The structures are determined by the relationships between observed peak intensities. All LAM and C_N forming CN-BCPs display higher order reflections corresponding to peak ratios of $q^*: 2q^*$ and $q^*: \sqrt{3}q^*$ respectively, and the S_N forming CN-BCPs only displayed a single refection. In Figure

2.4.4 SAXS curves labeled 12, 13, and 14 correspond to Lam, C_N, and C_N – forming PS-*b*-PTACCy CN-BCPs respectively.

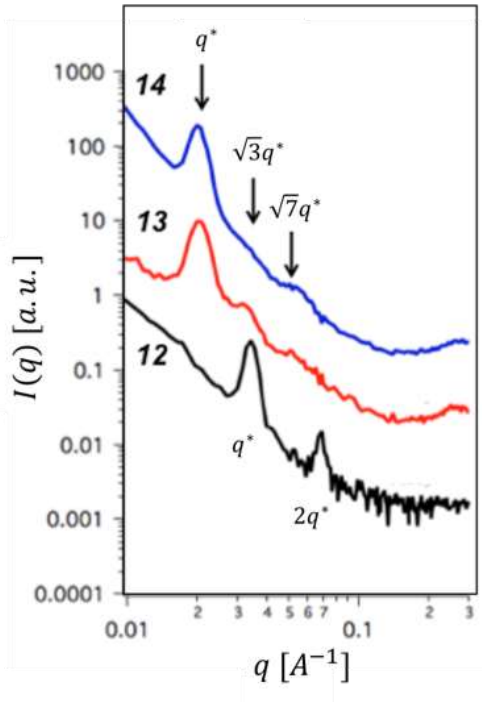

Figure 2.4.4. SAXS results for PS-*b*-PTACCy bulk films taken on the lab source. The SAXS intensity $I(q)$ vs. the scattering vector q for self-assembled PS-*b*-PTACCy bulk CN-BCPs (12)$N = 140, \phi_{CNBP} = 0.33$, (13) $N = 175, \phi_{CNBP} = 0.61$, (14) $N = 195, \phi_{CNBP} = 0.72$

All of the information obtained from SAXS and TEM was used to compile a PS-b-PTACCy morphology diagram show in Figure 2.4.5A. The morphology diagram shows boundaries between the S_N, C_N, and LAM phases that are significantly skewed toward the low ϕ_{CN-BCP} in comparison with the strong segregation limit (SSL) transitions found in BCPs.[69] In particular, we find the C_N-to-LAM boundary for this system to be at $\phi_{CN-BCP} \sim 0.4$ and shifted dramatically compared to the corresponding SSL value at $\phi_{CN-BCP} = 0.66$. The asymmetry in the diagram suggests that these CN-BCPs prefer morphologies that have matrices comprised of the PTACCy block even when it is the volumetric minority component. Further, we also include the recent morphological results on tris(2,4,6-trimethoxyphenyl)phosphonium-containing CN-BCPs

(S-Phos, red data points) in Figure 2.4.5A. The S-Phos motif has a similar chemical architecutre to that of TACCy, and the S-Phos-containing CN-BCPs display similar asymetrical morphological behavior.[70] We compare such striking results to other conventional cationic CN-BCPs systems in Figure 2.4.5B, which contains published data of imidazolium (IM, blue data points), quaternary ammonium (AM, green data points), and tributylphosphonium-containing CN-BCPs (H-Phos, orange data points).[25,27,71–73] The data in Figure 2.4.5B, are more in agreement with the behavior of conventional BCP SSL transitions marked by the dashed black lines.[69] To explain these large difference in morphology diagrams we highlight the stark contrast between the reported S-Phos and H-Phos morphological behavior. We conjecture that their dramatically different functionalities (likely the differences in bulkiness of the side groups) leads to these dramatically different morphological results. The observed differences for these CN-BCPs are consistent with our hypothesis that bulky and highly delocalized ionic units can behave drastically different than the more conventional hard ions. However, a more quantitative and mechanistic description of this effect remains outstanding.

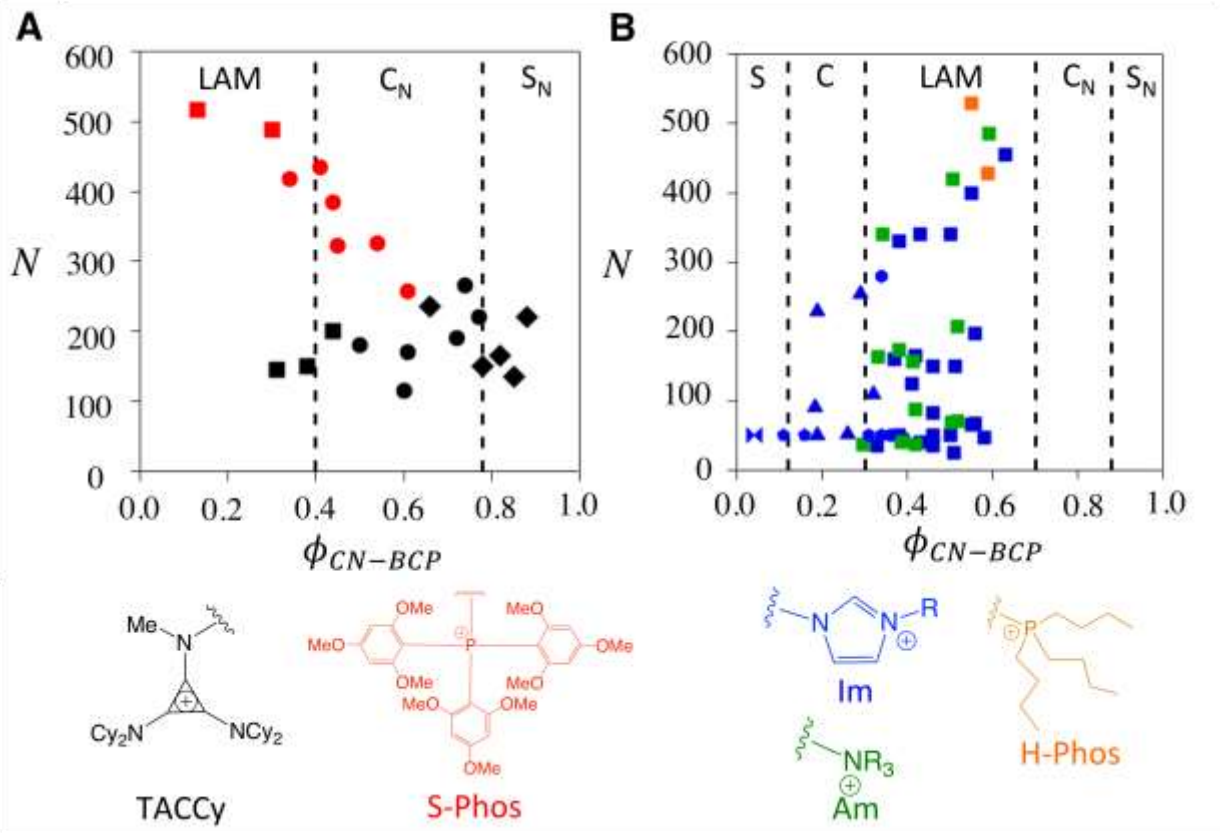

Figure 2.4.5. Morphology diagrams of CN-BCPs exhibiting (A) strong vs. (B) weak electrostatic interactions. (A) Data collected for PS-*b*-PTACCy (black symbols) and tris(2,4,6-trimethoxyphenyl)phosphonium-containing (red symbols) CN-BCPs[70] (squares = LAM, circles = C_N, diamonds = S_N). Note the black dotted lines (---) are used to guide the eye. (B) The dashed lines (---) correspond to the BCP strong segregation limit transitions and the data correspond to reported morphologies for various imidazolium (blue symbols), quaternary ammonium (green symbols), and tributylphosphonium (orange symbols) containing CN-BCPs (squares = LAM, hexagons = LAM/C, triangles = C, pentagons = S, bowtie = disordered)[25,27,71–73]. The chemical structures of the discussed ionic moieties are provided underneath and color-coded to match their representative morphological data.

While it is mechanistically unclear how charge delocalization impacts CN-BCP microphase segregation, we will attempt to correlate the polyelectrolyte's static dielectric constant, a parameter directly related to the strength of ion interactions, to the CN-BCP morphology diagrams. As mentioned previously, the IM and AM-containing CN-BCPs have high dielectric constants and thus low ion correlation lengths where $l_B \sim 0.5 - 4$ nm. The PS-b-PTACCy CN-BCPs, on the other hand, have $l_B \sim 19 - 22$ nm (at least an order of magnitude larger). We

postulate that the stark contrast between the two morphology diagrams in Figure 2.4.5 arise from the large difference in ion correlation length scale. Some studies have hinted at shifts in morphology diagrams from polarizable groups, but these do not account for the drastic changes observed in Figure 2.4.5.[74–76] In the following sections and chapter 3, we present additional experimental observations and a simple theoretical framework coupled with a generalizable scaling model to rationalize the extended C_N morphological regime in the PS-*b*-PTACCy morphology diagram respectively. The excellent agreement between the generalized scaling model and the morphology potentially elucidates the physical phenomena underpinning these results while providing a pathway towards rationalizing the development of additional CN-BCPs that may demonstrate the same asymmetric morphological behavior.

2.5 Quantification of PS-*b*-PTACCy PTACCy chain conformation and the impact of strong ionic interactions

In the section we demonstrate the impact of strong Coulombic interactions on the PS-b-PTACCy chain conformations. For this, we turn to an in-depth analysis of PS-*b*-PTACCy CN-BCP SAXS data. We compare the observed microphase-segregated periodicity (*d*) to the overall CN-BCP polymer chain length (*N*) for all classes of CN-BCPs presented in Figure 2.4.5. Figure 2.5.1A plots *d vs. N* for PS-*b*-PTACCy (black filled circles), IM-containing CN-BCPs (blue open triangles)[72], AM-containing CN-BCPs (green open squares)[72], and H-Phos-containing CN-BCPs (orange open diamonds).[73] For each PS-*b*-PTACCy sample, the peak position of the primary reflection (q^*) is used to calculate the domain spacing according to the following relationships, $d_{LAM} = 2\pi/q^*$, $d_{cyl} = 2\pi\sqrt{4/3}/q^*$, and $d_{sph} = 2\pi\sqrt{3/2}/q^*$, for lamellar, HCP cylinders, and close-packed sphere-forming CN-BCPs, respectively. The data set was fit to $d \sim N^{\nu}$, where the exponent ν provides information regarding the chain conformation. This procedure was followed

for the PS-*b*-PTACCy CN-BCPs, and the values of $d, N,$ and ν for the IM, AM, and H-Phos-containing CN-BCPs were taken from literature.[72,73] For reference, for traditional BCPs, where strong segregation theory applies, we expect $\nu = 2/3$.[69]

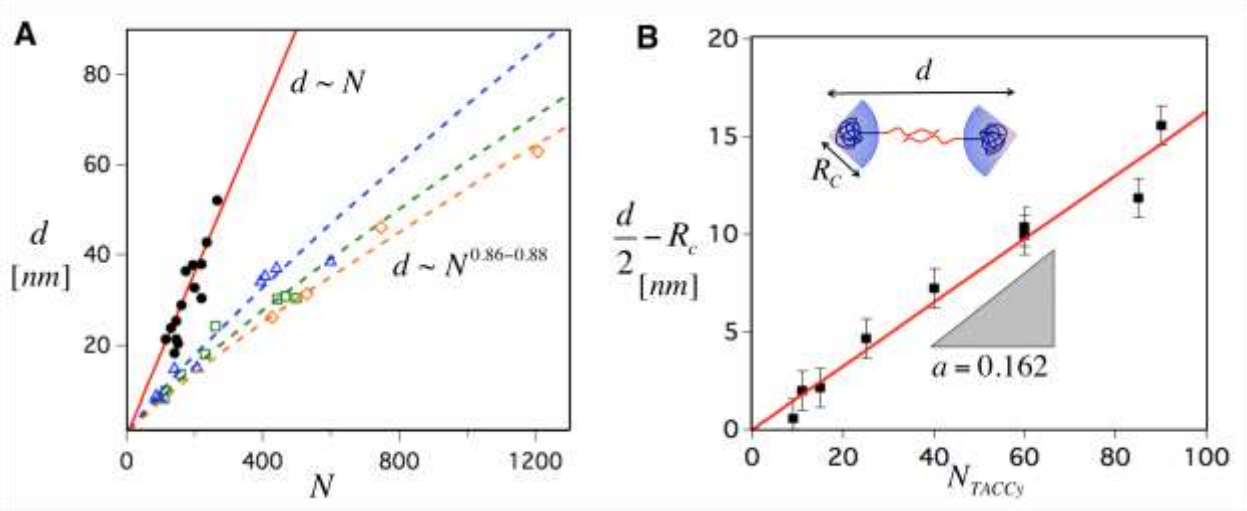

Figure 2.5.1. Quantification of PTACCy matrix chain rigidity. (A) A plot of the experimental domain spacing vs. CN-BCP total degree of polymerization for various CN-BCPs.[72,73] (B) A plot of the PTACCy contribution to the PS-b-PTACCy periodicity as a function of increasing PCPCy chain length. The solid red line is a linear fit to the data with a fixed y-intercept at the origin.

At the other extreme, $\nu = 1$ represents a rigid-rod polymer chain, and thus we expect the various CN-BCPs to fall somewhere between these two limits. Interestingly, we find that PS-*b*-PTACCy has rigid-rod-like scaling ($\nu = 1$), unlike other cationic CN-BCPs, where ν = 0.86 - 0.88. This indicates that the PS-*b*-PTACCy CN-BCP chains are more extended in comparison with the other cationic CN-BCPs, and a result that supports the observed enhanced PTACCy ion correlation length scale.[54]

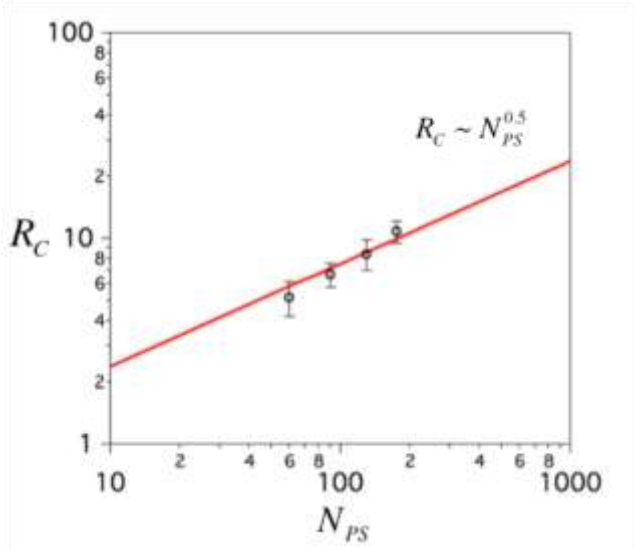

Figure 2.5.2. The PS contribution to the Ps-b-PTACCy chain conformation. The red link is a power law fit constrained by $R_C = 0$ at $N_{PS} = 0$. The best-fit exponent is 0.5 indicating the PS block maintains a gaussian conformation within the domain.

To further interrogate the results in Figure 2.5.1A, we plot the PTACCy contribution to the domain length, $d/2 - R_c$, where R_c is the average radius of the PS domain, against the number of TACCy monomers (N_{TACCy}, Figure 2.5.1B). We find a linear relationship between $d/2 - R_c$ and N_{TACCy}, confirming that the matrix TACCy chains are fully extended. From the slope of this line we determined the effective TACCy monomeric contribution to $d/2 - R_c$, from which we relate the extent of PTACCy matrix chain interpenetration. For a fully interpenetrating PTACCy matrix, we would expect the apparent monomeric spacing to be 0.115 nm, corresponding to half of the monomeric backbone contour length (l_{TACCy}). Alternatively, for a non-interpenetrating matrix, the apparent monomeric spacing will equal l_{TACCy}. The measured apparent monomer spacing is 0.16 nm showing that the PTACCy chains partially interpenetrate which might serve as a mechanism to maximize ionic correlations and maintain a constant density throughout the PTACCy matrix. For completeness, we also examine the PS chain conformation. Figure 2.5.2 plots R_c as a function of the number of styrene monomers, N_{PS}, and we find $R_c \sim N_{PS}^{0.5}$, indicating that the PS chains maintain their Gaussian coil scaling within the domain. Note that the red line in Figure 2.5.2 is a

best-fit $R_c \sim N_{PS}^{0.5}$ power law to the experimental data (open black circles). The experimental data was obtained from image analysis of the TEM micrographs. Here R_c denotes the radius of the polystyrene domain and N_{PS} is the degree of polymerization of the polystyrene block. If we consider a composite conformation for the entire PS-*b*-PTACCy CN-BCP we conclude that these materials form a rod-coil chain conformation. Typically rod-coil polymers contain a conjugated polymer as the rigid component, whereas here we demonstrate how an ionic block based copolymer can achieve the same rod-conformation.[77]

2.6 PS-*b*-PTACCy PTACCy self-assembly in the presence of doped salt – the effect of charge screening

In this section, we first demonstrate that the extended PTACCy chain conformation arises from ionic considerations to compliment the results found in section 2.5. For a single PS-*b*-PTACCy CN-BCP (N = 220, ϕ_{CN-BCP} = 0.77), we selectively doped lithium bis(trifluoroamethanesulfonyl)amide (Li^+TFSI^-) salt into the PTACCy matrix to screen the strong electrostatic interactions. Figure 2.6.1A plots SAXS curves for a series of salt loadings ranging from ϕ_{salt} = 5.0 x 10^{-5} - 5.0 x 10^{-2}, where ϕ_{salt} is the volume fraction of doped salt in the PS-*b*-PTACCy CN-BCP. In Figure 2.6.1B we plot the Lorenz correct SAXS curves focusing only on the primary reflection – the regime where we expect to see the greatest impact from screened interactions. We quantify the impact of salt doping by obtaining the doped CN-BCP periodicity using $d = 2\pi\sqrt{4/3}/q^*$, accounting for the hexagonal geometry displayed in Figure 2.6.1C, as well as the hexagonal grainsize, approximated using the full width half maximum (FWHM) of the distribution. The fitting results and analysis are provided in Table 2.6.1.

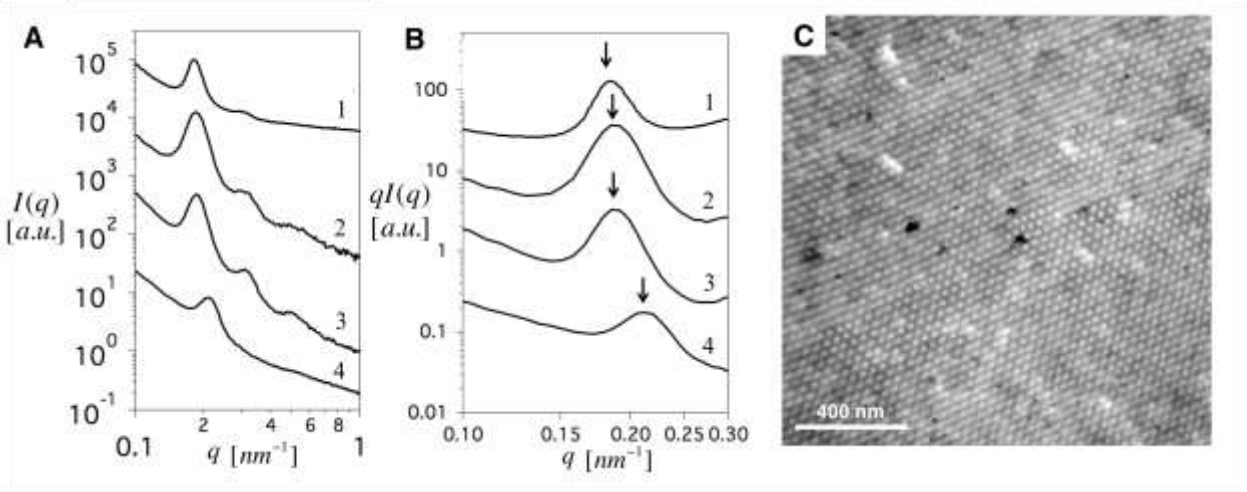

Figure 2.6.1. CN-BCP chain conformations and effect of salt doping. (A) SAXS curves for the PS-*b*-PTAC CN-BCP (N = 220, ϕ_{CN-BCP} = 0.77) doped with various amounts of Li^+TFSI^- salt ($\phi_{salt} = 0$ (1), $\phi_{salt} = 5.0 \times 10^{-5}$ (2), $\phi_{salt} = 5.0 \times 10^{-4}$ (3), and $\phi_{salt} = 5.0 \times 10^{-2}$ (4)) (B) Lorenz corrected SAXS curves highlighting the primary reflection for all salt doped PS-*b*-PTACCy CN-BCP (N = 220, ϕ_{CN-BCP} = 0.77). The entire q range can be found in Figure S26 of the Supporting Information. (C) A TEM micrograph of PS-*b*-PTACCy CN-BCP (N = 220, ϕ_{CN-BCP} = 0.77) doped with $\phi_{salt} = 5.0 \times 10^{-4}$ Li^+TFSI^- salt.

For low salt loadings (ϕ_{salt} < 5.0 x 10^{-2}), the selective addition of salt in the PTACCy matrix enhances the contrast between the PS domain and PTACCy relative to the salt free CN-BCP (Figure 2.6.1A, trace 1). This is apparent in Figure 2.6.1A as traces labeled (2) and (3) have an increased number of higher order hexagonal reflections (q^*: $\sqrt{3}q^*$: $\sqrt{7}q^*$); however, the FWHM for these traces have also increases compared to trace (1), the salt-free sample. The increase in FWHM indicates the hexagonal grain size has decreased, and this effect is consistent throughout all salt-doped samples compared to the salt-free case. This suggests that salt selective infiltrates the PTACCy matrix and does not increase the persistence of ordering but instead provides a higher contrast between the PS domain and the PTACCy matrix. The increased electron density contrast allows for the observation of higher order hexagonal reflections.

Table 2.6.1. A summary of parameters for LiTFSI doped PS-b-PTACCy ($N = 220, \phi_{CNBP} = 0.77$).

Sample Name	Salt volume fractions (ϕ_{Salt})[b]	q^* (nm^{-1})[b]	FWHM (nm^{-1})[b]	R_C (nm)[c]
(a) Salt Free	0	0.183	0.0336	10.6 ±0.9
(b) 0.0001M LiTFSI	$5.0x10^{-5}$	0.188	0.0456	——
(c) 0.001M LiTFSI	$5.0x10^{-4}$	0.189	0.0402	10.5 ±0.9
(d) 0.01M LiTFSI	$5.0x10^{-3}$	0.189	0.0454	10.2 ±0.9
(e) 0.1M LiTFSI	$5.0x10^{-2}$	0.2107	0.0496	——

[a]The salt volume fraction was calculated using the CN-BCP mass, $\phi_{CN\text{-}BCP}$, Li^+TFSI^- density (1.33 g/cm^3), and the Li^+TFSI^- mass loading. [b]The q^* and FWHM were determined by fitting the Lorenz corrected primary bragg reflection to a normal distribution. [c]The R_c was determined by image analysis using ImageJ software.

In addition to the grain size, we also find a relationship between salt loading and the PS-*b*-PTACCy CN-BCP periodicity. The inclusion of salt in PS-*b*-PTACCy CN-BCPs promotes a reduction in periodicity relative to the salt free case as shown by the primary reflection shift to higher q in Figure 2.6.1B.

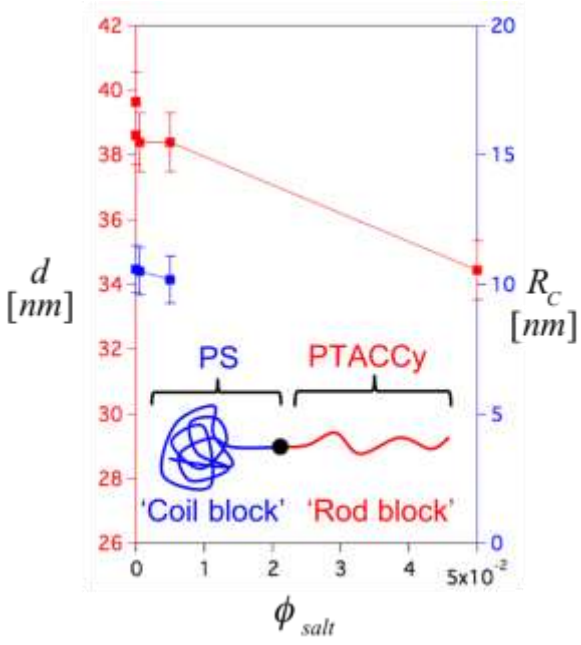

Figure 2.6.2. The impact of salt doping on the PS-b-PTACCy periodicity. A plot of the PS-*b*-PTAC CN-BCP ($N = 220$, $\phi_{CN-BCP} = 0.77$) periodicity (filled red squares, d) and PS domain radius (filled blue squares, R_c) vs. salt loading ϕ_{salt}. A schematic representation of the PS-b-PTACCy chain architecture is provided as an inset.

In order to attribute the decrease in periodicity to screened ionic interactions, we first rule out the possibility that it is associated with changes in the PS domain size. We find the changes in R_c with increasing salt loading to be within the uncertainty of the image analysis measurement, and therefore to be statistically insignificant. At low salt loadings ($\phi_{salt} < 5.0 \times 10^{-2}$), we also find the decrease in CN-BCP periodicity to also be within the uncertainty of R_c ($\pm$0.9 nm), and thus we are unable to definitively confirm where the decrease originates in this case. However, at high salt loading ($\phi_{salt} = 5.0 \times 10^{-2}$), we find a 4.5 nm decrease in the periodicity, which is significantly larger than the uncertainty in R_c and shows that the reduction arises from the PTACCy matrix. These results are presented in Figure 2.6.2. The filled red and blue squares plot the observed PS-*b*-PTACCy periodicity and R_c vs. ϕ_{salt} respectively. This result supports the conclusion that the rod-like PTACCy chain conformation stems from the strong ionic interactions, and that by using salt dopants we are able to screen the ionic interactions and allow the PTACCy chain to relax into a less extended conformation, thereby reducing the CN-BCP periodicity.

Chapter 3: Thermodynamic and packing parameter rationalization for electrostatically guided PS-b-PTACCy self-assembly

Quantifying impact of ionic interactions on charge – neutral diblock copolymer (CN-BCP) self-assembly remains an evolving area of research. In the previous chapter, we present contrasting CN-BCP morphology diagrams that differ depending on the strength of electrostatic interactions. We determine the electrostatic interaction strength using the Bjerrum length, l_B, a parameter that varies inversely with the static dielectric constant of the polymer electrolyte block (ε_r). In this section, we will scrutinize the experimental results and provide a simple thermodynamic and geometric analysis to rationalize the dominance of the C_N morphology and C_N – LAM transition at $\phi_{CN-BCP} = 0.4$ respsectively. To capture the general behavior of CN-BCP self-assembly we proposed a simple scaling model modified from surfactant self-assembly principles to incorporate the strength of ionic interactions determined by $\Lambda = l_B/b_{PS}$, the Bjerrum length normalized by the PS block Kuhn length. The scaling model was fit to the morphology diagrams presented for $\Lambda \sim 1$ and $\Lambda \gg 1$ with excellent agreement. The simple scaling model elucidates a set of N and ϕ_{CN-BCP} for a given CN-BCP where the morphology diagram is expected to be dominated by electrostatic interactions and promote atypical morphological behavior.

3.1 Justification for the large C_N phase space in the PS-b-PTACCy CN-BCP morphology diagram

In this section we will attempt to justify the extended C_N region in the PS-b-PTACCy morphology diagram using the influence of electrostatic interactions. To do this, we must consider the favorable structural motif that would form in the absence of these interactions. PS-*b*-PTACCy CN-BCPs have a asymmetric conformational architecture akin to conjugated rod-coil block copolymers that have been studied extensively in the literature.[78–80] Due to the conformational asymmetry, weakly segregated rod-coil block copolymers such as poly(alkoxyphenylenevinylene)–*b*–poly(isoprene) predominately form lamellar morphologies[78], and other rod-coil materials have shown a variety of other lamellar-like phases, including zigzag[77], arrowhead, wavy lamellar[77], and smectic-type liquid crystalline phases.[77,81] All of these examples of rod-coil copolymers display a similar morphological characteristic – they form structures with planar interfaces. PS-*b*-PTACCy CN-BCPS exhibit morphologies predominantly with a convex interfacial curvature and in stark contrast with the expected result. This suggests that an additional molecular interaction is not only present in PS-*b*-PTACCy CN-BCPs but also dominant over the conformational considerations that drive rod-coil copolymers into planar structures. One possible explanation is an effective electrostatic repulsion between PTACCy monomers at the PS – PTACCy interface. This effect could be made possible through a surface polarization of PTACCy monomers due to the dielectric contrast between the PS and the PTACCy block ($\varepsilon_r = 2.2$ and $\varepsilon_r = 3$, respectively).[55,82–84]

In this vein, we propose a simple free energy argument to provide insight into the stability of the C_N morphology for these materials. To do this we balance between interfacial tension and electrostatic repulsions from polarized ion pairs.

$$F_{int}/k_BT \sim \gamma\alpha \tag{3.1.1}$$

$$\gamma \sim \chi^{1/2} b_{PS}^{-2} \tag{3.1.2}$$

$$F_{ele}/k_BT \sim e^2/4\pi\varepsilon_0\varepsilon_r k_b T r \tag{3.1.3}$$

The interfacial energy (F_{int}/k_BT) can be written as a product of the interfacial tension[85,86] (γ) and the interfacial area (α), where b_{PS} is the PS segmental length. The interaction parameter χ is known to be a function of temperature, *T*, for BCPs[69] and contain a salt concentration dependence for salt-doped BCPs.[16,30,87] However, for CN-BCPs the true functional form of χ has yet to be fully formulated, and for simplicity we treat it as a constant. The electrostatic repulsions are approximated as point source interactions separated by a distance r and the interaction energy is calculated using Eq (3.1.3). Trigonometric relationships are utilized to combine r and α into a single parameter: the subtended angle between neighboring chains along the PS domain circumference (θ), since R_c is known. A schematic representation of θ is given in Figure 3.1.1. Minimizing these two energetic terms provides the theoretical minimum subtended angle (θ_{min}) for a given χ and ε_r. To compare this theoretical construct to our experimental data, we first determine α by recognizing it to be inversely related to the PS cylinder graft density (σ_{Cyl}).

$$\alpha^{-1} = \sigma_{Cyl} = R_c/2V_{PS,chain} \tag{3.1.4}$$

Due to chain connectivity, the σ_{Cyl} can be calculated using R_C and the volume occupied by a single PS chain, $V_{PS,chain}$. If we consider a small disk of the PS domain of thickness b_{PS}, we can obtain an experimental estimate of the subtended angle between chains (θ_{PS}) using image analysis of the TEM micrographs.

$$\theta_{PS} \cong 360/2\pi R_c b_{PS} \sigma_{Cyl} \tag{3.1.5}$$

For this estimation all PS chains are assumed to be distributed uniformly around the domain circumference. A comprehensive list of the relevant estimated parameters can be found in Table

3.1.1. It is important to note that θ_{min} is the calculated theoretical minimum subtended angle and θ_{PS} is the experimentally estimate subtended angle.

Table 3.1.1. A list of relevant parameters to balance the interfacial energetics.

N_{PS}	R_c [nm]	θ_{PS} [deg]	σ_{cyl} $[chains/nm^2]$	χ
90	9.5 ± 0.9	28 ± 8	0.31 ± 0.06	0.3 ± 0.16
130	11.4 ± 1.4	24 ± 10	0.31 ± 0.08	0.3 ± 0.25
175	13.2 ± 1.3	20 ± 6	0.30 ± 0.06	0.4 ± 0.23

N_{PS} was obtained using GPC calibrated with polystyrene standards. R_c was determined via image analysis of TEM micrographs and averaged over all CN-BCPs with the same PS block. The σ_{cyl} was calculated using R_c and $V_{PS,chain} = N_{PS}MW_{mon}/N_A\rho_{PS}$ where MW_{mon}, N_A, and ρ_{PS} are the monomer molecular weight, Avogadro's number, and polystyrene bulk density respectively. The reported χ is an estimated value that satisfies the θ_{min} criterion.

With R_c, θ_{PS}, σ_{Cyl}, and ε_r known, we can use our model to obtain an order of magnitude estimation of χ for PS-*b*-PTACCy CN-BCPs. Figure 3.1.1 plots $F/k_BT = (F_{int} + F_{ele})/k_BT$ as a function θ for a $R_c = 11.4$ nm ($N_{PS} = 130$), $\sigma_{Cyl} = 0.3$, ε_r= 3, and $\chi = 0.3$ as a solid black line. Understanding the θ dependence of F_{int}/k_BT and F_{ele}/k_BT is a vital component to describing the origins of the extended C_N region. The interfacial energy (F_{int}/k_BT) increases linearly with the θ which reflects the increasing interfacial area separating the nearest PS – PTACCy interfacial connections (Figure 3.1.1 schematic, black dots). The electrostatic energy (F_{ele}/k_BT) on the other hand has a $1/\theta$ dependence indicating that as the interfacial connections separate the effective electrostatic repulsions between polarized ion pairs weaken. Therefore, an increase in interfacial curvature reduces the electrostatic energy yet increases the interfacial energy, and the balancing of these two components drives F/k_BT through a minimum, *i.e.* θ_{min}. When θ_{min} is large then $F_{ele}/k_BT \gg F_{int}/k_BT$ and the interface is force to bend, and when $F_{ele}/k_BT \ll F_{int}/k_BT$ the interface is driven flat.

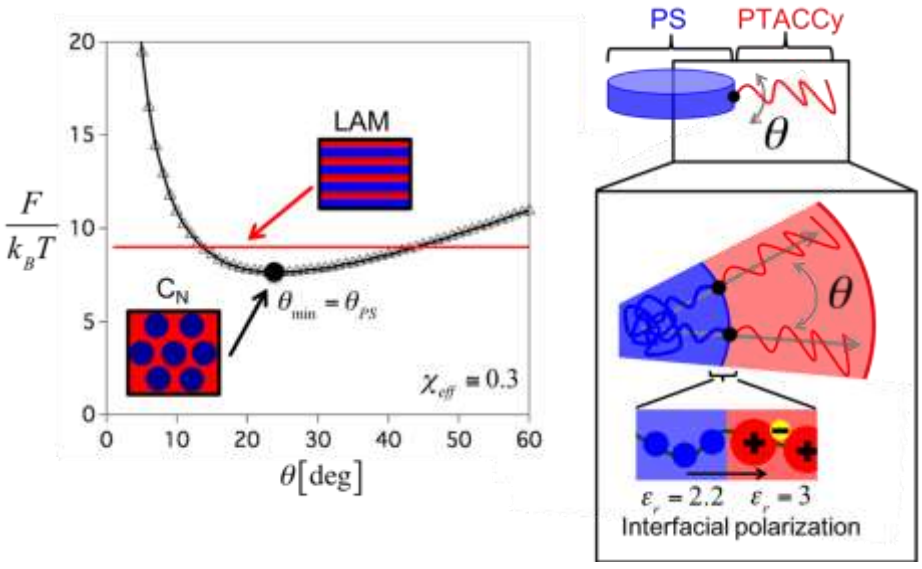

Figure 3.1.1. Stability criterion for the CN morphology. A plot of F/k_BT verses bending angle (θ) for a constant $\varepsilon_r = 3$ and $R_c = 11.4$ nm. The open triangle curve shows the case $\theta_{min} = \theta_{PS}$, where $\chi = 0.3$ was used to meet this requirement. The χ values used to produce the other traces are provided in figure. The solid red line is the corresponding F/k_BT for the lamellar morphology given $R_c = 11.4$ nm, $\varepsilon_r = 3$, and $\chi = 0.3$.

When we set $\theta_{min} = \theta_{PS}$ (Figure 3.1.1A, open triangles) we estimate $\chi \cong 0.3 - 0.4$ for PS-*b*-PTACCy CN-BCPs which is in good agreement with the reported interaction parameters for strongly segregating BCPs and salt doped BCPs.[87–92] Table 3.1.1 reports a list of estimated χ parameters that meet the $\theta_{min} = \theta_{PS}$ requirement for each set of C_N forming PS-*b*-PTACCy CN-BCPs. Interestingly, we find that across all the PS-*b*-PTACCy CN-BCPs the measured effective χ using this method is constant within the error of the analysis. The solid red line (–) in Figure 3.1.1 represents the F/k_BT for the LAM morphology that was determined using geometric analysis and the determined value for χ. For a given R_c, we find the C_N morphology (Figure 3.1.1, open triangles) has a lower F/k_BT than the LAM morphology (Figure 6A, solid red line) at $\theta = \theta_{min}$. This result supports the observed PS-*b*-PTACCy preference for morphologies with convex interfacial curvature and the extended C_N compositional range which is not characteristic of rod-coil BCPs.

3.2 Diagnosis of the shifted C_N-LAM transition: the role of compressibility on PS-b-PTACCy self-assembly

Previously, we discussed a brief theoretical justification for the stability of the C_N morphology. However, it would be naïve to assume this criterion applies for all ϕ_{CN-BCP} since this analysis ignores the PS-b-PTACCy CN-BCPs polymeric aspects. A direct result of the assumptions made in the model is the inability to predict the C_N – LAM transition. Therefore, to formulate the shifted C_N-to-LAM boundary we consider the impact of maintaining the C_N morphology while reducing ϕ_{CN-BCP}. In the context of our synthetic methodology, a constant PS macroinitiator chain length (*i.e.* fixed PS domain radius, R_c), reducing the ϕ_{CN-BCP} translates to lower N_{TACCy}, and thereby a more geometrically frustrated PTACCy matrix. We postulate that the PTACCy matrix chain frustration drives the C_N – LAM order – order transition (OOT), and we quantity the extent of chain frustration using a dimensionless parameter, λ.

$$\lambda = \frac{0.23N_{TACCy}}{l} \tag{3.2.1}$$

For a given ϕ_{CN-BCP}, this parameter compares the maximum distance the PTACCy matrix chain can extend, $0.23N_{TACCy}$, to the distance from the PS domain interface to the interstitial center of the 2D HCP structure (l). Since we the morphology and domain spacing (d) are known we can calculate l for every CN-BCP using the following geometric relationship.

$$l = d\sqrt{3}/3 \tag{3.2.2}$$

Note that Eq (3.2.2) assumes the PS domains order a perfect hexagonal array. Figure 3.2.1 highlights the two important conditions. When $\lambda > 1$, the PTACCy chain is presumably able to fill all regions in the 2D HCP structure, and conversely, if $\lambda < 1$, then PTACCy matrix chains are unable to fill the entire structure and are frustration to maintain a constant density throughout the

C_N morphology. Figure 3.2.1 plots λ as a function of ϕ_{CN-BCP} for all PS-b-PTACCy CN-BCPs studied in Section 2.

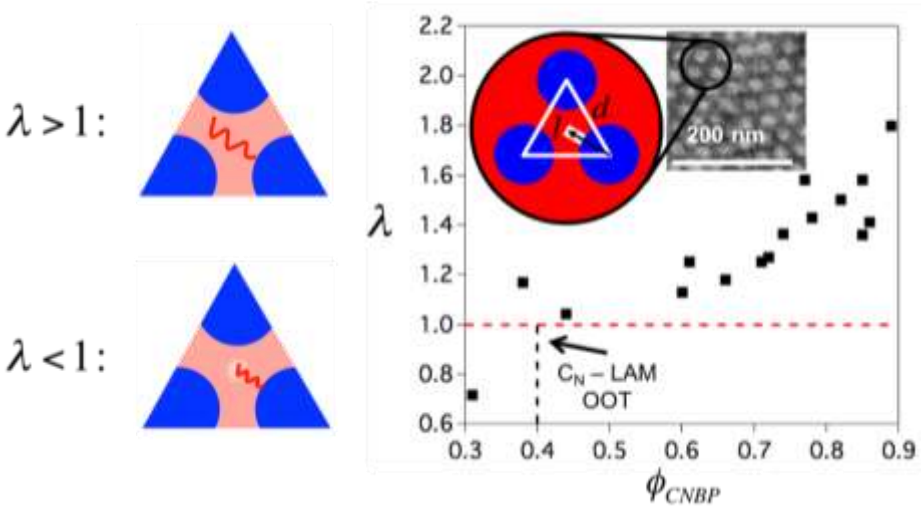

Figure 3.2.1. Geometric frustration in PS-b-PTACCy CN-BCPs. (B) A plot of $\lambda = 0.23N_{TACCy}/l$ against the ϕ_{CNBP}. The dotted red line (---) corresponds to $\lambda = 1$ and the black dotted line (---) is the C_N –to–LAM transition. The inset provides a schematic representation of l highlighted by the white region.

The line at $\lambda = 1$ (horizontal red - - line) is used to indicate the onset of geometric frustration if the 2D HCP morphology is maintained. For reference, we have included the observed C_N-to-LAM transition for PS-*b*-PTACCy CN-BCPs (vertical black - - line). We find λ approaches unity at nearly the same ϕ_{CN-BCP} that we observe the C_N-to-LAM phase transition. Thus, we believe the observed phase transition occurs as a mechanism to alleviate the matrix chain frustration caused by space filling considerations in the C_N morphology.

3.3 A generalized packing parameter approach to connect CN-BCP self-assembly across all electrostatic interaction strength

In this section, we attempt to capture the impact of Coloumbic interactions on CN-BCP self-assembly through a simple, generalized scaling model inspired by Israelachvili's small-molecule surfactant packing parameter.[44] The morphologies of small surfactants containing a

hydrophilic head group and a nonpolar tail can be rationalized by the following packing parameter, P.[93,94]

$$P \equiv \frac{v}{a_0 l_p} \tag{3.3.1}$$

where v and l_p are the volume and the length of the surfactant tail, respectively, and a_0 is the head's cross-sectional area.[93,94] This concept has been extended to BCPs where the characteristic dimension of each polymer block is captured by the corresponding radius of gyration[95] shown in Eq (3.3.2).

$$P_{BCP} = \frac{(R_{g,tail})^2}{(R_{g,head})^2} \tag{3.3.2}$$

Where $R^2_{g,tail}$ and $R^2_{g,head}$ are the cross-sectional areas of the tail and head group, respectively. If we assume both blocks have the same Kuhn length, (*i.e.* $l_{head} = l_{tail}$), then the parameter definition simplifies to the following expression.

$$P_{BCP} = \frac{(1-\phi)}{\phi} \tag{3.3.3}$$

Where ϕ is the volume fraction the polymer block occupying the head group. Thus, we can derive a BCP packing parameter, P_{BCP}, for each BCP phase transition by inserting the ϕ associated with each strong segregation limit (SSL) transition. The SSL transitions between the spherical cluster (S), the cylinder phase (C) and the lamellae phase (L) are $\phi = 0.12\ (S-C), 0.3\ (C-L), 0.7\ (L-C), 0.88(C-S)$, and whe substituted into the Eq (3.3.3) correspond to $P_{BCP} = 22/3\,, 7/3\,, 1, 3/7\,, 3/22$ respectively.[69]

Now that we have established mapping of the packing parameter onto the BCP SSL phase diagram, we can extend this concept to apply or CN-BCPS. We postulate that the influence of ionic integrations rescales the size of the polyelectrolyte block if the Eq (3.3.5) inequality applies. We consider a charge – neutral diblock copolymer, in which A (B) is the neutral (polyelectrolyte)

block with Kuhn length b_A (b_B) and chain length N_A (N_B). To simplify this theory, we consider the case were density of component A is equal to the density of component B, $\rho_A = \rho_B$. Therefore the number fraction of A and B is equal to the volume fraction of A and B and defined as $\phi_A = N_A/N$ and $\phi_B = 1 - \phi_A$, respectively, where N is the total chain length of the copolymer. The Bjerrum length, *i.e.* the length scale over which the Coulombic interaction energy is comparable with the thermal energy ($k_B T$), is l_B.

$$l_B = \frac{e^2}{4\pi\varepsilon_0\varepsilon_r k_B T} \tag{3.3.4}$$

Using this packing parameter model, we divide the CN-BCP morphology diagram into two regions using the following criterion.

$$l_B \geq l_{head}\sqrt{N_{head}} \tag{3.3.5}$$

Using this condition, we calculate a critical CN-BCP total degree of polymerization (N^*) at which this condition is met for each ϕ_{CN-BCP}.

$$N^* = \Lambda^2 \phi_{CN-BCP}^{-1} \tag{3.3.6}$$

N^*, below which the l_B is larger than the characteristic size of the polyelectrolyte block ($l_B \geq l_{head}\sqrt{N_{head}}$) and the P_{CN-BCP} is recalculated to accommodate the ionic interactions by rescaling the effective size of the head group according to l_B. Taking the rescaling into consideration, the CN-BCP packing parameter in this limit can then be written as:

$$P_{CNBP} = \left(\frac{l_{tail}}{l_b}\right)^2 N_{tail} = \frac{N(1-\phi_{CN-BCP})}{\Lambda^2} \tag{3.3.7}$$

Where the dimensionless interaction parameter Λ is equivalent to the Bjerrum length normalized by the neutral block Kuhn length ($\Lambda \equiv l_B/b_A$). The implication of these results enforces that the CN-BCP morphology cannot simple be captured by N and ϕ_{CN-BCP} and must have a third axes,

Λ. This three-dimensional morphology diagram is presenting in Figure 3.3.1A. The blue surface represents the $l_B \geq l_{head}\sqrt{N_{head}}$ boundary dependence on Λ and demonstrates the partitioning of the morphology diagram into two separate regimes. The gray plane, an iso- Λ surface at $\Lambda = 5$, represents a two-dimensional morphology mapping for $\Lambda = 5$, and shown in Figure 3.3.1B. The vertical black line represents the BCP OOTs and their mapped P_{BCP} values provided previously. However, when the P_{BCP}values reach the N^*condition they are recalculated to accommodate the electrostatic interactions and bend significantly to the low ϕ_{CN-BCP} regime in response. The red lines in Figure 3.3.1B represent the recalculated P_{BCP} values (P_{CN-BCP}) for each OOT observed in the BCP phase diagram.

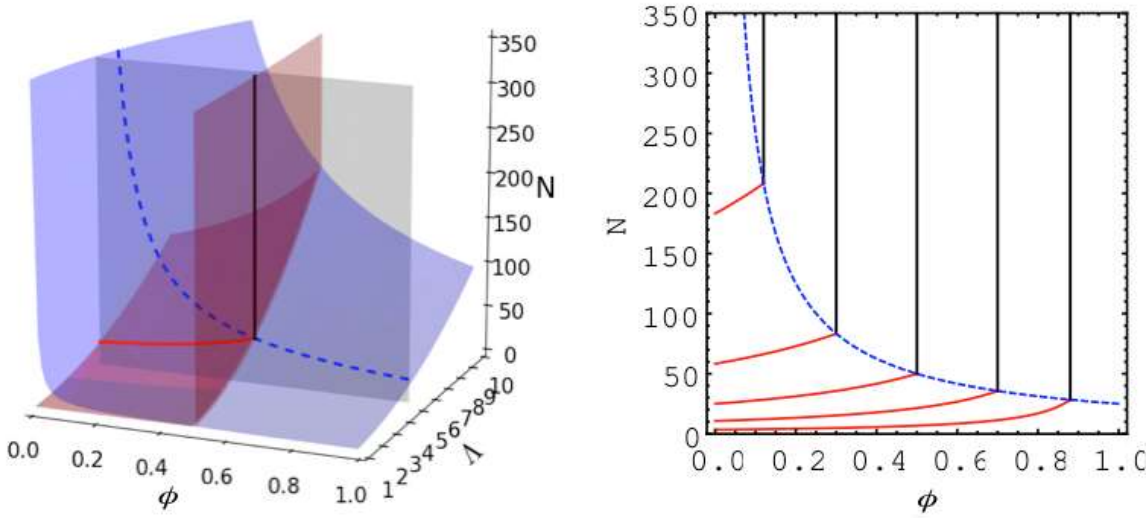

Figure 3.3.1. A three-dimensional representation of the packing parameter model. (A) The three-dimensional surface plot of the critical chain length N^* (ϕ_{CN-BCP}, Λ) (blue). The P = 1 surface (red) is a vertical plane (not a function of ϕ_{CN-BCP}) above N^*. A vertical plane (gray) at Λ = 5 intersects the iso-*P* surface at the phase boundary line (solid). Right: The two-dimensional cut of the three-dimensional surface plot at Λ = 5. Phase boundaries (red solid lines) at P=22/3, 7/3, 1, 3/7, 3/22 are bent below the critical N^* line (blue dashed) but remain unaffected (black solid lines) above N^*.

Therefore, to capture all the features of the three-dimensional morphology mapping we provide the following formalism for the packing parameter to connect across both regimes of the morphology mapping.

$$P \equiv \frac{R_{g,A}^2}{max\{R_{g,B}^2, l_B^2\}} = \frac{N_A b_A^2}{max\{N_B b_B^2, l_B^2\}} = \begin{cases} \frac{1-\phi_{CN-BCP}}{\phi_{CN-BCP}} \left(\frac{b_A}{b_B}\right)^2, & l_B < b_B\sqrt{N_B} \\ N(1-\phi_{CN-BCP}) \left(\frac{b_A}{l_B}\right)^2, & l_B \geq b_B\sqrt{N_B} \end{cases} \quad (3.3.7)$$

Where the end-to-end distance of the two segments $R_{g,A}$ and $R_{g,B}$ are assumed to follow the ideal chain law. If we us the definition of Λ and assign both blocks to have identical Kuhn segments (*i.e.* $\beta \equiv b_A/b_B$) then the calculation of packing parameter can be simplified to the following expressions.

$$P = \begin{cases} (1-\phi_{CN-BCP})\phi_{CN-BCP}^{-1}\beta^2, & N > N^* \\ N(1-\phi_{CN-BCP})\Lambda^{-2}, & N \leq N^* \end{cases} \quad (3.3.8)$$

Alternatively, these equations can be rearranged and solved for the corresponding ϕ_{CN-BCP} and N which allows for the tailored design of any CN-BCP provided there is knowledge of both Λ nd β.

$$\phi_{CN-BCP} = \begin{cases} (1+P_{BCP}\beta^{-2})^{-1}, & \Lambda < \sqrt{N\phi_{CN-BCP}} \\ 1-P_{CN-BCP}N^{-1}\beta^{-2}\Lambda^2, & \Lambda \geq \sqrt{N\phi_{CN-BCP}} \end{cases} \quad (3.3.9)$$

or

$$N = P_{CN-BCP}\Lambda^2\beta^{-2}(1-\phi_{CN-BCP})^{-1}, \quad N \leq N^* \quad (3.3.10)$$

Returning to our experimental data, Figure 3.3.2 shows the packing parameter model predictions for the strong (Figure 3.3.2A) and weak (Figure 3.3.2B) morphology diagrams using $\Lambda = 16$ and $\Lambda = 3$, respectively. Interestingly, the best-fit Λ used for the strong electrolyte morphology diagram corresponds to a lower dielectric medium than what is measured for the pure

polyelectrolyte block. This discrepancy most likely arises from oversimplifications inherent in the scaling model, or perhaps is representative of residual solvent effects on the self-assembly. To this point, while there are a multitude of physical phenomena not represented in the scaling model, this simple rescaling of the molecular geometry appears to capture the PS-b-PTACCy morphology diagram remarkably well. Importantly, the model elucidates the importance that ionic interactions have in creating percolating ion conducting morphologies, even at low ϕ_{CN-BCP} values of the charged block.

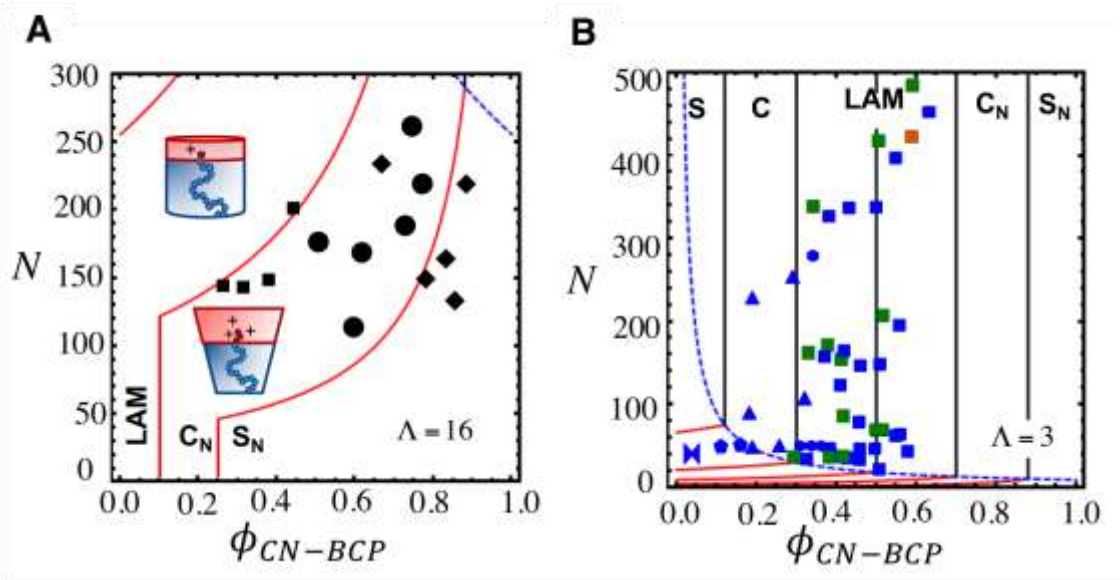

Figure 3.3.2. Packing parameter applied to CN-BCPs. The packing parameter model applied to the (A) strong and (B) weak electrostatic interaction morphology diagrams. In both diagrams, the following symbols are used to define their corresponding CN-BCP morphology; bowtie = disordered, pentagons = S, triangles = C, hexagons = LAM/C, squares = LAM, circles = C_N, diamonds = S_N. The red lines correspond to the theoretical packing parameter predictions that only affect the phase boundaries when the range of electrostatic interactions is larger than electrolyte block (the region below the blue dashed line (---)).

The beauty of this modeling methodology lies in its simplistic nature and minimalist approach. The scaling model requires only a single interaction parameter, $\Lambda = l_b/l_{tail}$. In an ideal case, this fit parameter can be directly calculated from physical characteristics of the CN-BCP and therefore tuned to systematically to adjust the morphology diagram accordingly. The l_b is a

difficult parameter to adjust since it requires a systematic approach to modifying the polyelectrolyte block static dielectric constant, ε_r. However, the tail block Kuhn length, l_{tail}, can be modify through macroinitiator monomeric choice. Thus, this suggests the optimal method to adjusting the CN-BCP morphology diagram is to modify the rigidity of the neutral block for a fixed polyelectrolyte block chemistry. In the literature, many interaction parameters have been presented and the Coulombic cohesion parameter, Γ, bears a striking resemblance to Λ. The only differentiating between two parameters is the normalizing length scale for the Bjerrum length[17]. If Λ is the appropriate quantity to describe such situations, then it would suggest that the chain rigidity of the neutral block captured by l_{tail} can also play a significant role in determining whether or not a given material will exhibit an asymmetric morphology diagram.

Chapter 4: Hydration effects on the permselectivity-conductivity trade-off in polymer electrolytes

Polymer electrolytes, which are commonly used as separator materials in electrochemical devices, have ionic conductivity that is thought to be controlled by segmental mobility. Thus, any improvements made towards increasing ionic mobility comes at the expense of the mechanical integrity. However, selectively solvating the ionic domain, the region responsible for ion conduction, with water or polar organic solvents presents a potential opportunity to circumvent this physical constraint. Here, we explore the role of hydration on the transport properties of membranes formed from randomly sulfonated polystyrene (PS-*r*-sPS). We find the water volume fraction underpins an intrinsic tradeoff between separator permselectivity (Ψ^m) and ion conductivity (κ) – thus, improvements in ion diffusion due to increased water content, comes at the expense of the separator charge density which yields a reduced Ψ^m. We provide a summary of the $\Psi^m - \kappa$ tradeoff for a suite of commercially available separators to elucidate structure – property relationships that can be used for the rational design of advanced separators with improved Ψ^m and κ .

4.1 Material synthesis, methods, and instrumentation

All sulfonated polystyrene separators were prepared from commercially available polystyrene (cat. No. 430102 Sigma Aldrich) and sulfonated using an acetic sulfate procedure modified literature[96]. One gram of polystyrene was dissolved in 20 mL of dry dichloromethane and placed into a three-neck round bottom flask fitted with a condenser and stir bar. In a separate round bottom flask 10 mL of dry dichloromethane was added to 14 mL of acetic anhydride (Sigma) and cooled to 0 ºC. Subsequently, 4.2 mL of 96% sulfuric acid (Sigma) was added to the round bottom flask to generated acetic sulfate. The acetic sulfate solution was then immediately added to the reaction mixture using a glass funnel and the reaction was heated to 45 ºC for reflux. An argon blanket was maintained over the reaction mixture for the entire duration of the experiment. As the reaction progressed the mixture was extracted at various times, immediately quenched in methanol, concentrated *in vacuo*, and the sulfonic acid incorporation (%SL) was determined using ^{1}H NMR in *d-acetone* to monitor the kinetics of the reaction. Once the kinetics of the reaction had been determined, multiple subsequent reactions were performed and quenched at various times to yield randomly sulfonated polystyrene-r-poly(styrene sulfonic acid) (PS-*r*-sPS) copolymers with %SL ranging from $13 - 39\%$. After the PS-*r*-sPS copolymers were quenched they were placed into porous methylcellulose bags for dialysis in water for at least 72 hrs to ensure complete removal of any residual impurities. Then, following the same procedure outline previously, they were concentration *in vacuo*, characterized using ^{1}H NMR in *d-acetone*. The $\%SL$ was determined from the ^{1}H NMR spectra using a procedure described elsewhere[74]. The PS-*r*-sPS separators were prepared by dissolving the purified powder in a 1:1 (v/v) mixture of acetone and methanol and cast into Teflon dishes. The solution was allowed to evaporate for a period of 24 hrs to produce ~ $150\ \mu m$ thick polymer electrolyte separators. The sPS separators were then placed under vacuum

at 100 ºC for 48 hrs to remove any residual solvent and moisture. Prior to electrochemical characterization, the PS-*r*-sPS separators were pretreated using a method modified from a procedure developed for Nafion 117 and outline briefly here[97]. The PS-*r*-sPS separators were first boiled in 1 M H_2SO_4 at 80 ºC for at least 12 hrs then subsequently boiled in 0.1M LiCl at 80 ºC for a period of 3 hrs. After pretreatment, the PS-*r*-sPS separators were stored in 0.1M LiCl and left to equilibrate prior to electrochemical testing.

Table 4.1.1. The Physical Properties of the PS-*r*-sPS polymer electrolytes.

Polymer	SL%[a]	c_f $[\frac{mol}{m^3}]$	IEC $[\frac{mequ}{gm}]$	${\phi_{H_2O}}^b$	${c_{f,swollen}}^c$ $[mol/m^3]$
PS-*r*-sPS13	13	1200	1.1	0.20	970
PS-*r*-sPS21	21	1850	1.7	0.34	1200
PS-*r*-sPS26	26	2220	2.1	0.65	750
PS-*r*-sPS39	39	3100	3.9	0.83	520

[a]All sulfonated materials were characterized using ^{1}H NMR in *d-acetone* to determine the percent monomer functionalization (SL%). [b]The ϕ_{H_2O} was determined from the water uptake assuming volume additivity. [c]The swollen separate charge density ($c_{f,swollen}$) was determined using c_f and accounting for ϕ_{H_2O}.

All PS-*r*-sPS separations were weighed before pretreatment to get the initial dry separator mass (m_{dry}). The dry PS-*r*-sPS separators were then pretreated using the procedure outline previously and the water uptake was determined gravimetrically by quickly removing each sample from solution, drying the sample with an absorbent lab wipe, and weighing the swollen polymer separator to get the swollen separator mass ($m_{swollen}$). The amount of water uptake (m_w) was calculated using Eq (4.2.1)

$$m_w = m_{swollen} - m_{dry} \tag{4.2.1}$$

Using the know densities for each constituent (density of water, dry sPS and dry PS were taken to be $\rho_W = 1.0\ g/cm^3$, $\rho_{sPS} = 1.11\ g/cm^3$, and $\rho_{PS} = 1.03\ g/cm^3$ respectively) the water mass uptake is converted to ϕ_{H_2O} assuming volume additivity[98].

$$\phi_{H_2O}=\frac{m_{W/\rho_W}}{m_{W/\rho_W}+(1-\%SL)m_{dry}/\rho_{PS}+\%SL(m_{sPS}/\rho_{sPS})} \quad (4.2.2)$$

Longer pretreatment times were conducted and no there was no measurable change in the amount of water uptake indicating the samples had reached an equilibrium water content. For confirmation, the ϕ_{H_2O} was measured for each PS-*r*-sPS separator in triplicate to gather an uncertainty in hydration.

To measure the mechanical properties of the PS-*r*-sPS separators we preformed nanoindentation experiments using a *Keysight Nano Indenter G200* in XP mode with a Berkovich indenter tip fabricated by *MicroStar Tech*. Prior to the experiments, the frame stiffness of the system and the area function of the indenter tip were calibrated using a fused silica standard. Samples were loaded onto an aluminum stage using crystalbond adhesive at 120° C. The Keysight built-in standard method entitled *G-Series Basic Hardness, Modulus at a Depth* method was utilized for all measurements such that each indentation test was performed with a single loading/unloading cycle to the user-defined maximum depth of 5 μm. The hardness was determined from the slope of the load-displacement curve during unloading. For each sample, an array of 10 indentations (at minimum) was performed to measure the mean and standard deviation of the hardness at the maximum applied load. Additionally, the fused silica standard was retested periodically before and after sample measurements to ensure accuracy. This procedure was preformed on all dry and swollen PS-*r*-sPS separators to explore the impact of hydration on the separator's mechanical properties.

Following the measurement of the PS-*r*-sPS separators' mechanical properties we set out to measure the ion transport properties of the hydrated separators. In the literature, a lot of emphasis has been placed on determining polymer electrolyte's ionic conductivity (κ), and in the subsequent paragraph we will discuss how κ is measured, however, for solvated separators a complete

understanding of ion transport it is imperative to also quantify the separator ion transference number (t_c^m). Measurement of the t_c^m is done using an ion tracer technique which is discussed in depth elsewhere[99] and outline briefly here. A two syringe *Kent Scientific* syringe pumps controlled volumetric flow rates of electrolyte through the 1 /4″ vinyl tubing at a flow rate of 1mL/min. A Keithley DC supplier was used to apply a constant current between the electrodes ranging from 0–10 mA depending on the sPS separator. The electrode reactions are expected to be hydrogen evolution at the cathode and oxygen evolution at the anode. It should be noted that the measurements are independent of the electrode reaction assumptions, as long Li^+ and K^+ are not produced or consumed at the electrodes under the present aqueous environment. Since the electrodes were positioned in the outlet ports the reaction products flow out of the device and therefore have minimal interference with ion transport across the membrane. For each applied current, 55 mL of electrolyte were used. The device-liquid volume, including tubing, was approximately 5 mL on both the cathode and anode sides. The first 40 mL of sample were discarded, ~ 8 residence times, and the last 15 ml were collected. The initial volume discarded ensures that the experiment is allowed enough time to reach steady state. The concentration of trace Li^+ in the cathode compartment effluent was determined using atomic adsorption spectroscopy (AA). The trace lithium concentrations in the cationic outlet samples were measured with AAS using a Thermo Scientific iCE 3300 spectrometer. Absorbance readings scaled linearly with concentration ($R^2 > 0.99$) over a range of 1–5ppm Li. A 5-point calibration curve was obtained immediately before measuring samples obtained from operating the flow cell. Any samples that were outside the calibration window were diluted to fall within the calibration range.

Finally, to measure the PS-*r*-sPS separator κ an in-house two-compartment Teflon cell was machined to perform potentiostatic electrochemical impedance spectroscopy. Ports in each

compartment were installed to hold platinum electrodes and strategically placed on both sides of a mounted separator and far enough apart such that the potential field lines were constrained by the separator area for transport. Prior to measurement, the cell was then filled with 0.1M LiCl and the background ohmic resistance for aqueous solution was determined. Immediately afterwards, the sPS separator was mounted into the cell and the ohmic resistance was measured. By subtracting the background resistance from the measured separator ohmic resistance yielded the resistance associated with ion transport through the separator.

4.2 Water uptake and mechanical properties.

Polystyrene ($M_w = 190kDa$) purchased from Sigma Aldrich was sulfonated using a procedure outlined previously and used to prepare PS-*r*-sPS of varying %SL characterized by ^{1}H NMR[74]. To avoid miscibility with water which occurs at high %SL we chose to prepare a low to moderate sulfonation range (%SL = 13% – 39%) and the physical properties of all prepared materials are given in Table 4.1.1[74]. The amount of water uptake was determined gravimetrically and quantified using the dimensionless hydration number (λ_w).

$$\lambda_w = \frac{mol_w}{mol_{SO_3}} \tag{4.3.1}$$

The λ_w compares the moles of water inside the separator (mol_w) to the moles of sulfonate groups bound to the polymer separator (mol_{SO_3}). Figure 4.2.1A plots λ_w *vs*. the dry PS-*r*-sPS fixed ion concentration (c_f) which elucidates a nonlinear relationship. The c_f can be converted to the ion exchange capacity (IEC) using the polymer density and the ion exchange capacity (IEC) for all PS-*r*-sPS separators reported in Table 4.1.1. A more convenient way to plot water uptake is to convert λ_w into the separator water volume fraction (ϕ_{H_2O}) which can be achieved using the know densities for each constituent and assuming volume additivity[98]. It is important to note that for polymer electrolytes volumetric additivity has proven to provide a reasonable estimation of

ϕ_{H_2O}[100]. The volume fraction of water for all hydrated sPS membranes is plotted on Figure 4.2.1A (connected red squares). Similar to λ_w, ϕ_{H_2O} increases with increasing c_f, yet, unlike λ_w, we find ϕ_{H_2O} to have a nearly linear dependence on c_f within the experimentally probed %SL range. The nature of this relationship is outside the scope of the work in this chapter and should be the subject of a future investigation. At the highest PS-*r*-sPS c_f, c_f~3100 mol/m^3 (sPS39), the $\phi_{H_2O} =$ 0.83 indicating the separator is predominately water which has a severe impact on the mechanical properties.

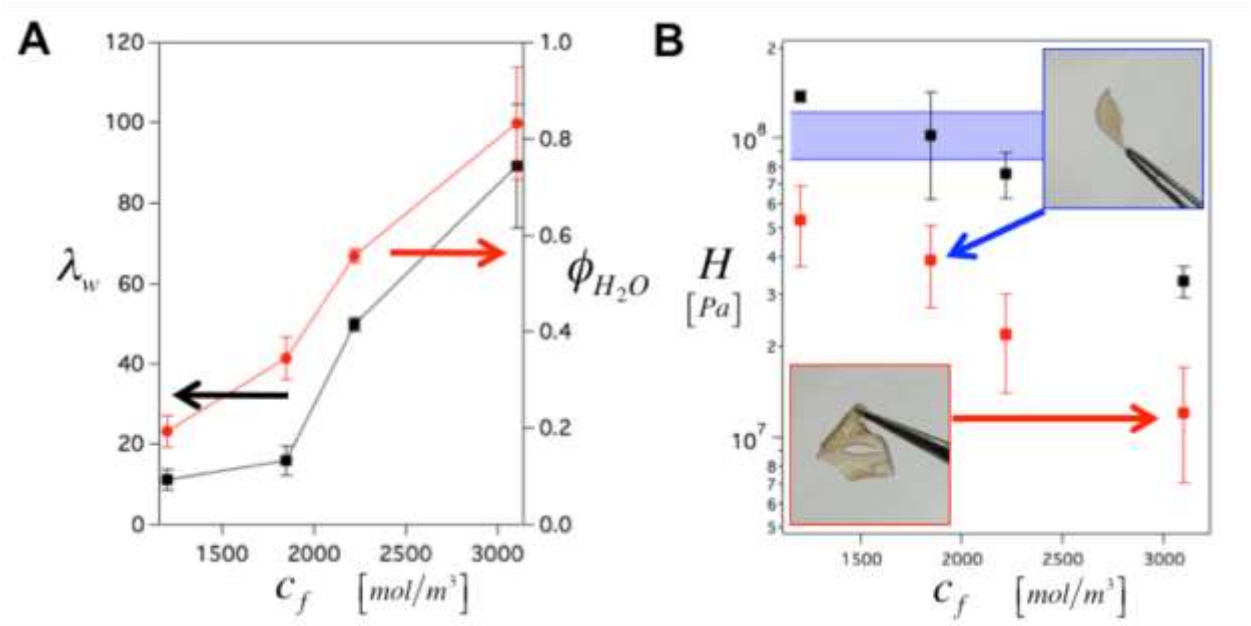

Figure 4.2.1. Swelling and mechanical properties of PS-r-sPS separators. (A) λ_w (black squares) and ϕ_{H_2O} (red squares) were determined and plotted as a function of increasing c_f. (B) The mechanical hardness (*H*) of the swollen (red square) and dry (black squares) PS-*r*-sPS separators are plotted to compare separator mechanical properties before and after pretreatment. The insets are visual aids of the indicated PS-*r*-sPS separators after pretreatment.

To investigate the dry and swollen PS-*r*-sPS separators mechanical properties, nanoindentation, a technique used to probe the hardness of a material (*H*), was employed. Figure 4.2.1B plots the measured *H* dependence on c_f for both the dry (black squares) and hydrated (red squares) PS-*r*-sPS separators. The provided blue region shows the expected *H* range for

polystyrene and is in a quantitative agreement with most PS-*r*-sPS39 separators. The deviation in PS-*r*-sPS39 and slight decreasing trend is presumably due to the inability to completely remove all moisture out of the separator during the drying process. After pretreatment, the *H* decreases by almost an order of magnitude constituting a dramatic change in separator mechanical integrity. All pretreated PS-*r*-sPS separators were mounted at an elevated temperature (120° C) to ensure adhesion to the sample stage. Therefore, the measured *H* for the pretreated separators are likely affected by the mounting procedure. However, the observed qualitative trend with increasing c_f in both the dry and pretreated PS-*r*-sPS separators are still valid and indicative of the impact of ϕ_{H_2O} on separator *H*. Images of PS-*r*-sPS21 and PS-*r*-sPS39 after pretreatment are given as insets in Figure 4.2.1B and used to visually contextualize the dramatic change in mechanical properties with increasing c_f. The PS-*r*-sPS21, $\phi_{H_2O} = 0.34$, is a flexible freestanding film while PS-*r*-sPS39, $\phi_{H_2O} = 0.83$, tears under gravitational force. The impact of hydration of mechanical properties can in some case be beneficial and potentially aid the processing of glassy polymer separators via increased flexibility. However, if hydration compromises the separator mechanical integrity then it could be problematic. For example, during device operation the polymer electrolyte separator experiences a stress due to the fixed charge density suspended within the electric field between electrodes, which, if the polymer modulus is low enough, can cause the separator to tear. [101]

4.3 Characterization PS-*r*-sPS ion transference number

The t_c^m characterizes the amount of current carried by the Li^+ ions, the PS-r-sPS counterion, across the separator in the absence of concentration gradients. The t_c^m can be converted to the separator ionic selectivity, *i.e.* permselectivity (Ψ^m), using Eq 1.2.1. However, using conventional methods for measuring t_c^m (potentiostatic polarization, galvanostatic polarization, electromotive

force methods, NMR, and the Hittorf Method) are not amenable for high throughput characterization and low experimental certainty[102–104]. Recently, Vardner et al. developed a robust ion tracer method that uses an aqueous flow cell to minimize the t_c^m characterization time[99]. Here, the cation tracer method was employed to measure t_c^m for each hydrated PS-r-sPS separator. Each hydrated PS-r-sPS separator was sealed in electroplater's tape with a well-defined exposed cross-sectional area ($A = 0.5\ cm^2$) for ion transport and mounted in the flow cell. For the cation tracer experiments, 0.1M LiCl and 0.1M KCl solutions were loaded into the anodic and cathodic reservoirs respectively and a dual-syringe isocratic microfluidic pump was used to maintain a constant flow rate ($Q = 1mL/min$). A constant current was applied across the cell and samples of the catholyte effluent containing trace amounts of Li^+ ions were collected after 40 minutes of continual operation to ensure a steady-state ion flux was achieved. Atomic absorption spectroscopy (AAS) was employed to determine the Li^+ ion concentration (c_{Li}) and the Li^+ ion flux (N_{Li}) across the membrane was calculated using:

$$N_{Li} = \frac{c_{Li}Q}{A} \tag{4.3.1}$$

Following dilute solution theory, the total Li^+ ion flux across the mounted sPS membranes at the applied current density ($i = i$) can be expressed as:

$$N_{Li} = c_{Li}v - D_{Li}\nabla c_{Li} - Fz_{Li}u_{Li}c_{Li}\nabla\Phi \tag{4.3.2}$$

The bulk fluid velocity across the separator, *v*, is taken to be zero and the Li^+ ion mobility, u_{Li}, follows the Stokes-Einstein relationship:

$$D_{Li} = u_{Li}RT \tag{4.3.3}$$

The applied current density can be related to total ion flow (a sum over all ion species *j*) across the separator using Faraday's constant, *F*.

$$i = F \sum_j z_j N_j \tag{4.3.4}$$

In the limit of high current density, the flux of potassium across the membrane goes to zero, and as a result, the fraction of current carried by the lithium ion becomes approximately equal to t_c^m. The following inequality was used to determine the appropriate current density range necessary to obtain t_c^m for each sPS separator. The application of dilute solution theory to the flow cell characterization of t_c^m is discussed more thoroughly in the literature[99] .

$$\frac{t_c^m i}{FN_{Li,i=0}} > 10\,,\; t_c^m \approx \frac{FN_{Li}}{i} \tag{4.3.5}$$

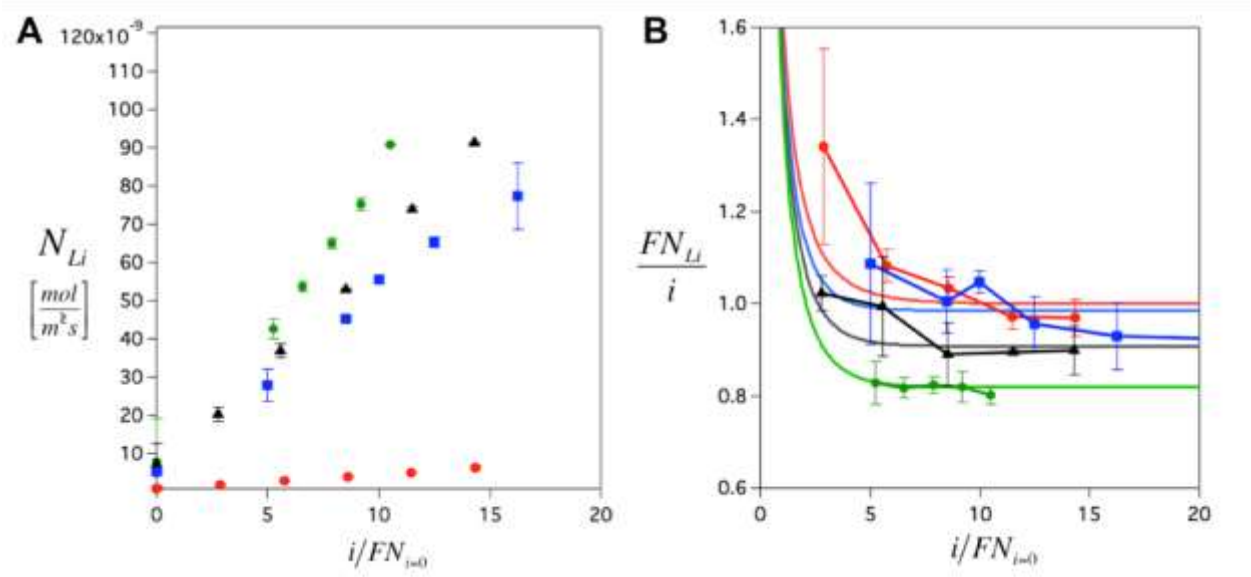

Figure 4.3.1. Electrochemical characterization of t_c^m. (A) The total Li^+ ion flux as function of increasing dimensionless applied current density. (B) Plots the dimensionless Li^+ ion flux dependence on the dimensionless applied current density. The solid lines are numerical dilute solution simulations fit to the experimental data. For both plots the green hexagons = PS-r-sPS39, black triangles = PS-r-sPS26, blue squares = PS-r-sPS21 and red circles = PS-r-sPS13.

Figure 4.3.1A shows the total Li^+ ion flux (N_{Li}) dependence on applied current density normalized by $N_{Li,i=0}$ for all prepared PS-r-sPS membranes. Figure 4.3.1B plots FN_{Li}/i against

the dimensionless current density ($i/FN_{Li,i=0}$). In the limit of high current density, the values of FN_{Li}/i converge to a finite value for all characterized PS-r-sPS membranes. A good estimate of t_c^m can be obtained with Eq (4.3.5), however, numerical simulations were performed to precisely quantify the values of t_c^m considering salt uptake and diffusion through each PS-r-sPS separator[99]. The solid lines on Figure 4.3.1B are the results from the numerical simulation using the best-fit t_c^m values for each separator.

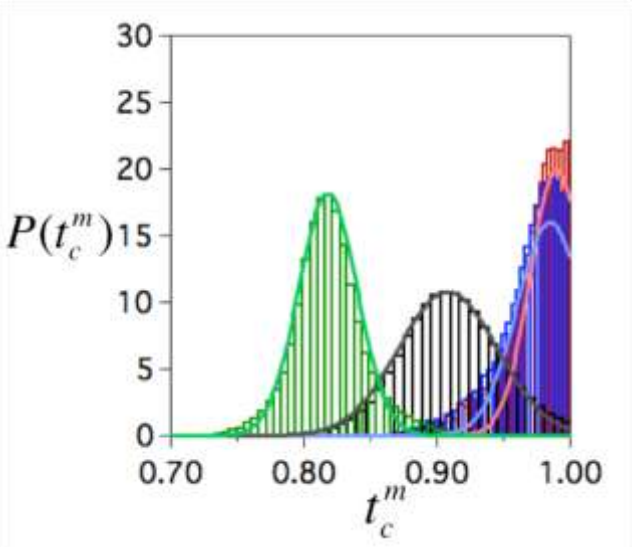

Figure 4.3.2. MCMC simulations of the transference number. MCMC results for the lithium ion tracer experiments. Approximating the probability distribution functions to be gaussian yields $t_c^m = 0.99 \pm 0.03$ for PS-r-sPS13, $t_c^m = 0.98 \pm 0.03$ for PS-r-sPS21, $t_c^m = 0.91 \pm 0.04$ for PS-r-sPS26, and $t_c^m = 0.82 \pm 0.03$ PS-r-sPS39.

Uncertainty analysis in the t_c^m estimates were conducted using a Markov Chain Monte Carlo (MCMC) algorithm, similar to work conducted in the literature[105]. Figure 4.3.2 presents the MCMC results of t_c^m for each separator by comparing the experimental data to the mathematical model. The accepted values of the MCMC algorithm were binned, normalized, and fit to gaussian distributions to estimate the mean and standard deviation of t_c^m for each membrane. The determined t_c^m values for each PS-r-sPS separator are reported in the Figure 4.3.2 caption.

4.4 Trends in the $\Psi_m - \kappa$ tradeoff

The t_c^m is vital component to describing Li^+ transport through the hydrated PS-r-sPS separators but incomplete without a measure of κ or the lithium ion diffusion coefficient (D_{Li}). An in-house conductivity cell was built to perform potentiostatic electrochemical impedance spectroscopy (EIS). From the Nyquist plots, the ohmic resistance (R_Ω) was obtained directly from the high frequency real impedance intercept and then converted into κ using:

$$\kappa = \frac{h_{mem}}{R_\Omega A} \tag{4.5.1}$$

Where h_{mem} and A are the membrane's thickness and exposed area for ion transport respectively. The h_{mem} was determined after pretreatment using a digital vernier caliper. Figure 4.4.1 shows κ and t_c^m as a function of ϕ_{H_2O}. We observe inverse relationship between κ and t_c^m characteristic of swollen polymer electrolyte separators. If c_f is only taken into consideration, then an increasing c_f produces an increase in ion conductivity yet a decrease in t_c^m. However, considering Donnan exclusion, the t_c^m should increase with increasing c_f and become more selective for cationic species as the separator charge density increases[37,45]. If the membrane's swelling is considered, then the trends in both κ and t_c^m can be rationalized.

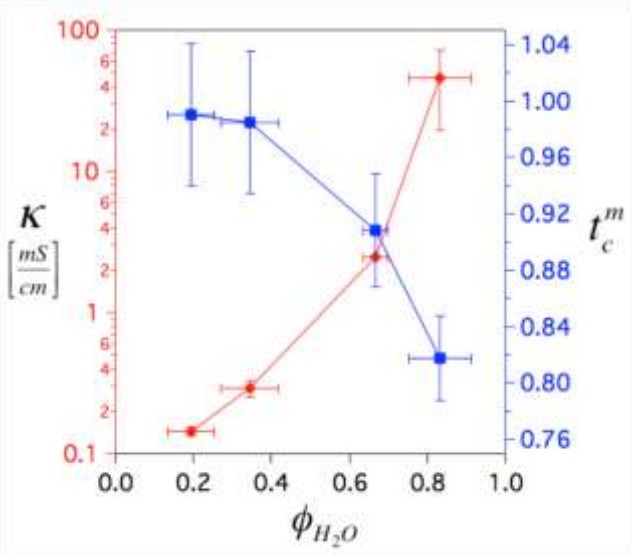

Figure 4.4.1. The tradeoff between selectivity and mobility. The observed inverse relationship between Li ion transference number (blue squares) and ionic conductivity (red diamonds) as the water volume fraction in the sPS separator increases.

The c_f was recalculated to account for ϕ_{H_2O} and labeled $c_{f,swollen} = (1 - \phi_{H_2O})c_f$, the hydrated fixed ion concentration. Figure 4.4.2A plots t_c^m as a function of $c_{f,swollen}$ and we find t_c^m increases with increasing $c_{f,swollen}$. To confirm the validity of our t_c^m measurements we utilized the anion tracer method to repeated the t_c^m measurement on PS-r-sPS21. The red data point is Figure 4.4.2A is the repeated t_c^m measurement and falls within error of the previously determined value. It should be noted that for cation exchange membranes the anion tracer method provides a more certain value of t_c^m. However, due to the low anion (Cl^-) fluxes across the PS-r-sPS separators it was required to go to high applied currents to get accurate determination of Cl^- concentrations using Mohr's method[106]. The PS-r-sPS21 separator was ideally suited for this experiment because the Cl^- concentration was high enough to determine experimentally while maintaining enough mechanical integrity to withstand the strong potential field across the separator. After accounting for ϕ_{H_2O} in the separator charge density an increasing trend in t_c^m with increasing $c_{f,swollen}$ was observed. This treatment of ion transport data was first proposed by Helfferich and then adopted by many other researchers since the delivered message is clear – increasing $c_{f,swollen}$ improves Ψ^m.[37] Interestingly, at a $c_{f,swollen} \sim 1000\, mol/m^3$ we find a transition from single Li^+ conduction ($t_c^m \sim 1$) to mixed ion transference ($t_c^m < 1$). Interestingly, the material with the highest c_f studied (PS-r-sPS39) has the lowest $c_{f,swollen}$ and also the lowest Ψ^m. Additionally, for PS-r-sPS13 and PS-r-sPS21 we find higher t_c^m than most commercial materials including Nafion, yet these separators have a substantially lower κ. Ideally, connecting the separator's chemical structure to its electrochemical performance is desirable. We attempt to

elucidate connections between molecular architecture and separator performance by mapping Ψ^m and κ data for known polymer electrolytes in an effort to inform separator design.

Although t_c^m is the experimentally determined quantity, Ψ^m it is more convenient representation of ion selectivity as it is normalized by t_c^{aqu}. Figure 4.4.2B plots Ψ^m against κ for the PS-r-sPS membranes (black squares) along with a range of different separators found in the literature[37,45,53,107]. The filled symbols are linear randomly functionalized homopolymer of varying bound ion identity and backbone compositions (the chemical structures provided in Figure 4.4.2C). The open symbols represent a summary of materials with different separator architectures (*i.e* chemically cross-linked networks [blue open diamonds] or phase separated blends [green open squares]). Additionally, a host of commercially available separators (black open circles)[107] including Selemion[107] (purple filled hexagon) and Nafion (pink filled pentagon, considering Li^+ conductivity) are provided for reference of the state-of-the-art separator performance. Taking a step back, comparing across all linear randomly functionalized homopolymers we find a intriguing relationship between backbone rigidity and the $\Psi^m - \kappa$ tradeoff. Polymer electrolyte separators derived from high glass transition temperature polymers such as poly(phenylsulfone) (green triangles) and poly(2,6-dimethyl-1,4-phenylene oxide) (red circles and orange squares)[37] ($T_g =$ 220 °C and $T_g =$190 °C respectively) display a minor tradeoff between $\Psi^m - \kappa$ over a wide parameter space ($0.01 < \kappa < 10\ mS/cm$ and $0.85 < \Psi^m < 0.95$) which is highlighted by the (--) line . Interestingly, when $\kappa \to 0$ this class of polymer electrolyte separators do not recover single ion-conducting behavior ($\Psi^m = 1$). Perhaps this is related to an intrinsic free volume within the material driven by frustrated molecular packing. Indeed, as mentioned previously, increasing molecular rigidity has proven effective parameter to manipulate gas permeability and attributed to an increase in free volume for penetrants[38,41,108,109]. Polystyrene on the other hand has a much lower

glass transition temperature (T_g ~105 °C) and shows a very different $\Psi^m - \kappa$ tradeoff demonstrated by the black (- -) line. In contrast, when $\kappa \to 0$ the PS-r-sPS separators recover $\Psi^m = 1$ behavior yet lose Ψ^m quickly as κ increases. When compared across a similar range in κ to the high T_g backbone materials, the PS-r-sPS separators have a more dramatic $\Psi^m - \kappa$ tradeoff ($0.7 < \Psi^m < 1$). Note that the lines (- - and - -) in Figure 4.4.2B are included to elucidate the trends in the experimental data and are empirical relationships that currently have no theoretical foundation.

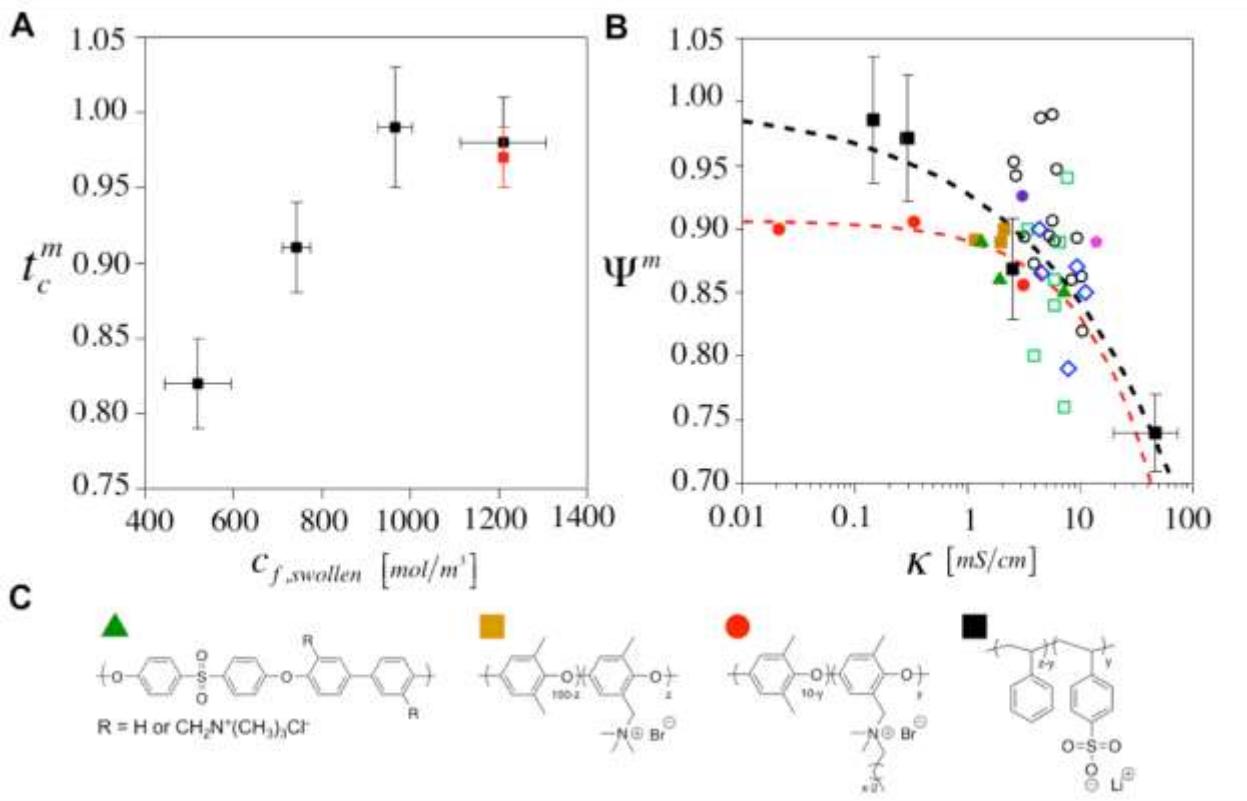

Figure 4.4.2. The $\Psi^m - \kappa$ tradeoff in swollen polymer electrolytes. (A) The Li^+ ion transference number (t_c^m) plotted as a function of $c_{f,swollen}$. (B) The tradeoff between permselectivity (Ψ^m) and κ for sPS separators (black squares) and a variety of separators found in the literature. Notes that a reported value of $t_c^{aqu} = 0.31$ for 0.1M LiCl aqueous solution was used to calculate Ψ^m for the sPS separators[110]. (C) The chemical structures of some of the polymer electrolyte separators provided in (5B) where the corresponding symbols are located directly above the structure.

Additionally, the $\Psi^m - \kappa$ tradeoff can be influenced by separator physical architecture. As mention previously, Guler et al. prepared anion exchange membranes by cross-linking polyepichlorohyrin (PECH) elastomers with 1,4-diazabicyclo[2.2.2]octane where each crosslink two quarternized ammonium moieties. To manipulate the ion exchange capacity, the authors blended the PECH with polyacrlyonitrile, an inert mechanically reinforcing polymer, at different ratios (green open squares) prior to crosslinking[53]. They found that increasing the inert polymer content produced substantial improvements to Ψ^m with only minor decreases in κ. Additionally, Chakrabarty et al. prepared anion exchange separators by cross linking poly(vinyl alcohol) with 2-(dimethylamino)ethylmethacrylate containing trimethoxysilane end groups where the cation moiety is created by methylating the amino motif[45]. In this study, increasing the c_f by almost 50% produced separators with improved Ψ^m with only a minor decrease in κ. Both studies demonstrate the Ψ^m sensitivity to separator physical architecture suggesting that perhaps the presence of non-conducting phases and cross-linking agents can produce a horizontal navigation of the $\Psi^m - \kappa$ diagram.

While the complied $\Psi^m - \kappa$ diagram does elucidate intriguing structure – property relationship for hydrated polymer electrolytes it is also immediately apparent from Figure 4..4.2B that practically all commercially available separators have $\Psi^m < 1$ regardless of κ. Aqueous energy storage applications such as vanadium flow batteries minimizing ionic crossover arising from $\Psi^m < 1$ is imperative to improve the implementation of the technology. Therefore, it is necessary to develop a more advanced fundamental understanding of how Ψ^m and κ connects to the separator's chemical structure.

4.5 Lithium ion diffusion in PS-r-sPS separators

The κ can be calculated for any ionically conductive medium by accounting for the sum of all diffusing ions using Eq (4.6.1).

$$\kappa = \frac{F^2}{RT}\sum_j z_j^2 D_j c_j \tag{4.6.1}$$

Invoking ohm's law and using the measured t_c^m for each sPS separator we can convert the measurements of κ into the Li^+ diffusion coefficient ($D_{Li,}$) by applying Eq (4.6.2).

$$D_{Li} \approx \frac{\kappa RT t_c^m}{F^2 z_{Li}^2 c_{f,swollen}} \tag{4.6.2}$$

The extraction of D_{Li} from κ using the experimentally determined t_c^m is under the assumption that the Li^+ concentration in the membrane is equal to the fixed concentration $c_{f,swollen}$ and the consequences of this assumptions will be discussed subsequently. Additionally, another independent measure of D_{Li} can be obtained from the cation tracer $N_{Li,i=0}$ by applying dilute solution theory, shown in Eq (4.6.3).

$$D_{Li} = \alpha(t_c^m, D_K, D_{Cl}, \frac{S_K}{S_{Li}}) \frac{N_{Li,i=0} h_{mem}}{c_{f,swollen}} \tag{4.5.3}$$

Dilute solution theory shows that the value of D_{Li} is proportional to the diffusive flux of Li^+ across the separator by a coefficient α, which depends on the salt uptake (S_K/S_{Li}) and transport through (t_c^m, D_{Cl}, D_K) the membrane. The α coefficients were simulated for each PS-r-sPS separators by fixing the t_c^m values and varying the other physical parameters. A list of α coefficients for all PS-r-sPS separators is available in Table 4.5.1. For all PS-r-sPS separators where $t_c^m < 1$ we find $\alpha > 1$ indicating that Fick's Law ($\alpha = 1$) would not yield a reliable estimate of D_{Li} due to the charge associated with the lithium species. The MCMC was used to estimate the uncertainty in D_{Li} accounting for experimental error in $N_{Li,i=0}$.

Table 4.5.1. Simulated α coefficients for all PS-r-sPS separators.

Polymer	α[a]
PS-r-sPS13	1.0
PS-r-sPS21	1.0
PS-r-sPS26	1.1
PS-r-sPS39	1.3

[a]All α coefficients were determined using dilute solution theory with knowledge of $N_{Li,i=0}$ and t_c^m for each separator.

Figure 4.5.1 plots the D_{Li} determined from Eq (4.5.2) (connected red squares) and Eq (4.5.3) (connected blue squares) as a function of increasing ϕ_{H_2O}. The two estimates of D_{Li} agree quantitatively except for PS-r-sPS39 where the entire separator volume is dominated by water $\phi_{H_2O} > 0.5$. The departure between the two D_{Li} estimates for this membrane is thought to be due to the breakdown of the assumption that $c_{Li} = c_{f,swollen}$ in Eq (4.5.1). Eq (4.5.1) assumes the Li^+ concentration in the membrane is equal to $c_{f,swollen}$ and that all the Li^+ within the separator exhibit the same D_{Li}. When $t_c^m \sim 1$ we observe good agreement between the simulated D_{Li} and the value determined from κ. However, when $t_c^m < 1$ the concentration of Li^+ in the separator may be higher than $c_{f,swollen}$ leading to an overestimation of D_{Li}. Figure 4.5.2 plots the steady state zero current Li ion flux ($N_{Li,i=0}$) as a function of increasing c_f. Higher c_f translates to increased $N_{Li,i=0}$ and attributed to the increased free volume available for ion diffusion.

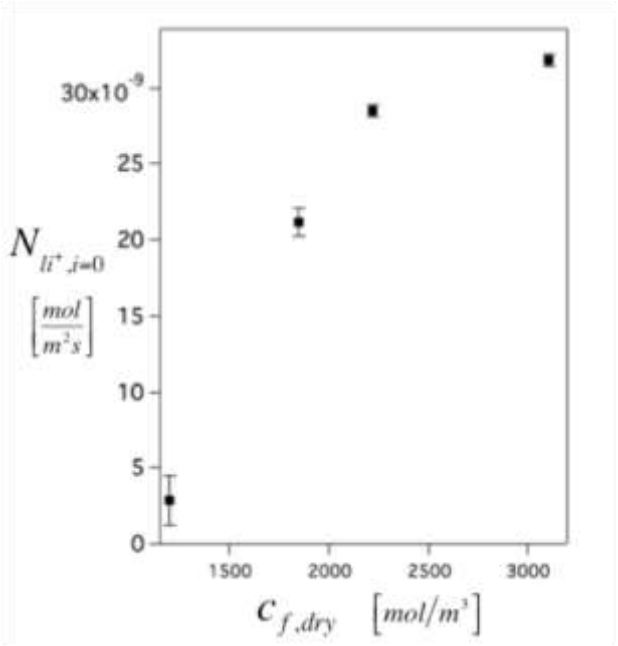

Figure 4.5.2. A plot showing the $N_{Li,i=0}$ dependence on the dry PS-r-sPS fixed charge density, c_f.

Additionally, many researchers studying swollen polymer electrolytes using pulse field gradient Li^+ NMR have reported observing multiple different D_{Li} corresponding to Li^+ having different local chemical environments[111,112]. It is quite possible that modeling the κ of hydrated polymer electrolyte separators with a single diffusing Li^+ species may be inadequate when ϕ_{H_2O} is large. Future work will be to dedicated towards determining Li^+ and Cl^- ion uptake to more precisely evaluate how D_{Li} and D_{Cl} are affected by ϕ_{H_2O} and hydrated separator charge density.

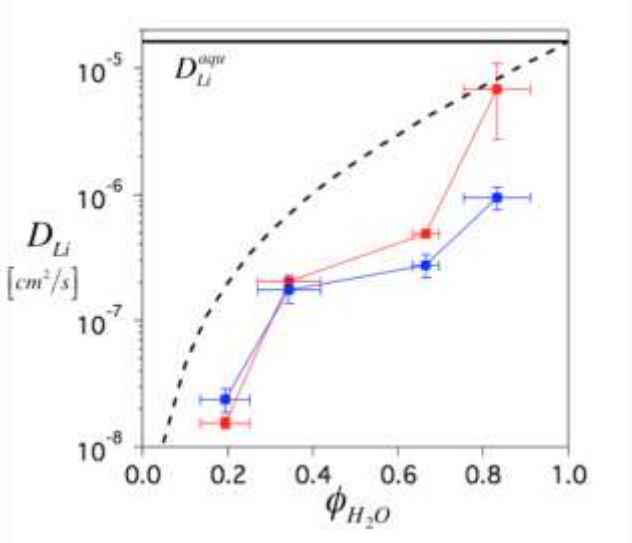

Figure 4.5.1. The role of hydration on the Lithium ion diffusion coefficient. The Li^+ diffusion coefficient dependence on ϕ_{H_2O} calculated from κ data (connect red squares) and $N_{Li,i=0}$ data(connect blue squares).

Mackie and Meares produced a model to predict D_{Li} in swollen polymer electrolyte membrane given below[113].

$$D_{Li} = \left(\frac{\phi_{H_2O}}{2-\phi_{H_2O}}\right) D_{Li}^{aqu} \tag{4.5.4}$$

The statistical model assumes the polymer chains are distributed randomly on a cubic lattice and D_{Li} can be calculated using the aqueous lithium diffusion coefficient D_{Li}^{aqu} and a tortuosity factor that depends only on ϕ_{H_2O}. Since the polymer's segmental diffusion coefficient is much smaller than D_{Li} the chains are assumed to be immobile and not contributing to D_{Li}. The Mackie and Meares prediction is plotted on Figure 4.5.1 (- -) and shows agreement with D_{Li} at $\phi_{H_2O} = 0.83$. This type of agreement has been observed in the literature for highly swollen separators[114]. Interestingly, across all the other experimentally measured PS-r-sPS membranes we observe a D_{Li} lower than what is predicted by the Mackie and Meares model. This result suggests that an additional factor other than separator tortuosity is contributing to a reduction in D_{Li}. Indeed, measurements of salt sorption in sulfonated polymer electrolytes suggest that separators with lower

ϕ_{H_2O} are influenced by Donnan exclusion to a greater extent[58]. Additionally, increasing the salt content in the external solution increased coion sorption into the sulfonated polymer separator, which might be expected from screened ionic interactions. In this vein, perhaps an ionic consideration might be necessary to explain the observed suppression in D_{Li} with respect to the tortuosity prediction by Mackie and Meares, but at this time, the underlying mechanism for these results is unclear.

Chapter 5: Two-dimensional self-assembly of PS-b-PTACCy CN-BCPs.

Block copolymer thin films have traditionally been of interest for lithograph, optics, coatings, and membrane technologies, however, incorporating ionic functionality into the thin matrix opens the door to emerging energy storage applications. In this chapter we explore trisaminocyclopropeniumdicyclohexyl (TACCy) containing charge neutral block copolymers (CN-BCPs) as a model system for structuring ionic thin films. Due to the strong ionic interactions present in PS-*b*-PTACCy thin films, arising from the low PTACCy static dielectric constant ($\varepsilon_r = 2.5 - 3$), solvent vapor annealing was utilized to facilitate the self-assembly. We combined grazing incidence small angle x-ray scattering with atomic force microscopy to probe the thin-film CN-BCP self-assembly and the results are compared to the bulk PS-b-PTACCy morphology diagram. Additionally, we explore the annealed PS-*b*-PTACCy thin-film morphology film thickness dependence and propose a role of confinement on the self-assembly. Finally, we demonstrate control over the domain orientation and if the annealing conditions are picked appropriately both orientations can be accessed reversibly.

5.1 Materials, experimental methods, and instrumentation

Before moving on to the experimental part of this section, we will first briefly discuss the synthesis of the studied PS-b-PTACCy CN-BCPs. All materials were purchased from Sigma-Aldrich and were used without further purification. Styrene was polymerized using a previously reported procedure.[21] Copper (I) bromide and tris(2-pyridylmethyl)amine were added to a dry Schlenk flask and the material was deoxygenated via five vacuum-argon cycles. Degassed styrene was added to the flask and allowed to stir for 10 minutes under argon until the solution turned light green, indicating that the Cu complex formed. The Schlenk flask was closed under argon and degassed ethyl α-bromoisobutyrate was injected. The reaction mixture was heated to 90 °C and allowed to react overnight. The polymer was dissolved in tetrahydrofuran (THF), filtered through an alumina column, precipitated twice into a stirred solution of cold methanol, and vacuum dried overnight. The molecular weights and Đ of the final material were determined using GPC in THF calibrated with polystyrene standards.

After isolation, the polystyrene macroinitiator was used in a subsequent chain extension polymerization and carried out as follows. Copper (I) bromide and tris(2-pyridylmethyl)amine were added to a dry Schlenk flask and the material was deoxygenated via five vacuum-argon cycles. Degassed tert-butyl methyl(4-vinylbenzyl)carbamate was added to the flask and allowed to stir for 10 minutes under argon until the solution turned light green, indicating the Cu complex formed. The mixture was subjected to three freeze-pump-thaw cycles to ensure all oxygen was removed from the reaction vial. The Schlenk flask was closed under argon and degassed polystyrene macroinitiator anisole solution was injected, the reaction mixture was heated to 90 °C and allowed to react overnight. Aliquots were taken at different times and examined by ^{1}H NMR to determine conversion. The polymer was dissolved in THF, filtered through an alumina column,

precipitated three times into a stirred cold methanol/water solution, and vacuum dried overnight. The molecular weights and Đ of the final material was determined using GPC in THF using polystyrene standards. The poly(tert-butyl methyl(4-vinylbenzyl)carbamate) block (PBoc) degree of polymerization was determined using ^{1}H NMR.

The PS-*b*-PBoc was then prepared for functionalization via deprotection of the tert-butyl carbamate group. The PS-*b*-PBoc was dissolved in a 50/50 DCM: MeOH solution (15 mL) in a round bottom flask under argon. The flask was cooled to 0˚C and trimethylsilyl chloride was added. The reaction was allowed to stir at room temperature overnight and then concentrated under vacuum to yield a white powder. The powder was then re-dissolved in DMSO and 1 M NaOH was added dropwise, with stirring, until the polymer precipitated from solution. The resulting slurry was centrifuged, and the supernatant decanted. The deprotected polystyrene-b-poly(4-methylaminostyrene) (PS-*b*-PMAS) polymer was washed twice with DI water, and collected via centrifugation, and dried under vacuum. PS-*b*-PMAS was dissolved in chloroform in a scintillation vial. In parallel, *N,N*-diispropylethylamine was added to the another scintillation vial, followed by a solution of TACCy in 4 mL of Chloroform. The two solutions were combined and the reaction mixture was heated to 65 °C and allowed to react overnight. The resulting solution was concentrated *in vacuo*, dissolved in methanol, transferred into a 3.5 kDa MWCO Spectrum Labs dialysis bag, and allowed to dialyze in a methanol bath for three days. The bath was replaced with fresh methanol twice per day. The resulting colloidal solution was concentrated under vacuum to yield a light amber powder, a purified PS-*b*-PTACCy linear diblock copolymer. The ^{1}H NMR chemical shifts and integrations have been reported for this material in a previous.[21,22]

Table 5.1.1. A summary of PS-b-PTACCy CN-BCPs for thin-film morphology mapping.

Polymer Name	PS M_n (kg/mol)	Charge Fraction ($\phi_{CN\text{-}BCP}$)	Degree of Polymerization (N)	Dispersity (Đ)
PS_{175}-*b*-$PTAC_{25}$	18	0.44	200	1.08
PS_{175}-*b*-$PTAC_{60}$	18	0.66	235	1.14
PS_{175}-*b*-$PTAC_{90}$	18	0.74	265	1.2
PS_{130}-*b*-$PTAC_{10}$	14	0.31	140	1.07
PS_{130}-*b*-$PTAC_{20}$	14	0.38	150	1.07
PS_{130}-*b*-$PTAC_{40}$	14	0.61	170	1.07
PS_{130}-*b*-$PTAC_{60}$	14	0.72	190	1.18
PS_{130}-*b*-$PTAC_{90}$	14	0.78	220	1.08
PS_{90}-*b*-$PTAC_{25}$	9.5	0.61	120	1.04
PS_{90}-*b*-$PTAC_{40}$	9.5	0.71	130	1.06
PS_{90}-*b*-$PTAC_{60}$	9.5	0.78	150	1.07
PS_{90}-*b*-$PTAC_{75}$	9.5	0.82	165	1.09
PS_{90}-*b*-$PTAC_{90}$	9.5	0.85	180	1.09
PS_{90}-*b*-$PTAC_{130}$	9.5	0.89	220	1.11
PS_{60}-*b*-$PTAC_{60}$	6.5	0.85	120	1.08
PS_{60}-*b*-$PTAC_{65}$	6.5	0.86	125	1.07

Table 5.1.1 lists all the PS-b-PTACCy CN-BCPs used in this study. The PS-*b*-PTACCy CN-BCP charge volume fraction (ϕ_{CN-BCP}) was obtained using ^{1}H NMR, the bulk density of PS (ρ_{PS}= 1.04 g/cm^3), the bulk density of PTACCy (ρ_{PTACCy}= 1.07 g/cm^3, determined via helium pycnometry), and assuming no volume change upon mixing. The second measure of the PS-*b*-PTACCy CN-BCP charge volume fraction was calculated using a combination of TEM image analysis and small angle x-ray scattering to obtain the size of the PS domain and CN-BCP lattice constant respectively. Any spaces that have a (--) correspond to materials that were unable to be imaged via TEM. The total degree of polymerization (N) was calculated using a combination of GPC and ^{1}H NMR. Specifically, GPC was used to obtain the number of styrene monomers in the PS macroinitiator and ^{1}H NMR to determine the number of PTACCy monomers relative to the PS

monomers in the macroinitiator. The dispersity was measured using gel permeation chromatography calibrated to polystyrene standards using THF as the mobile phase

The prepared PS-b-PTACCy CN-BCPs were dissolved in methylethylketone (MEK) to form a 10 mg/mL solution and stirred overnight. Silicon (Si) wafers were diced using a diamond score and solvent washed with DI H_2O, acetone, methanol, and isopropanol sequentially (for each solvent washing, the wafers were sonicated for 30 min), and then dried using a N_2 in preparation for coating. The homogenous PS-b-PTACCy solution was filtered through a 0.2 μm PTFE filter to remove any large impurities and spun coated onto the cleaned Si wafers. The coated film thickness was varied by adjusting the number of revolutions per minute (from 500-3000 rpm) during spin coating. Each PS-b-PTACCy CN-BCP film was dried under vacuum at room temperature for a period of 24 h to remove all residual casting solvent before solvent vapor annealing. The solvent vapor annealing process is discussed subsequently and modified from a set-up that can be found elsewhere[115].

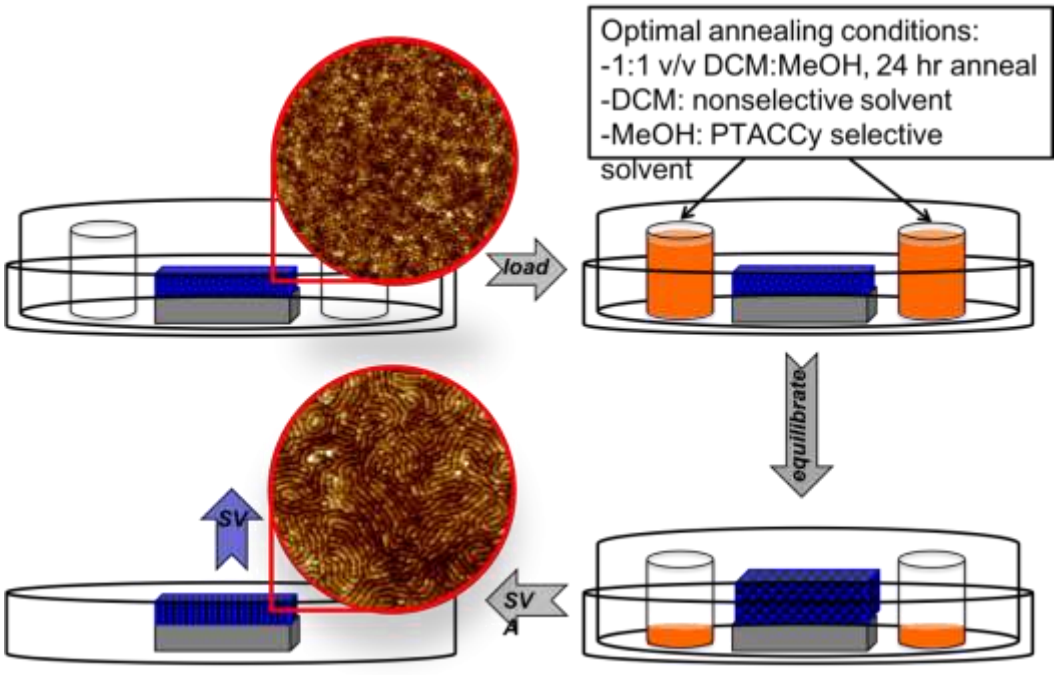

Figure 5.1.1. A schematic representation of the bell jar solvent vapor annealing process. It is broken down into 4 separate steps, (1) spin coating a thin-film, (2) loading the bell

jar with the solvents chosen for vapor annealing, (3) letting the film swell and equilibrate, and finally (4) removal of the lid to start solvent evaporation. AFM topography images of the *as cast* and vapor annealing PS-*b*-PTACCy film surfaces are provided.

The dried *as-cast* CN-BCP films were solvent vapor annealed using the stepwise procedure provided in Figure 5.1.1. First the films are placed in a glass petri dish along 10 mL beakers filled with the desired solvents for annealing. Many solvents were screened to vapor anneal the PS-*b*-PTACCy films, and the optimal solvent systems was found to be 20 mL dichloromethane / 20 mL methanol (two 10 mL beakers of each solvent). Next, the samples and solvent beakers were covered with a glass crystallization dish, fortified with weights, and allowed to vapor anneal for a 24 hr period. The glass chamber was then removed to commence the solvent evaporation and the self-assembly of the PS-*b*-PTACCy film. The films were left on the benchtop for ~ 1hr to condense and then placed in under vacuum overnight. The schematic representation of the chamber is found elsewhere[115]. The dried vapor annealed PS-b-PTACCy films were characterized using atomic force microscopy (AFM), grazing incidence small angle x-ray scattering (GISAXS) and ellipsometry to determine the surface morphology, film morphology, and film thickness respectively. The methodology for each technique will be described subsequently.

AFM was performed on a Bruker Dimension Icon peak force quantitative nanomechanical-mapping mode to determine the sample surface morphology. We used a scan asyst silicon tip on a nitride lever with a spring constant of 0.4 N/m and resonant frequency of 70 kHz. The feedback gain was varied to minimize the peak force error and a 0.1 Hz scan rate was used for each image. Next, GISAXS was performed at the Advance Light Source Lawrence Berkeley National lab on the 7.3.3 beam line with a constant X-ray energy of 10 keV. The sample to detector distance was calibrated using a silver behenate standard. The incidence angle between the incident beam and sample surface was fixed at 0.14°. The scattering profiles were recorded using a Pilatus 1M 2-D

area detector. Finally, the CNBP film thicknesses were determined using a J.A. Woollam Co., Inc Ellipsometer. The instrument was calibrated to silicon oxide with a 23nm oxide layer. The Cauchy model was used to model a transparent film on top of the silicon substrate.

5.2 Determination of PS-*b*-PTACCy film composition

Transmission electron microscopy (TEM) and atomic force microscopy (AFM) are methods of imaging the bulk and surface morphology of polymer films respectively. An advantage of TEM is that this techniques maps the electron density contrast between components throughout the sample which can provide information related to the film composition. AFM, on the other hand, AFM uses a cantilever to measure to determine a film's surface topography which is indirectly relatable to the sample surface composition if the proper mode is applied. However, to accurately decode the PS-*b*-PTACCy surface morphology we devised tailored selective swelling surface reconstruction experiment to selectively infiltrate solely the PS block. [116] Using the this technique and a AFM we can decouple the components present at the film surface.

Figure 5.3.1 provides a schematic representation of the selective swelling surface reconstruction. On the top, we provide an example of the AFM topography image obtained after solvent vapor annealing a $h = 40\text{nm}$ PS-*b*-PTACCy ($N = 220, \phi_{CN-BCP} = 0.78$) thin-film. The surface shows a hexagonal array of circular surface domains that protrude 1-2 nm out of the film surface. The Fourier transform of the film surface was done using imageJ software and provided next to the AFM topography image. The transformed image displays a set of 6 scattering spots and consistent with the 2D hexagonal structure factor. In chapter 2, we found the PS block dominantly assumes the discrete phase of the PS-*b*-PTACCy bulk morphologies and we postulated the consideration applies here. Therefore, to reconstruct the PS-*b*-PTACCy film surface we sought to selectively swell the PS domains using cyclohexane – a selective solvent for PS. We completely

submerged the PS-*b*-PTACCy thin film in a 50 mL beaker filled with cyclohexane. Due to the selective nature of the solvent it infiltrates the PS domains causing the chains to expand out of the film since the matrix is fixed. Therefore, if the cyclohexane is rapidly removed before the chains have enough time to relax back into the domain, then the PS chains are arrested on the film surface leaving a pore in the center of the PS domain following the schematic in Figure 5.3.1.

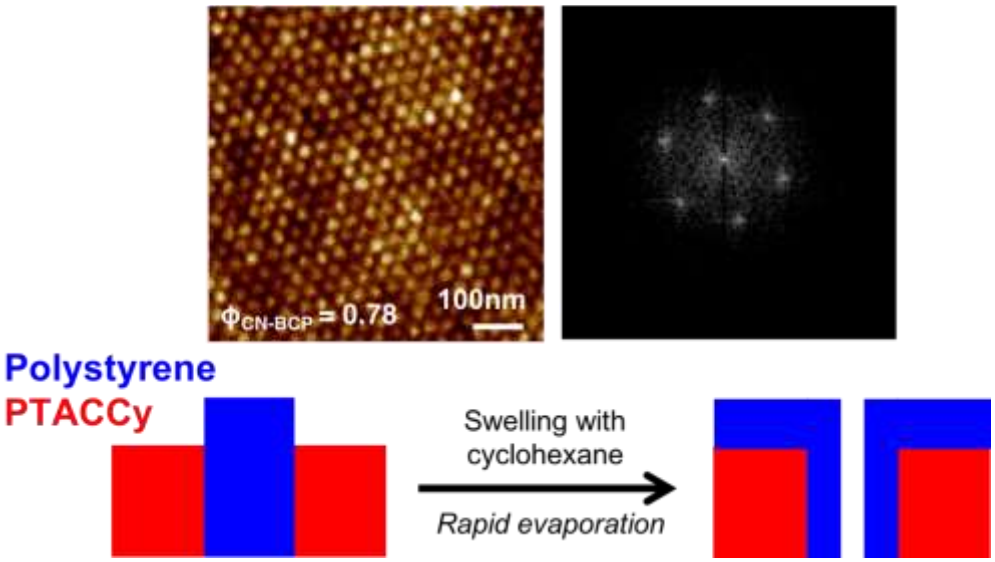

Figure 5.1.1. Schematic representation of the solvent reconstruction process. Here, we are showing the PS domains (blue) reconstructed with a selective solvent (cyclohexane). The provided AFM topography image and FFT image of the film surface (top) show the sample the underwent the surface reconstruction experiment.

The results of the selective swelling surface reconstruction are provided in Figure 5.3.2. Figure 5.3.2A is an AFM topography image taken after solvent vapor annealing and the average domain spacing (d) and cylinder radius (R_c) were determined to be 36 ± 4 nm and 11.5 ± 2 nm using image analysis. The inset is a Fourier transform of the film surface highlighting the domain hexagonal symmetry. This film was subjected the selective swelling surface reconstruction experiment in cyclohexane. Figure 5.3.2B is an AFM topography image of the same film taken after the surface reconstruction. Immediately, a qualitative confirmation of a successful surface reconstruction is provided by the appearance of pin holes in the center of each domain. We find

that the reconstructed film $d = 36 \pm 4$ nm, $R_c = 13.5 \pm 2$nm, and the average pore radius (R_p) is $R_p = 3 \pm 0.75$ nm and undoubtable confirming the domains are indeed the PS block.

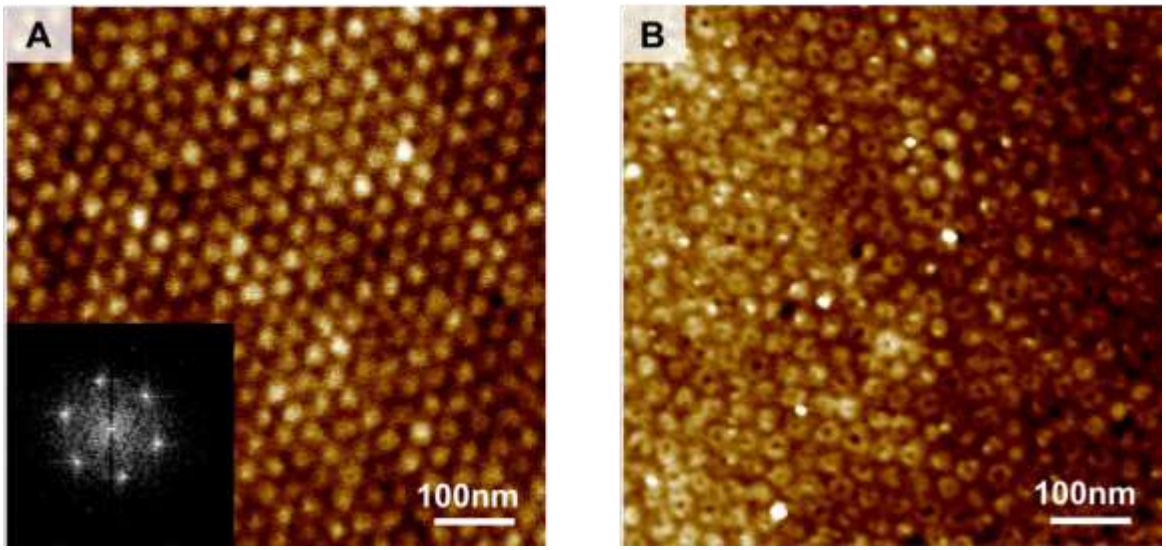

Figure 5.2.2. A solvent reconstruction of a PS-*b*-PTACCy thin-film. (A) The pre-reconstructed AFM topography image of PS-b-PTACCy ($N = 220, \phi_{CN-BCP} = 0.78$) film surface morphology after solvent vapor annealing. (B) The post-reconstruction AFM topography image of film surface morphology.

To corroborate this assessment, we set out to use AFM to measure the PS-b-PTACCy surface composition via a specialized mode – peakforce quantitative nanomechanical mapping. The beauty of this mode is it compares for the cantilever interactions with film surface during tip approach and retraction providing a measurement the surface adhesion that can be mapped across the sample surface. This mode of mapping is quite important as we expect very different types of interactions with the silicon nitride cantilever from the PS and PTACCy blocks – *i.e.* Van der Waals vs. electrostatic interactions. Figure 5.2.3A presents an AFM topography image for a solvent vapor annealed thin-film and the corresponding adhesion mapping in presented Figure 5.2.3B. The circular domains, the discrete phase, have a much lower adhesion for the silicon nitride cantilever than the matrix indicated by the dark brown and bright yellow regions respectively. PS block is expected to have weaker, Van der Waals, interactions with the AFM cantilever than the PTACCy

block's electrostatic interactions. These results, combined with the selective swelling surface reconstruction experiments, confirm that the PS blocks forms the discrete phase of the PS-*b*-PTACCy thin-film morphology. This is consistent with results found in chapter 2 – the PS block forms the discrete phase of the assembly.

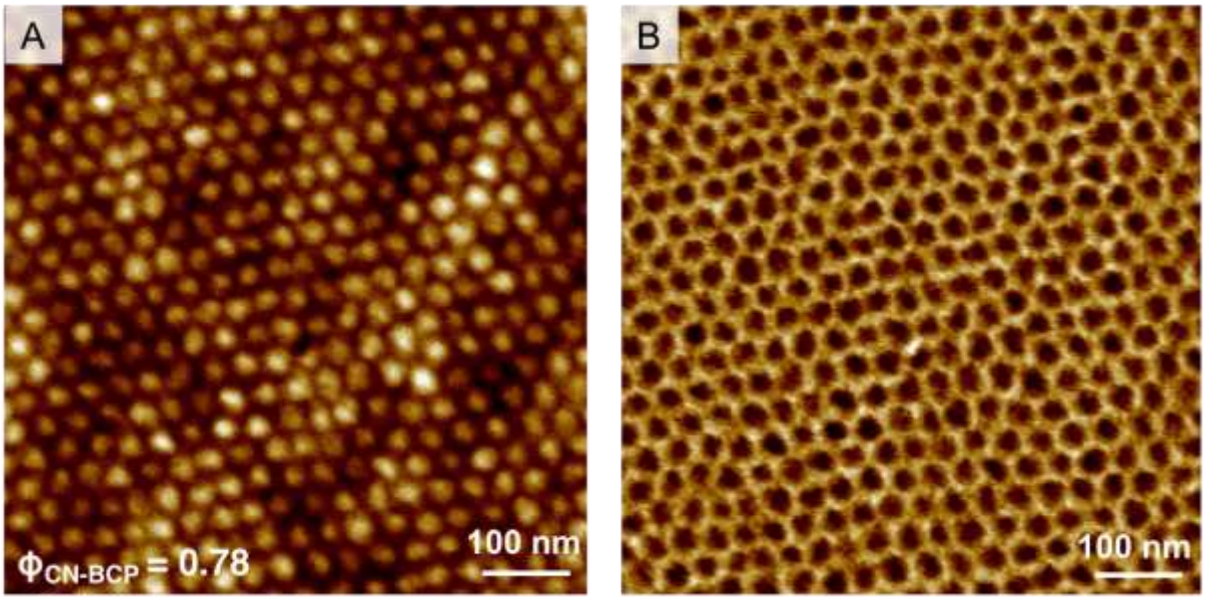

Figure 5.2.3. Atomic force microscopy nanomechanical mapping of a self-assembled PS-*b*-PTACCy thin-film. The AFM (A) topography and adhesion (B) image of PS-b-PTACCy ($N = 220, \phi_{CN-BCP} = 0.78$) film surface morphology after solvent vapor annealing.

Now that we confirmed AFM can be used to obtained a preliminary measure of the PS-*b*-PTACCy we preformed the same analysis on all the PS-b-PTACCy CN-BCPs listed in Table 5.2.1. The results of this analysis are presented in section 5.4 in the context of thin-film morphology mapping.

5.3 Quantification of PS-*b*-PTACCy surface and film domain organization

In the previous section, we observed that solvent vapor annealing facilitates the spontaneous self-assembly of PS-b-PTACCy into hexagonally packed PS domains. In this section, we will attempt to quantify the extent of ordering that can be obtained through solvent vapor annealing using a combination of surface analysis and GISAXS. Additionally, we evaluate if the

solvent vapor annealing process can be used to refine the PS-b-PTACCy thin film structure through repetitive annealings of a film.

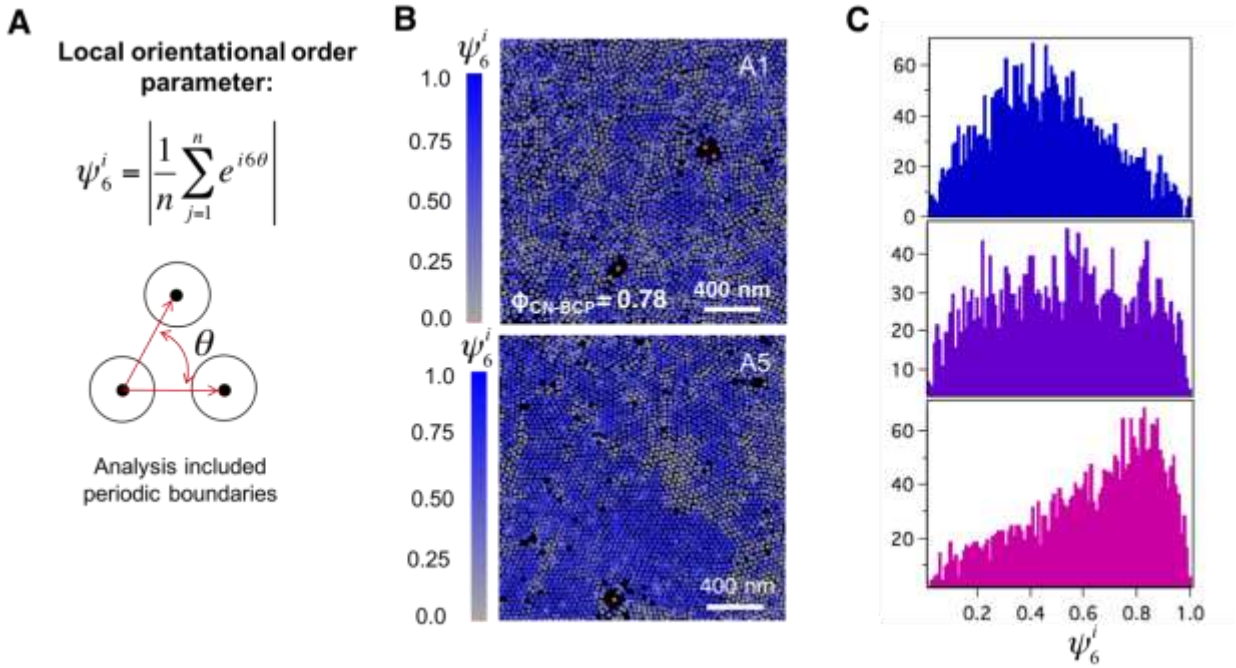

Figure 5.3.1. A quantification of hexagonal ordering in self-assembled PS-b-PTACCy thin-films. (A) a mathematical description of the local orientational order parameter with a schematic representation of the input parameter, θ. (B) The AFM images were discretized using the domain's center of mass, the ψ_6^i was calculated for each domain, and the ψ_6^i was mapped across the entire AFM image. A1 and A5 represent PS-*b*-PTACCy PS-*b*-PTACCy ($N = 220, \phi_{CN-BCP} = 0.78$) thin films annealed once and five times respectively. (C) the ψ_6^i frequency of occurrence plotted vs. ψ_6^i for PS-*b*-PTACCy PS-*b*-PTACCy ($N = 220, \phi_{CN-BCP} = 0.78$) films annealed once (top), three times (middle), and five times (bottom).

For this study we chose to use a PS-b-PTACCy ($N = 220, \phi_{CN-BCP} = 0.78$) $h = 40$ nm thin film since we have previous knowledge of thin-film's composition and structure. A single film was subjected to multiple solvent vapor annealings using the optimal annealing conditions (1:1 v/v DCM:MeOH) and after each vapor annealing the persistence of ordering was quantified using the two complimentary methods. From the surface morphology, we can quantity the extent of hexagonal packing by calculating the local hexagonal ordering parameter, ψ_i^6, defined by Eq (5.3.1), for every single PS domain[117–120].

$$\psi_i^6 = \left|\frac{1}{n}\sum_{j=1}^{n} e^{i6\theta}\right| \quad (5.3.1)$$

Here, $\psi_i^6$is calculated for each domain, *i*, and θ, the subtended angle between nearest neighbors, is calculated and averaged across all nearest neighbors, *n.* A schematic of how θ is determined for each nearest neighbor is provided in Figure 5.4.1A. It should be noted that an individual AFM image provides only a local description of the surface morphology ($4\,\mu m^2$ per image) and to acquire a statistical representation across the film surface we averaged over 15 images ($60\,\mu m^2$). Figure 5.3.1B are ψ_i^6 mappings for PS-*b*-PTACCy ($N = 220, \phi_{CN-BCP} = 0.78$) $h\ =\ 40$ nm thin films annealing once (A1) and five (A5) times. Qualitatively, a lot of useful information can be obtained from observing the different ψ_i^6 mappings. The deep blue regions represents perfect local hexagonal packing ($\psi_i^6 = 1$) and alternatively the red domains represents a liquid-like local ordering of domains ($\psi_i^6 = 0$). The PS-*b*-PTACCy A1 sample show small patches of hexagonal grains ($\sim$200 nm in diameter) suggesting a low persistence of hexagonal ordering. However, after repeative annealing the persistence of ordering increases significantly. The PS-*b*-PTACCy A5 sample we approximate the hexagonal grains size to be $\sim$ 1000 nm in diameter and a factor of 4 – 5 larger than A1. The increase in hexagonal ordering after multiple solvent vapor annealings suggests that the PS-*b*-PTACCy morphology is enriched through repetitive solvent vapor annealing cycles.

To elucidate a trend in growth of hexagonal ordering we extended the ψ_i^6 calculations to PS-b-PTACCy thin films solvent vapor annealed once (A1), three (A3), and five (A5) times. The ψ_i^6 mapping represents an agglomerate of discrete calculated ψ_i^6 values for each PS domain rounded to the nearest $\psi_i^6 = 0.01$ in a single AFM image. Instead of looking at the sum of the parts we tabulated the frequency of occurrence for each ψ_i^6 value average over all AFM images taken for a given annealing (*i.e.* A1, A3, and A5 separately) and compiled a histogram of the results

in Figure 5.3.1C. The histogram that represent the PS-*b*-PTACCy thin films annealing once, three, and five times are provided as the deep blue, purple, and pink respectively. As the number of times the PS-*b*-PTACCy thin films is solvent vapor annealed increases so does the most frequently occurring ψ_i^6 ($\psi_{i,ave}^6$). For A1, A3, and A5 we find $\psi_{i,ave}^6 \sim 0.4$, ~ 0.6, and $\psi_{i,ave}^6 \sim 0.85$ respectively which provides confirmation of the general trends observed in the ψ_i^6 mappings.

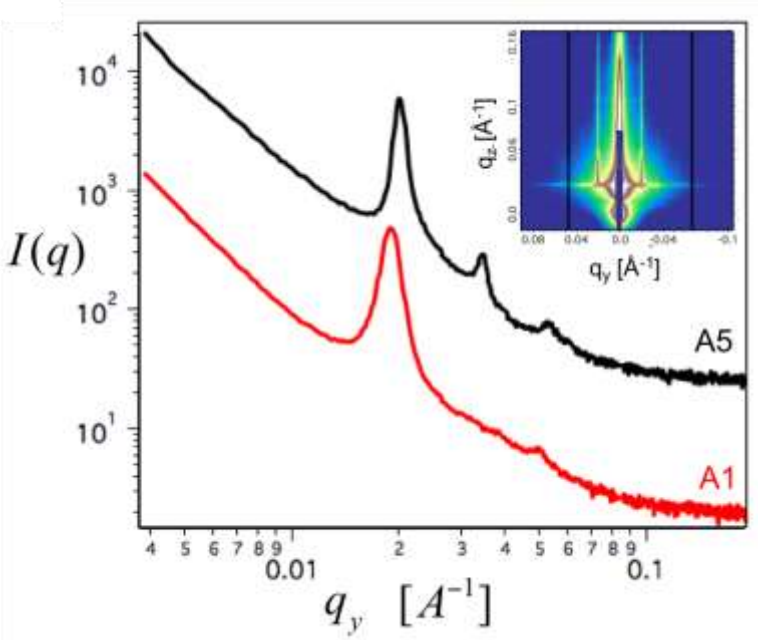

Figure 5.4.2. GISAXS of PS-b-PTACCy thin-films subjected to repetitive solvent vapor annealings. The in-plane scattering intensity ($I(q)$) plotted vs. q_y for a PS-b-PTACCy ($N = 220, \phi_{CN-BCP} = 0.78$) thin-films annealed once (red trace, A1) and five times (black, A5). The inset, the 2D scattering intensity for a PS-b-PTACCy ($N = 220, \phi_{CN-BCP} = 0.78$) thin-film annealed five times. The provided in-plane scattering intensity reflects a horizontal linecut taken at $\alpha_f = \alpha_c$.

To compliment the ψ_i^6 mappings presented in Figure 5.3.1, we conducted GISAXS experiments on PS-b-PTACCy films annealed once and five times. The incidence angle for each experiment was set to $\alpha_i = 0.14^\circ$ and the 2D scattering intensity was recorded using a 2M Pilatus 2-D area detector. Horizontal line cuts were taken at $\alpha_f = \alpha_c$ and plotted in Figure 5.3.2. The red and black trace reflect the linecuts for a sampled annealed once and five times respectively. The collected 2D imaged for A5 is provided as an inset of Figure 5.3.2. The Bragg rod streaks in the

qz scattered intensity indicate truncation of a 2D crystal and suggests the PS domains are cylindrical and oriented normal to the silicon interface [35,36].For the A5 in-plane scattering, we observe peak of intensity at q/q* ratios of 1: √3: √4: √7:√9 consistent with a 2D hexagonal structure factor [37] The scattering intensities of the √4 and √9 peaks are suppressed due to the nodes from form factor. [37,38] The primary bragg reflection (q*) for each trace was fit to gaussian distributed yielding the average domain spacing ($d = 2\pi\sqrt{4/3}/q^*$) and the peak width which contains information related to the persistence of hexagonal ordering in the PS-b-PTACCy film. The found d found for each film is consistent with the spacings found using the surface analysis. The measured primary bragg reflection peak widths (Δq) were converted into the average hexagonal grain size (GB) using Eq (5.3.2).

$$GB = 2\pi/\Delta q \tag{5.3.2}$$

For the PS-*b*-PTACCy films annealing once and fives times the GB were determined to be ~240 nm and ~ 900 nm respectively. The measured *GB* reflects the qualitatively observed hexagonal grain sizes in the ψ_i^6 mappings and directly supporting the surface analytical results.

5.4 PS-*b*-PTACCy thin-film morphology diagram – comparison to bulk morphologies

A large portion of this chapter has been devoted to the characterization of the PS-*b*-PTACCy thin film structure and composition, however, the primary goal of this work was to compare the thin-film and bulk PS-b-PTACCy morphology diagrams and examine the impact of confinement on the self-assembly. The PS-*b*-PTACCy bulk morphology diagram contains an unusually large C_N phase space. Interestingly, given the results presented in section 5.3, we find a similar structure in the solvent vapor annealed PS-b-PTACCy thin-films. On one hand, we slowly condense the PS-b-PTACCy CN-BCPs into a thick film from a nonselective solvent (MEK), and on the other,

solvent vapors are used to drive PS-b-PTACCy thin films into nonequilibrium morphologies[121–123]. The fact that both methods produce the same morphology suggests that perhaps the C_N morphology is substantially preferred even when subjected to solvent mediated interactions[124,125].

Therefore, we constructed a PS-*b*-PTACCy thin-film morphology diagram to compare to the results fond in chapter 2. The PS-*b*-PTACCy CN-BCPs listed in Table 5.1.1 were used in the construction the thin-film morphology mapping. When constructing the PS-*b*-PTACCy thin-film morphology diagram we kept the dry state film thickness was fixed at $h = 40$ nm. Many studies have demonstrated the importance of the thin-film thickness on the confinement. Additionally, since the polymer film is thin, surface interaction are significant and accounting for the preferential wetting[126–128] of each block for either the substrate or free interface plays an important role in determining the film thickness in which the copolymer feels a confining force[127–135]. Given these considerations, Each PS-*b*-PTACCy thin film was solvent vapor annealing follow the bell jar procedure outline in section 5.2. For each annealed film, the surface and film morphologies were determined using AFM and GISAXS respectively. Figure 5.4.1 presents all the unique PS-b-PTACCy thin-film morphologies observed across the morphology diagram. Figure 5.4.1A, B, and C are variations of the PS-*b*-PTACCy ($N = 220, \phi_{CN-BCP} = 0.78$) annealed film previously discussed in section 5.2 and 5.3. From the surface reconstruction experiments we determined the PS block forms the discrete phase of the assembly and this was used as a guide in analyzing Figures 5.5.1 D, E, and F. We find only two unique structures across the entire morphology mapping – C_N (Figure 5.4.1D and E) and disordered (Figure 5.4.1F).

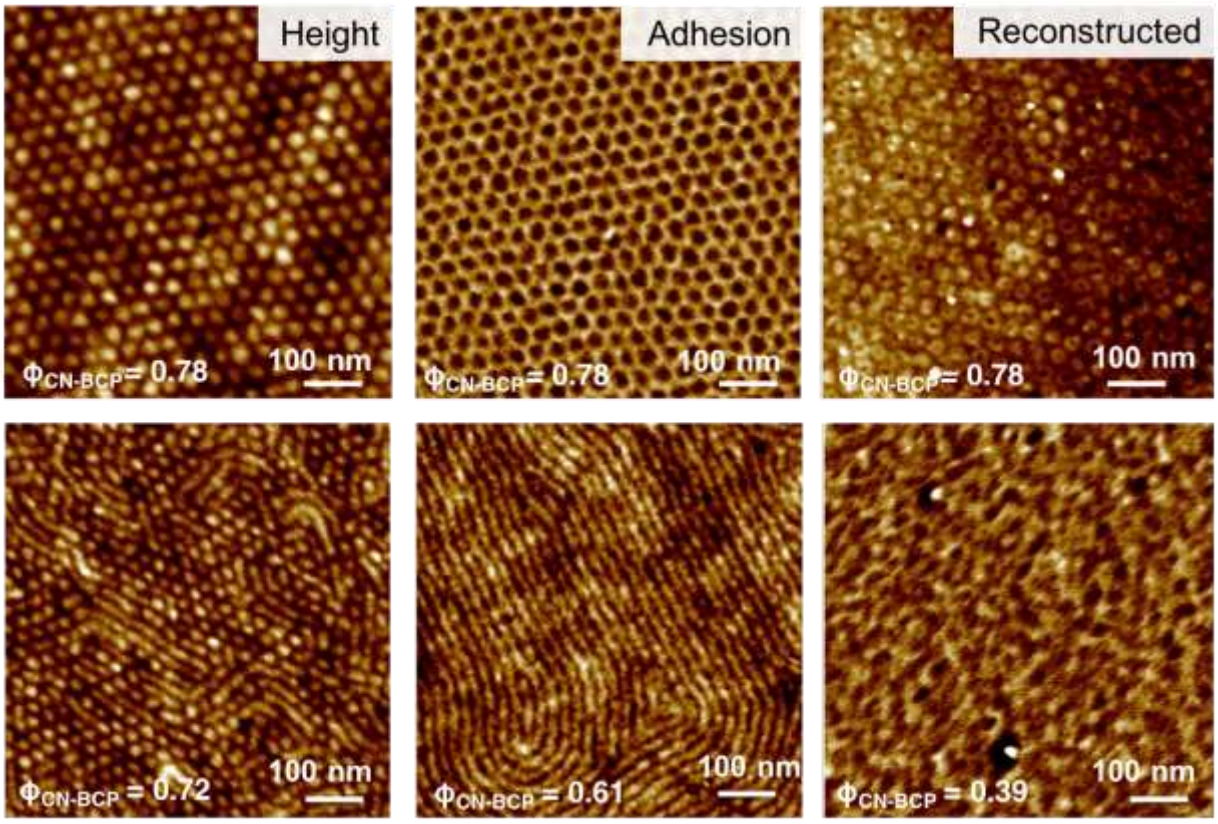

Figure 5.4.1. A summary of the all self-assembled PS-b-PTACCy thin-film surface morphologies. The AFM topography (A), adhesion (B), and reconstructed surface topography (C) image of the PS-*b*-PTACCy $N = 220, \phi_{CN-BC} = 0.78$ thin-film morphology. The AFM surface topographies of PS-*b*-PTACCy $N = 190, \phi_{CN-BCP} = 0.72$ (D), $N = 120, \phi_{CN-BCP} = 0.61$ (E), $N = 150, \phi_{CN-BCP} = 0.38$ (F) thin-film morphology.

In the bulk morphology mapping we observed three distinct structures, spheres (S_N), cylinders (C_N), and lamellae (LAM). These morphologies are separated spatial within the morphology diagram by the phase boundaries found at $\phi_{CN-BCP} = 0.4$ and $\phi_{CN-BCP} = 0.78$ for the LAM – C_N and C_N – S_N order – order transitions (OOTs) respectively, and bulk morphology diagram is provided in Figure 5.4.2B as a reference. Interestingly, these distinct OOTs are missing in the PS-b-PTACCy thin-film morphology diagram presented in Figure 5.4.2A. In fact, the C_N – LAM OOT at $\phi_{CN-BCP} = 0.4$ has been replaced with an order – disorder transition (ODT). Perhaps, this stark contrast in morphology diagrams is a manifestation confinement influences on the PS-*b*-PTACCy self-assembly and in increased importance of surface interactions on the PS-*b*-

PTACCy self-assembly. Indeed, if we consider the PS-b-PTACCy CN-BCP, the PS block prefers to wet the free interface, due to the low PS interfacial tension[136], and the PTACCy block prefers to wet the SiO_2 interface. Perhaps the lack of structure parallel to the film surface is not indicative of an ODT but the formation of a layered morphology stacking parallel to the substrate surface. Preferential interactions with the substrate and free interface could lead to such a scenario, however, this structural organization is simply speculation due to the lack of evidence of its formation.

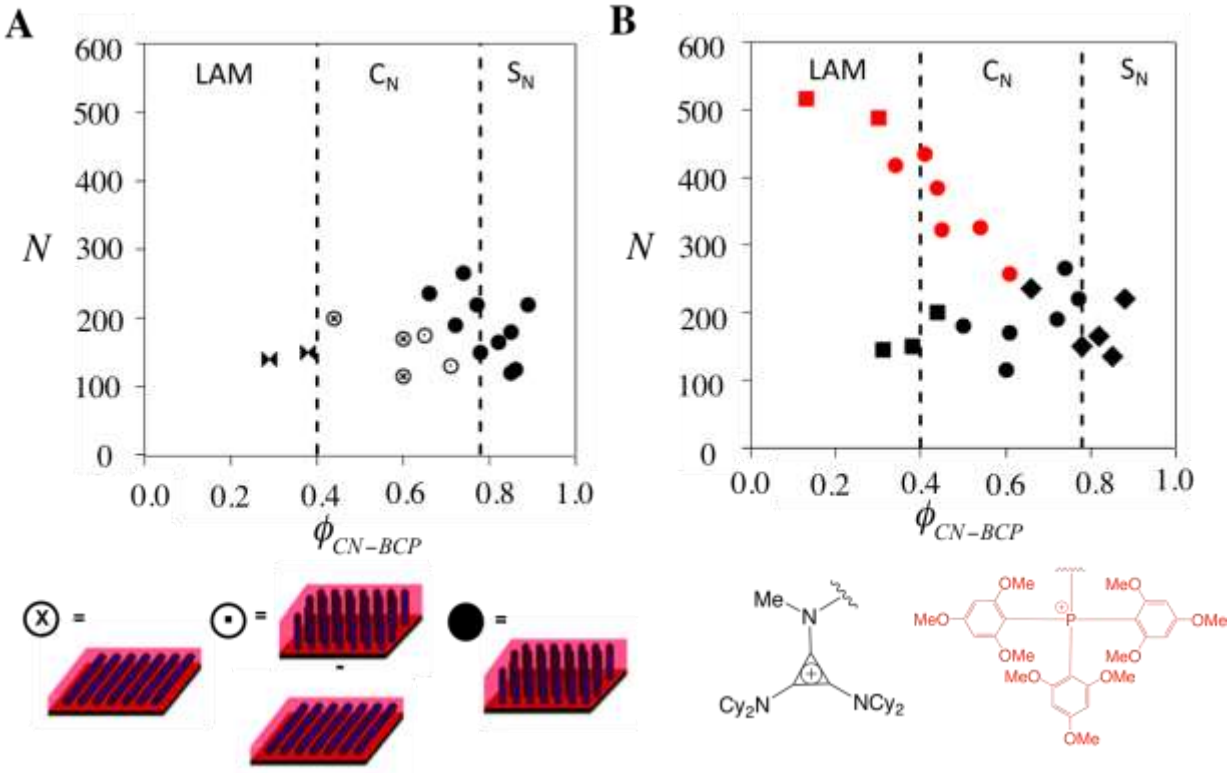

Figure 5.4.2. The PS-b-PTACCy thin-film morphology mapping. (A) The PS-*b*-PTACCy thin-film morphology diagram plotting the total degree of polymerization (N) vs. the PTACCy block volume fraction (ϕ_{CN-BCP}) for a constant film thickness ($h = 40$ nm). All reported structures were obtained after solvent vapor annealing. The various cylinder orientations are provided below their corresponding symbolic representation. The black bowtie represents a disordered thin-film. (B) The PS-b-PTACCy bulk morphology diagram presented in chapter 2. The probed region of N and ϕ_{CN-BCP} is the same for both morphology diagrams.

In addition to the loss of the C_N – LAM order – order transition we also observe do not observe the C_N – S_N order – order transition. Similar to the justification for the loss of the C_N –

LAM order – order transition, the culprit for this observation is likely interfacial driven interactions. If we consider the spherical morphology, the PS domain suspended within a PTACCy matrix, forces the PTACCy block to we the SiO_2 surface and free interface. However, we the PS block has a much lower surface energy and likely drives the presence of the domain at the free surfaces. The absence of both OOTs reinforces that surface energies have a pronounced impact on the PS-*b*-PTACCy thin-film assembly. However, one component of the PS-b-PTACCy thin-film morphology diagram reflects the influence of confinement - the cylindrical orientation transition as the ODT is approached. When the ϕ_{CN-BCP} is large we observed a dominate presence of PS cylinders oriented normal to the substrate surface, however, when the ϕ_{CN-BCP} approaches the ODT the dominant cylinder orientation switches to parallel with the substrate surface. The origins of the observed domain orientational switch will be discussed in the next section by probing the PS-*b*-PTACCy thin-film domain orientation thickness dependence near and far from the ODT.

5.5 The impact of confinement on domain orientation and process pathway engineering of PS-b-PTACCy thin-film morphology

To complete this chapter, we will briefly discuss observations of confinement and how these principles manifest in the PS-b-PTACCy morphology diagram. For all the PS-b-PTACCy thin film samples we only have their dry state film thickness. If we were discussing thermal annealing then the dry state film thickness would be the confining length scale, however, since we are discussing solvent vapor annealing the proper confining length scale is be the swollen state film thickness[133] which have not yet been determined. Therefore, the primary talking points for this chapter will be the domain orientation film thickness dependence and the impact of N and ϕ_{CN-BCP} on the observed thickness dependence.

In the context of the PS-b-PTACCy morphology diagram we can consider the film thickness as an additional axis as long as the film processing history does not impact the CN-BCP morphology. We picked two PS-b-PTACCy CN-BCPs on our thin film morphology mapping to study the film thickness dependence, one far ($N = 220, \phi_{CN-BCP} = 0.78$) and near ($N = 170, \phi_{CN-BCP} = 0.61$) the C_N – disordered ODT where the PS cylinders orient normal and parallel to the substrate surface respectively. Regardless of the PS-b-PTACCy film thickness the PS-b-PTACCy sample far from the ODT has no thickness dependence –PS cylinders oriented normal to the substrate surface for every film thickness. The sample close to the ODT ($N = 170, \phi_{CN-BCP} = 0.61$) on the other hand has a very rich thickness dependence which is provided in Figure 5.5.1. Figure 5.5.1 A – E are AFM topography images of solvent vapor annealed PS-b-PTACCy ($N = 170, \phi_{CN-BCP} = 0.61$) thin films with thicknesses of $h = 35, 40, 50, 60,$ and 70 nm respectively. As the film thickness increases the cylinder domain orientation oscillates from normal to parallel orientation – a hallmark of film confinement.

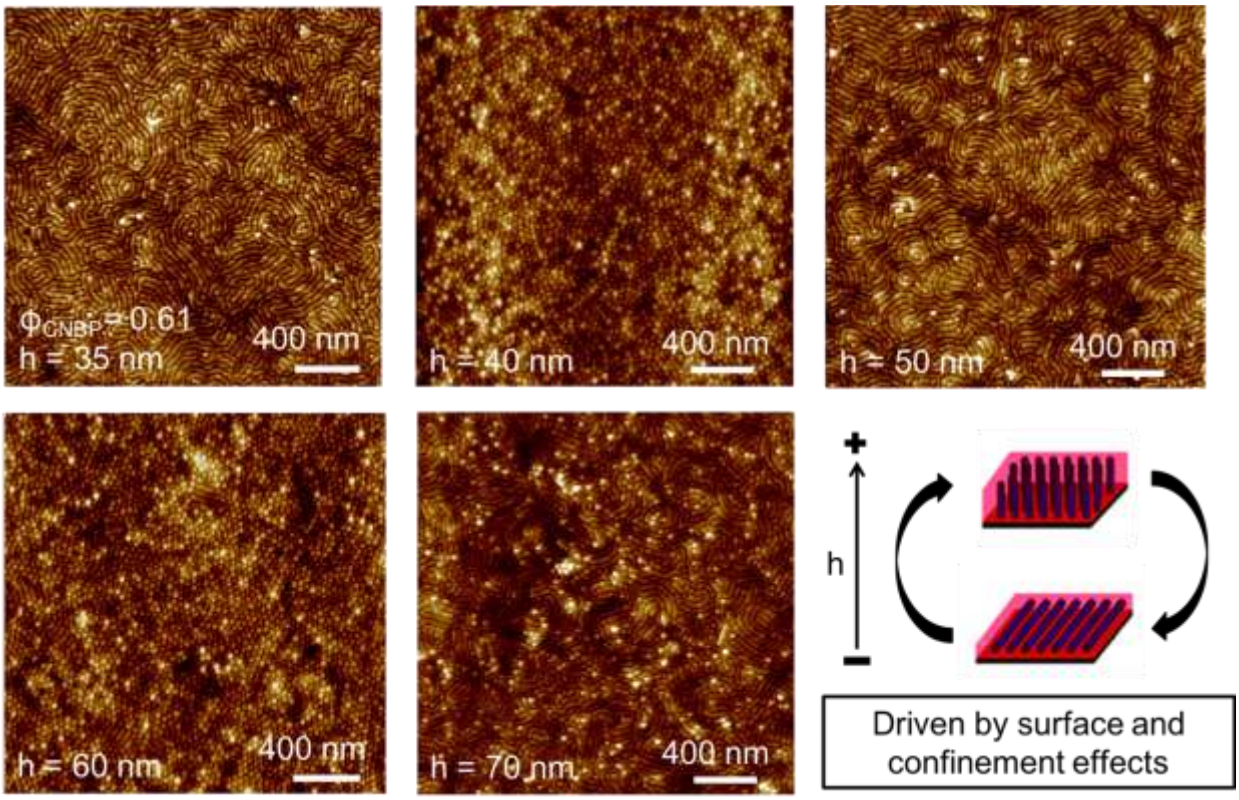

Figure 5.6.1. The PS-b-PTACCy thin-film domain orientation thickness dependence. AFM topography images of solvent vapor annealed PS-*b*-PTACCy ($N = 170, \phi_{CN-BCP} = 0.61$) thin-film of thickness $h = 35$ (A), 40 (B), 50 (C), 60 (D), and 70 (E). The schematic provided next to (E) shows the influence of increasing film thickness on the surface morphology.

Now that we had established a thickness dependence for PS-*b*-PTACCy $N = 170, \phi_{CN-BCP} = 0.61$ thin films, we will attempt to use this as an advantage to access both cylindrical orientations with the same film. The key achieving this goal was recognizing that the swollen state film thickness can be manipulated by choice of annealing solvents. This principle is demonstrated in Figure 5.5.2. Figure 5.5.2A is a AFM topography image take after solvent vapor annealing a with 1:1 (v/v) ratio of methanol to dichloromethane inside the annealing chamber. We see the expected morphology – cylinders orientated normal to the substrate surface.

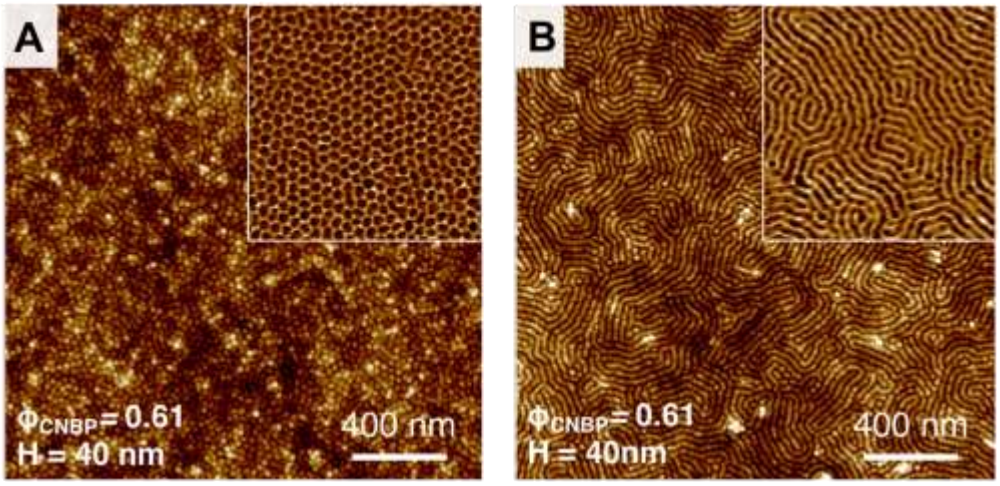

Figure 5.5.2. A reversible domain orientation switch using solvent vapor annealing on a single PS-*b*-PTACCy film. (A) the AFM topography image of a PS-b-PTACCy ($N = 170, \phi_{CN-BCP} = 0.61$) $h = 40$nm thick thin-film annealing with the optimal solvent vapor annealing conditions. The inset is a portion of the corresponding adhesion image. (B) an AFM image take after the same film was subsequently solvent vapor annealed with 2-butanone. The inset is a portion of the corresponding adhesion image.

If the annealing solvents are exchanged for 2-butanone and the same sample is annealed again we have the surface morphology given in Figure 5.6.2B. Figure 5.6.2B shows an AFM topography image of the film surface where the PS domains have switch to parallel orientation. This process cycle can be repeat to reversibly switch back and forth between cylinders oriented normal and parallel to the substrate surface. The difference between the two annealing conditions lies in the difference between dichloromethane ($39.6°C$) and 2-butanone ($79.6°C$) boiling points. The lower boiling point solvent produces less swelling of the PS-b-PTACCy thin-film and a lower swollen-state film thickness. Therefore, the two different solvent systems provide access to two separate swollen-state film thicknesses and two completely different confinement states.

Chapter 6: In situ grazing incidence small angle x-ray scattering investigation of PS-b-PTACCy thin-film self-assembly

Charge – neutral diblock copolymers (CN-BCPs) containing a low static dielectric constant (ε_r) are a difficult class of materials to thermally equilibrate due to presence of strong ionic interactions. As a result, it is imperative to decouple processing effects on the assembly so that kinetically trapped structures can be differentiated from equilibrium morphologies. To do this, solvent vapor annealing, a technique designed to rapidly organize polymer thin films into kinetically trapped nonequilibrium morphologies, was employed to probe the solvent's influence on the PS-*b*-PTACCy morphology. Atomic force microscopy and *in situ* grazing incidence small angle x-ray scattering techniques were utilized to quantify the PS-*b*-PTACCy assembly before, after, and during the solvent vapor annealing process. The influence of solvent selectivity on the PS-*b*-PTACCy process annealing pathway and solution phase behavior was determined. The impact of ionic interaction strength on the PS-b-PTACCy self-assembly was explored using annealing solvents with ε_r that span a range of $\varepsilon_r = 4.8 - 38.3$. We find the PS-*b*-PTACCy average periodicity and hexagonal grainsize can be reduced by ~ 8 nm and increased by a factor of 2 respectively by increasing the annealing solvent ε_r. Across all the annealing solvent used in this study there was no discernable change on the final PS-*b*-PTACCy thin-film morphology indicating the C_N is stable over a wide range of solvent conditions for PS-b-PTACCy CN-BCPs.

6.1 Materials and methods.

Before moving on to the experimental part of this section, we will first briefly discuss the PS-b-PTACCy synthesis (a detailed procedure can be found in section 2.1). All materials were purchased from Sigma-Aldrich and were used without further purification. Styrene was polymerized using a previously reported procedure.[21] Copper (I) bromide and tris(2-pyridylmethyl)amine were added to a dry Schlenk flask and the material was deoxygenated via five vacuum-argon cycles. Degassed styrene was added to the flask and allowed to stir for 10 minutes under argon until the solution turned light green, indicating that the Cu complex formed. The Schlenk flask was closed under argon and degassed ethyl α-bromoisobutyrate was injected. The reaction mixture was heated to 90 °C and allowed to react overnight. The polymer was dissolved in tetrahydrofuran (THF), filtered through an alumina column, precipitated twice into a stirred solution of cold methanol, and vacuum dried overnight. The molecular weights and Đ of the final material were determined using GPC calibrated with polystyrene standards.

After isolation, the polystyrene macroinitiator was used in a subsequent chain extension polymerization. Copper (I) bromide and tris(2-pyridylmethyl)amine were added to a dry Schlenk flask and the material was deoxygenated via five vacuum-argon cycles. Degassed tert-butyl methyl(4-vinylbenzyl)carbamate was added to the flask and allowed to stir for 10 minutes under argon until the solution turned light green, indicating the Cu complex formed. The Schlenk flask was closed under argon and degassed polystyrene macroinitiator anisole solution was injected. The mixture was subjected to three freeze-pump-thaw cycles to ensure all oxygen was removed from the reaction vial. Then the reaction mixture was heated to 90 °C and allowed to react overnight. Aliquots were taken at different times and examined by ^{1}H NMR to determine conversion and gather information related to the kinetics of the chain extension reaction. The final polymer was

dissolved in THF, filtered through an alumina column, precipitated three times into a stirred cold methanol/water solution, and vacuum dried overnight. The molecular weights and Đ of the final material was determined using GPC. The poly(tert-butyl methyl(4-vinylbenzyl)carbamate) block (PNBoc) degree of polymerization was determined using ^{1}H NMR.

The PS-*b*-PNBoc then prepared for functionalization by first deprotecting the tert-butyl ester group on the PNBoc chain. The PS-*b*-PNBoc was dissolved in a 50/50 DCM: MeOH solution (15 mL) in a round bottom flask under argon. The flask was cooled to 0˚C and trimethylsilyl chloride was added. The reaction was allowed to stir at room temperature overnight and then concentrated under vacuum to yield a white powder. The powder was then re-dissolved in DMSO and 1 M NaOH was added dropwise until the polymer precipitated from solution. The resulting slurry was centrifuged, and the supernatant decanted. The deprotected polystyrene-b-poly(4-methylaminostyrene) (PS-*b*-PMAS) polymer was washed twice with DI water, and collected via centrifugation, and dried under vacuum. PS-*b*-PMAS was dissolved in chloroform in a scintillation vial. In parallel, *N,N*-diispropylethylamine was added to the another scintillation vial, followed by a solution of TACCy in 4 mL of Chloroform. The two solutions were combined, and the reaction mixture was heated to 65 °C and allowed to react overnight. The resulting solution was concentrated *in vacuo*, dissolved in methanol, transferred into a 3.5 kDa MWCO Spectrum Labs dialysis bag, and allowed to dialyze in a methanol bath for three days. The bath was replaced with fresh methanol twice per day. The resulting colloidal solution was concentrated under vacuum to yield a light amber powder, a purified PS-*b*-PTACCy linear diblock copolymer. The ^{1}H NMR chemical shifts and integrations have been reported for this material in a previous publication.[21,22]

In this chapter we focus only on a single PS-b-PTACCy CN-BCP and Table 6.1.1 provides a list of the relevant physical parameters.

Table 6.1.1. Physical parameters of PS-b-PTACCy CN-BCP linear diblock copolymer prepared for *in situ* GISAXS investigation.

Sample	$M_{n,PS}\ [kDa]$[a]	$M_{n,PTACCy}\ [kDa]$[b]	N	ϕ_{Cn-BCP}[c]	Đ[d]
PS_{175}-b-$PTACCy_{115}$	68.1	18.2	290	0.79	1.17

[a]The $M_{n,PS}$was determined using THF mobile phase GPC calibrated with polystyrene standards. [b]$M_{n,PTACCy}$ was determined using H^1 NMR and the procedure outline in chapter 1. [c]The ϕ_{Cn-BCP} was calculated using the know bulk densities of each component ($\rho_{PS} = 1.04\ g/cm^3$, $\rho_{PTACCy} = 1.06\ g/cm^3$) and the known number of monomer in each block (N_{PS}, N_{PTACCy}). [d]The dispersity index (Đ) of PS_{175}-b-$PTACCy_{115}$ was determined using THF mobile phase GPC calibrated with polystyrene standards.

The PS-*b*-PTACCy CN-BCP was dissolved in methylethylketone (MEK) at 10mg/mL solution concentration, filtered through a 0.2 micron Teflon filter, and stirred overnight. In the interim, Si wafers were diced into 1 cm^2 square substrates then solvent washed sequentially with acetone, methanol, dichloromethane, acetone, and isopropyl alcohol, under a constant sonication. The PS-b-PTACCy CN-BCP was spun coated onto the cleaned Si wafer where the average film thickness (h) was modulated via adjusting the chuck's number of revolutions per minute (RPM). To obtain a $h = 40,\ 55,$ and 90 nm we used 3000, 1500, and 1000 RPM respectively. Directly after spincoating each film was placed under vacuum to remove an residual solvent in preparation for solvent vapor annealing and the *in-situ* GISAXS experiments.

6.2 Experimental set-up: determine critical angle, incident angle, quantification

Solvent vapor annealing is a widely employed technique to structure polymer thin-film and many focus on determining the key parameters in this annealing process[123,137–139]. The swelling ratio[137] (*i.e.* solvent volume fraction (ϕ_s)) has been proposed as a critical parameter related to the phenomena governing solvent vapor annealing. To capture the essence of the bell jar experiment discussed in chapter 5 it is imperative to obtain high swelling ratios, *i.e.* large ϕ_s, which is challenging using most standard *in situ* annealing cells[137]. Therefore, to mimic the bell jar annealing experiments, we chose the following cell shown schematically in Figure 6.2.1 for our *in-situ* GISAXS experiments.

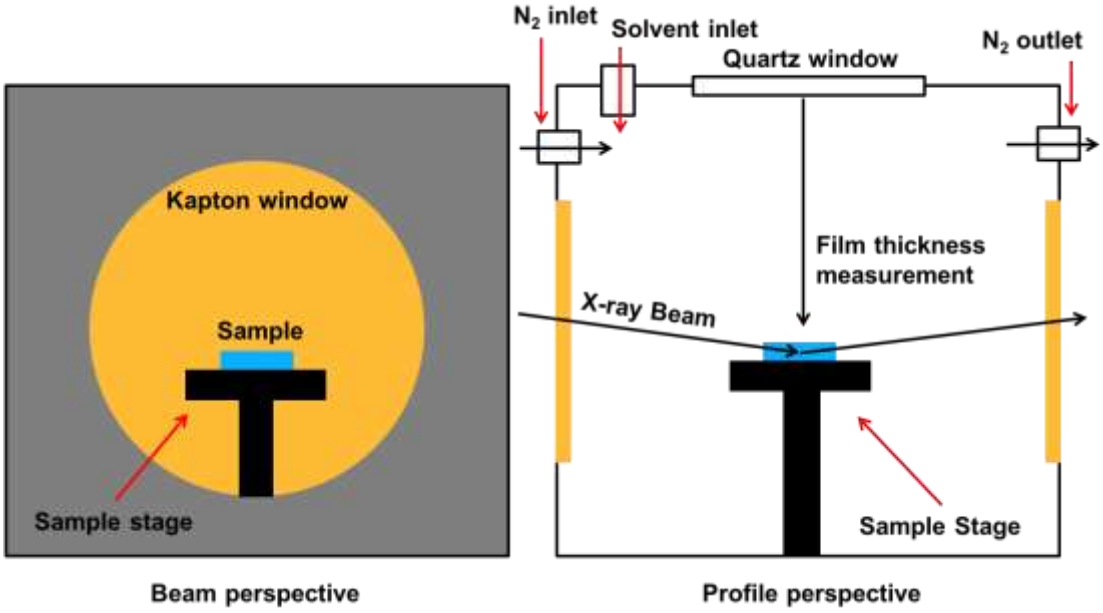

Figure 6.2.1. A schematic representation of the in-situ solvent vapor annealing chamber. On the left, a face-on view of the cell taking into account the perspective of the incoming beam. On either side of the sample stage are two Kapton windows and resting on the stage is the sample on which the GISAXS experiment is conducted. On the right, is a profile view of the sample cell. Here, all the functionality of the cell is elucidated. The quartz window on the top of the cell allows for a measurement of the film thickness. The solvent inlet is located at the top of the cell and allows for solvent to injected into the cell directly injected. Finally, at the top of the cell are inlet and outlet ports for overhead N_2 gas flow.

This cell allows for *in-situ* GISAXS experiments through the Kapton windows on polymer thin-film samples mounted on the indicated sample stage. The beauty of this cell design is the ability to inject solvent directly into the annealing chamber through the injection inlet port located at the top of the cell. Placing the solvent directly in the annealing chamber allows for higher solvent vapor pressures to be achieved within the cell (*i.e* higher ϕ_s) akin to the bell jar experiment. The quartz window at the top of the cell allows for a real-time measurement of the thin-film thickness during the vapor annealing experiment using a Filmetrics F20 interferometer. Additionally, at the top of the cell, there are N_2 inlet and outlet ports that can provide an overhead gas flow for an instantaneous control of the solvent vapor pressure inside the chamber.

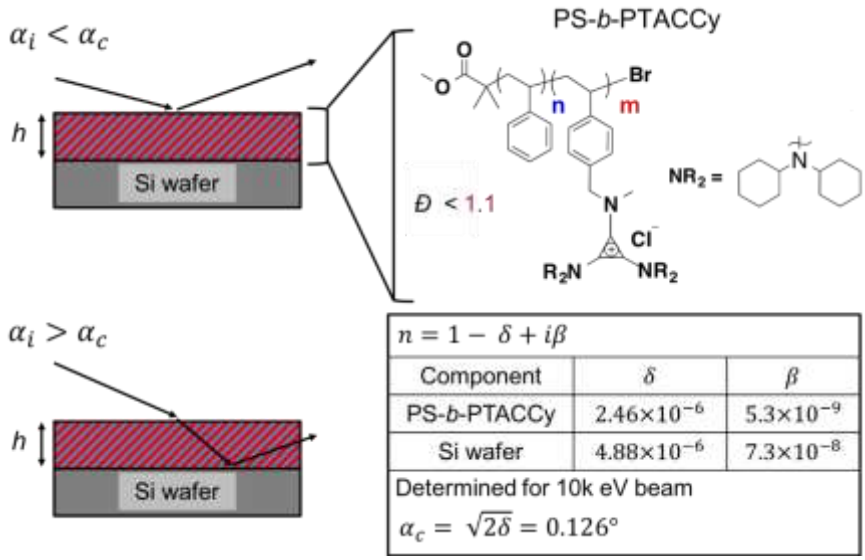

$n = 1 - \delta + i\beta$

Component	δ	β
PS-*b*-PTACCy	2.46×10^{-6}	5.3×10^{-9}
Si wafer	4.88×10^{-6}	7.3×10^{-8}

Determined for 10k eV beam

$\alpha_c = \sqrt{2\delta} = 0.126°$

Figure 6.2.2. A summary of relevant parameters for GISAXS experiments. (left) Two possible GISAXS scattering experiments depending on the incident angle (α_i) of the incoming x-ray beam with respect to the critical angle of the PS-*b*-PTACCy film (α_c). (right) Accounting for the chemical composition of the PS-*b*-PTACCy macromolecule and below there is a table all the components necessary to calculate the refractive index at 10k eV. When considering a GISAXS, the α_c is an important parameter to determine and can be calculated using $\alpha_c = \sqrt{2\delta}$, and a PS-*b*-PTACCy thin-film $\alpha_c = 0.126°$.

Once the vapor annealing sample cell was chosen, we then determined the appropriate incident angle (α_i) for the GISAXS experiments. To do this, we first calculated the PS-b-PTACCy critical angle (α_c) using the information provided in Figure 6.2.2.

$$\alpha_c = \sqrt{2\delta} = 0.126^{\circ} \tag{6.2.1}$$

If $\alpha_i < \alpha_c$ then the PS-b-PTACCy film is completely reflective to the incoming x-ray beam and the GISAXS experiment is only sensitive to the film surface structure. When $\alpha_i > \alpha_c$ then the incoming x-ray beam can penetrate the PS-b-PTACCy film and by analyzing the scattered intensity we can deduce information related the film structure. For every *in situ* annealing experiment $\alpha_i = 0.14^{\circ}$ ($\alpha_i > \alpha_c$) was maintained and the evolution of the PS-b-PTACCy film morphology was examined as a function of annealing time.

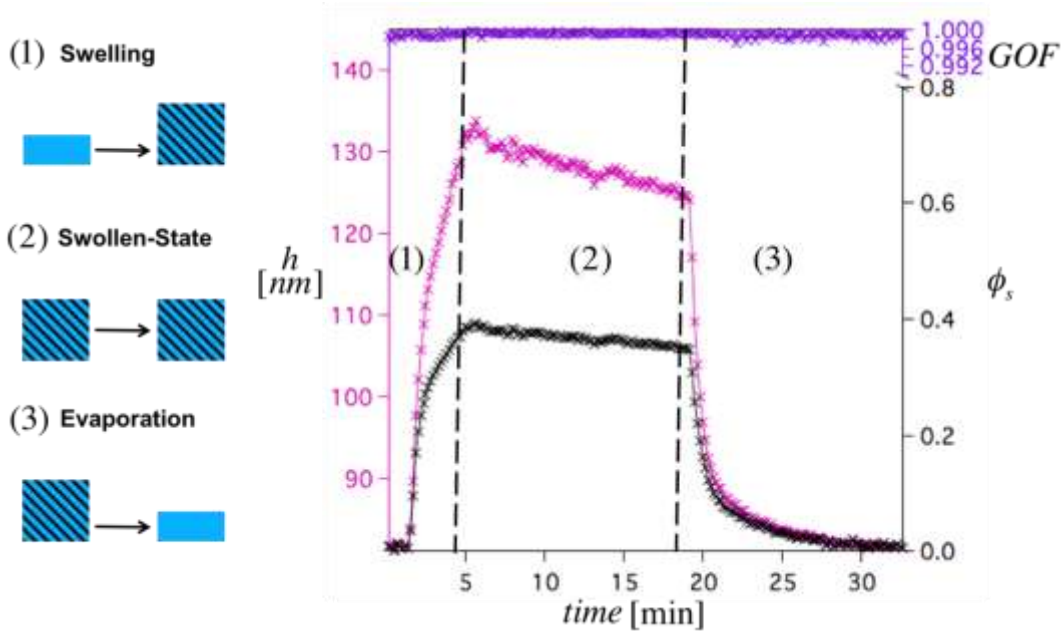

Figure 6.2.3. Overview of the PS-b-PTACCy film thickness measuring during vapor annealing. During the *in-situ* GISAXS solvent vapor annealing experiment, the PS-*b*-PTACCy film undergoes three separate phases, (1) swelling, (2) equilibration in the swollen-state, and (3) solvent evaporation. On the left are cartoon representations of each stage of the experiment. On the right, we have a plot that quantitatively captures each step of the experiment. In purple, pink and black we plot the goodness of fit (GOF), film thickness (h) and the ϕ_s are plotted as a function of experiment time.

The *in-situ* GISAXS provides structural information about the PS-b-PTACCy film during the solvent vapor annealing process and it is useful to correlate with the ϕ_s to understand morphological transitions[137]. In these experiments, the ϕ_s is not determined directly but calculated from the PS-b-PTACCy film thickness (h) during the solvent vapor annealing experiment. With this in mind, we measure the PS-b-PTACCy film thickness using a Filmetrics F20 interferometer taking advantage of the quartz window at the top of the annealing chamber. During the *in situ* annealing experiment, the PS-b-PTACCy undergoes three critical stages, (1) swelling, (2), equilibration in the swollen state, and (3) evaporation. All three steps are labeled and schematically represented in Figure 6.2.3. Figure 6.2.3 plots the data acquired from the interferometer during the *in situ* experiment. The light purple, pink and back data points are the goodness of fit (GOF), h, and annealing solvent volume fraction (ϕ_s) respectively are plotted *vs.* experimental time. Assuming the film can only swell normal to the substrate surface, ϕ_s is calculated using Eq (6.2.3).

$$\phi_s(t) = \frac{h(t)-h(t=0)}{h(t)} \tag{6.2.2}$$

Where $h(t)$ and $h(t=0)$ are the swollen PS-b-PTACCy film thickness at time *t* and the initial dry state PS-b-PTACCy film thickness respectively.

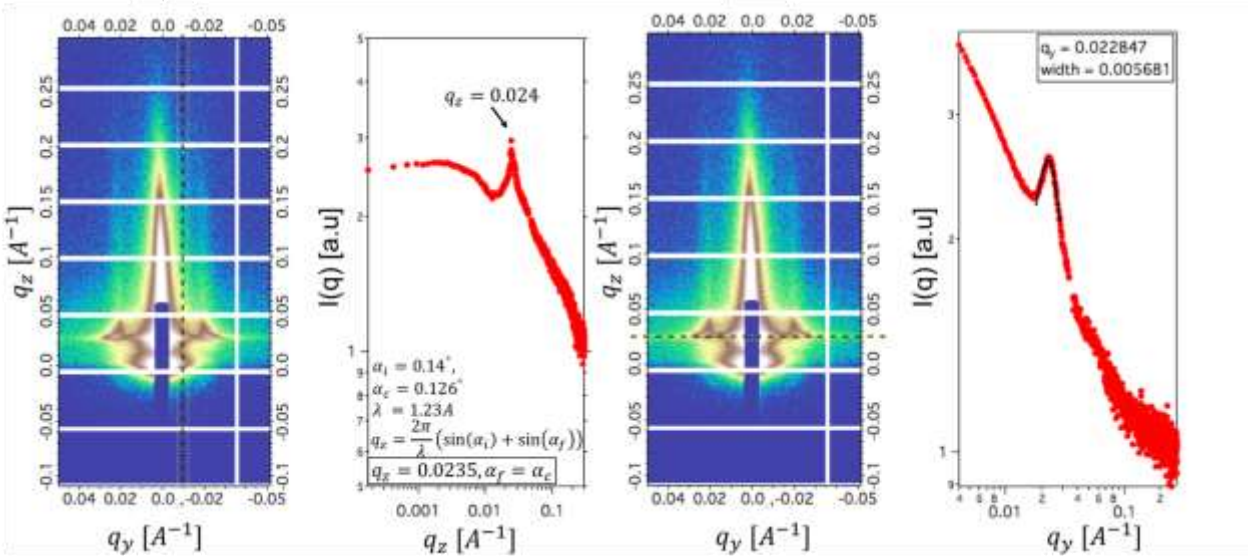

Figure 6.2.4.PS-b-PTACCy α_c and PS-b-PTACCy in-plane structural analysis (A) the 2D scattering intensity and (B) a vertical linecut taken at the dotted line (--) where the scattering intensity *I(q)* is plotted vs. q_z. The q_z of maximum intensity reflects the criterion $\alpha_f = \alpha_c$ and using Eq. 6.2.4 an estimation q_z that satisfies this criterion is provided. (C) The 2D scattering intensity and (D) a horizontal linecut is taken at the dotted line (--) plots the *I(q)* vs. q_y to elucidate the in-plane PS-*b*-PTACCy film structure. The primary bragg reflection was fit to a normal distribution.

Now, that we have a good measure of $\phi_s(t)$ during the annealing experiment, we briefly discuss analysis of the PS-b-PTACCy film structure. Data acquisition during each in situ experiment was set to 1-minute intervals by fixing the exposure time to 5 seconds and enforcing a delay time of 55 seconds. For each exposure, a 2D image of the scattering intensity $I(q)$ is collect on a Pilatus 2M detector (Figure 6.2.4A & C). The $I(q)$ is discretized with respect to q_y and q_z which can be determined using Eq (6.2.3) and Eq (6.2.4) respectively and applying Pythagorean theorem they can be converted into q using Eq (6.2.5).

$$q_y = \frac{2\pi}{\lambda}\left[\sin(\theta_f)\cos\left(\alpha_f\right)\right] \tag{6.2.3}$$

$$q_z = \frac{2\pi}{\lambda}\left[\sin(\alpha_i) + \sin\left(\alpha_f\right)\right] \tag{6.2.4}$$

$$q = \sqrt{q_y^2 + q_z^2} \tag{6.2.5}$$

Where θ_f, α_f, and θ_i are parameters that define the geometry between the incoming and exiting x-ray beam. Simulating the $I(q)$ is nontrivial and outside the scope of the work presented here, however, we do confirm the initial assessment of the PS-b-PTACCy α_c. A vertical linecut (close the beam stop) was taken on Figure 6.2.4A and the $I(q)$ *vs.* q_z is plotted in Figure 6.2.4B The yoneda peak ($q_{z,yoneda}$) occurs when $\alpha_f = \alpha_c$ and here we find $q_{z,yoneda} = 0.024\, A^{-1}$. Substituting $\alpha_c = 0.126^{\circ}$ and $\alpha_i = 0.14^{\circ}$ into Eq 6.2. the calculated $q_{z,yoneda} = 0.0235\, A^{-1}$ which in close agreement with the experimentally determined value. Shifting the attention to the PS-*b*-PTACCy in-plane film structure, we take a horizontal linecut of the 2D spectra at the $q_{z,yoneda}$ indicated by Figure 6.2.4C. The $I(q)$ plotted vs. q_y in given in Figure 6.2.4D and represents the structure of the PS-b-PTACCy film parallel to the substrate surface – *i.e.* the in-plane structure. The in-plane primary bragg reflection was fit to a gaussian distribution and the peak maximum (q^*) corresponds to the average in-plane domain spacing (d) and the peak width (Δq) is used to determine the average crystalline grain size (GB). Both d and GB are calculated using the following relationships respectively.

$$d = 2\pi\sqrt{4/3}\,/q^* \tag{6.2.6}$$

$$GB \sim 2\pi/\Delta q \tag{6.2.7}$$

The $\sqrt{4/3}$ prefactor in Eq (6.2.6) relates the longest hexagonal lattice plane to the average domain spacing[140] for a 2D hexagonal array. Additionally, Eq (6.2.7) is a simplified variation of the classical scherrer analysis to estimate the average crystalline grain size (*GB*).

6.3 Diagnosis of optimal solvent system.

Prior to conducting the *in-situ* GISAXS experiments we first preformed a bell jar vapor annealing experiment using the optimal annealing conditions (1:1 v/v DCM: MeOH for 24 hr) on a PS-b-PTACCy ($N = 290, \phi_{CN-BCP} = 0.79$) $h = 40$ nm thin-film. Figure 6.3.1 shows AFM

topography images of the PS-b-PTACCy surface morphology before (left) and after (middle) solvent vapor annealing and capturing the film's structural evolution through this annealing pathway. On the left, the *as cast* PS-b-PTACCy film topography shows a set polydisperse circular structures indicating microphase segregation has occurred despite the complete lack of ordering. After solvent vapor annealing, the PS-b-PTACCy film was dried in vacuum and the surface morphology was measuring using AFM. The annealed AFM topography image (Figure 6.4.1 middle) shows of the PS-b-PTACCy film after vapor annealing. Qualitatively, after vapor annealing the PS domains have organization into a well-defined hexagonally packed structure. Using imageJ software, the Fourier transform of the annealing surface was taken (Figure 6.4.1 right) and the concentric isotropic rings of intensity indicate a local hexagonal ordering. The primary reflection (indicated by the white arrow) can be used to extract the average domain spacing using Eq. (6.2.6). The average domain spacing was determined to be $d = 32$ nm which will be used as a benchmark to compare to the results obtained from the *in-situ* GISAXS experiments.

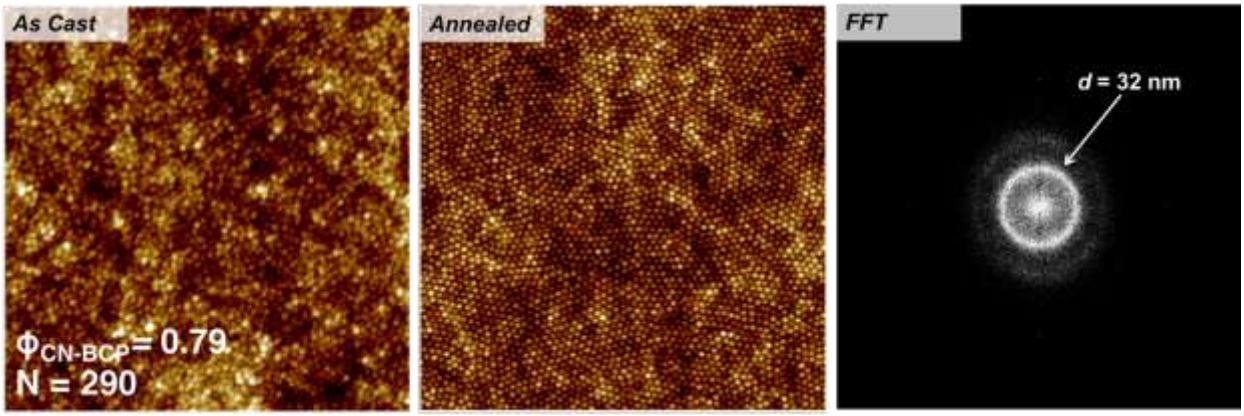

Figure 6.4.1. Surface morphology of a solvent vapor annealed PS-b-PTACCy ($N = 290, \phi_{CN-BCP} = 0.79$) film. (Left) an AFM image of the *as-cast* spun coated PS-*b*-PTACCy ($N = 290, \phi_{CN-BCP} = 0.79$) film. (Middle) an AFM image of the same film subjected to optimal solvent vapor annealing conditions for 24 hours. (Right) The Fourier transform of the annealed film surface morphology imageJ software.

To gain a preliminary understanding of the processing pathway PS-*b*-PTACCy thin-films undergo during solvent vapor annealing, we designed three experiments using the optimal annealing conditions where annealing solvent reservoir volume inside the chamber is sequentially increasing. The results of each experiment are provided in Figure 6.3.2 and the conditions for each experiment are provided in Table 6.3.1. The PS-b-PTACCy d, normalized hexagonal grain size (GB/d), and ϕ_s are plotted in Figure 6.4.2 with respect to the experimental run time.

Table 6.4.1. Summary of vapor annealing conditions

Experiment No.	No. 1 (Left)	No. 2 (middle)	No. 3[a] (Right)
Conditions	0.5 mL MeOH 0.5 mL DCM 0.1 LPM constant N_2 overhead flow	1 mL MeOH 1 mL DCM 0.1 LPM constant N_2 overhead flow	2 mL MeOH 2 mL DCM Periodic modulated N_2 overhead flow

[a]The periodic modulated N_2 overhead flow was achieved via manually adjustment of the flow rate.

Experiments No. 1, 2, and 3 correspond to the conditions used for the results presented in Figure 6.3.2 left, middle, and right respectively and reflect a sequentially increasing amount of annealing solvent reservoir added to the chamber (1mL, 2mL, and 4 mL total solvent reservoir volume). As expected, increasing the amount of solvent in the annealing chamber produces an increasing equilibrium ϕ_s ($\phi_{s,e}$) corresponding to $\phi_{s,e} \sim 0.35, 0.45$ and 0.7 respectively. In experiment No. 1 & 2 a constant overhead N_2 flow was utilized to suppress the maximum $\phi_{s,e}$ and help stabilize a constant $\phi_{s,e}$ for a longer duration of time. When the overhead N_2 flow is turned off completely (*i.e.* No. 3) the PS-b-PTACCy film can reach a larger $\phi_{s,e}$ ($\phi_{s,e} = 0.7$) but stabilizing the $\phi_{s,e}$ over a long period of time is difficult. In each experiment, the PS-*b*-PTACCy film appears to first undergo an order – disorder transition (ODT) which is represented by a complete loss of in-plane structure ($d = 0$, $GB/d = 0$). For both experiments No. 1 and No. 2, the PS-b-PTACCy film does not recover any in-plan structure until the solvent is evaporated from the film suggesting there is an ODT at $\phi_s \sim 0.3$. However, the PS-*b*-PTACCy does not stay

disordered for all $\phi_s > 0.3$. Experiment No. 3. Elucidates that the PS-b-PTACCy film undergoes another ODT at $\phi_s \sim 0.5$ and where we obvserve the formation of an ordered swollen state morphology that persists at large ϕ_s. The origins of these results will be discussed later, however, it is worth noting that swollen state structure is reversible and can be dissolved and reformed by cycling ϕ_s.

Turning our focus to the PS-b-PTACCy swollen state structure, we observe the domain periodicity increases with increasing ϕ_s. This result at first glance seems intuitive, however, the measured d represents the in-plane domain spacing (*i.e.* parallel to the substrate surface). Considering the PS-*b*-PTACCy film is constrained by the lateral dimensions of the substrate, an increase in d could indicates either (1) film is expanding laterally or (2) the PS-*b*-PTACCy film lateral dimensions are constant and the morphology is changing. The former scenario is physically unrealistic for the PS-b-PTACCy film cannot have a lateral dimension larger than the substrate, and latter is more likely occurring.

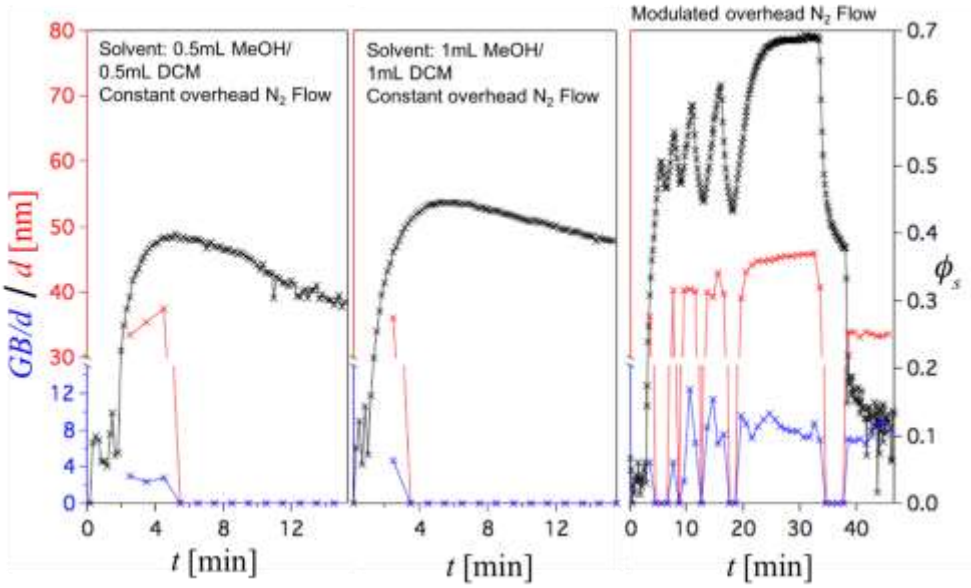

Figure 6.4.2. Three separate in-situ solvent vapor annealing experiments using the optimal solvent conditions. (Left) 0.5mL of methanol (MeOH) and DCM each were injected in the chamber with overhead N_2 flow (0.1 LPM). (Middle) 1 mL of methanol (MeOH) and DCM each were injected in the chamber with overhead N_2 flow (0.1 LPM). (Right) 2mL of methanol

(MeOH) and DCM were injected in the chamber with a modulated overhead N_2 flow (0.1 LPM). The black, red, and blue data points represent ϕ_s, PS-*b*-PTACCy CN-BCP periodicity (d), and the normalized average grainsize (GB/d) plotted *vs.* experimental time respectively.

Experiment No. 3 elucidated the presence of a second ODT where the PS-b-PTACCy film forms and ordered swollen-state morphology and we will to leverage this transition to refine the domain ordering in the swollen state. In the section 5.3, we discovered that sequential solvent vapor annealing a single PS-b-PTACCy thin film significantly increased the persistence of hexagonal ordering in the final condensed structure. Perhaps, we can mimic these results using a single solvent vapor annealing by cycling through the ordered swollen state repeatedly. To tackle this postulate, we examine the changes in the PS-*b*-PTACCy swollen-sate morphology over the course of multiple cycles between $\phi_s \sim 0.5$ and $\phi_s \sim 0.7$. Figure 6.4.3 (Left) plots d, GB/d, and ϕ_s vs. the experimental run time. As the PS-b-PTACCy film is cycled through the ordered swollen state the d only shows light variation that mirrors the changes in ϕ_s . However, the GB/d displays a different behavior. Each time the PS-b-PTACCy film is cycled through the swollen-ordered state the GB/d at the max ϕ_s has increased indicating a longer persistence of ordering. Figure 6.4.3 (right) plots the improved swollen state structure, qualitatively described by the sharpness of the primary bragg reflection, after each solvent cycle.

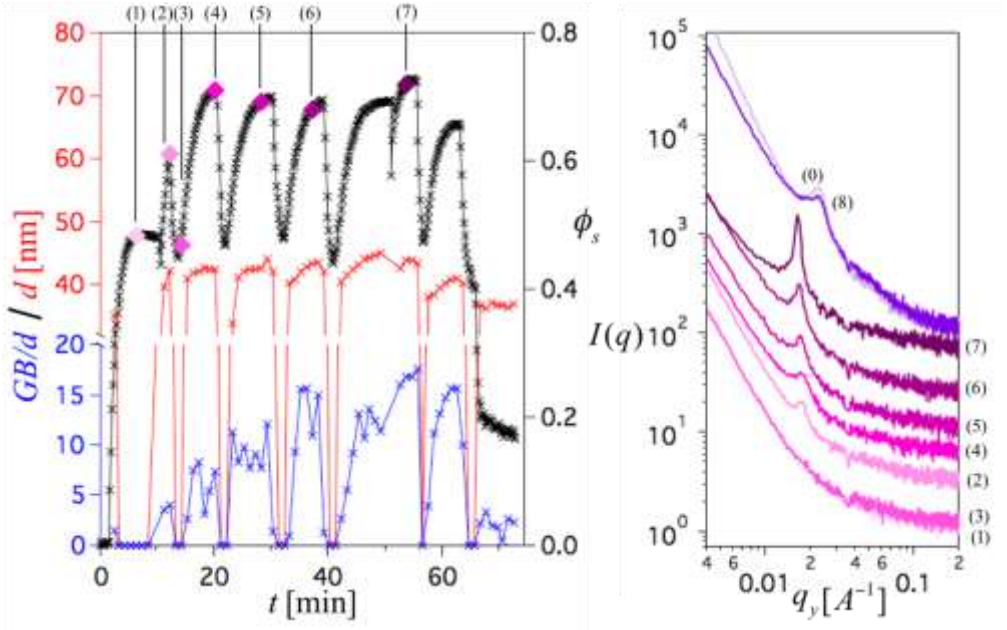

Figure 6.4.3. Refining the PS-b-PTACCy swollen-sate morphology. On the left, 1mL of methanol (MeOH) and DCM were injected in the chamber with a modulated overhead N_2 flow (0.1 LPM). the black, red, and blue data points represent ϕ_s, PS-*b*-PTACCy CN-BCP periodicity (d), and the normalized average grainsize (GB/d) are plotted as a function experimental time respectively. The indicated points (various shades of pink) correspond the indicated in-plane line cuts provided on the right. The intensity of the linecuts are shifted vertically for clarity, and the traces labelled (0) and (8) correspond to linecuts from before and after the *in-situ* experiment.

Dissolving and reforming the PS-*b*-PTACCy swollen state film morphology improved the persistence of ordering in the swollen state. However, at this time, it is unclear if any improvements in the swollen-state improvement translate into final condensed morphology. If simply cycling through the ordered swollen state can improve the resulting condensed film morphology, then perhaps this presents a new powerful method to creating highly ordered CN-BCP thin films.

6.4 Differentiating the impact of solvent type on thin-film self-assembly.

In the section we deconstruct the optimal annealing conditions into its elementary components and decipher the role of each solvent. We can categorize each annealing solvent into one of two types, nonselective and selective. A solvent that solvates both blocks equally is labeled "nonselective" and is thought to increase miscibility between the immiscible polymer blocks[137] in addition to increasing the total volume of the film. A solvent that preferentially solvates one of the

CN-BCP blocks is considered to be a "selective" solvent and cause a temporary increase the effective volume fraction of the solvated block[138] and can lead to an enhance segregation strength between the two block. The determined optimal solvent vapor annealing condition combines both types of solvent – a nonselective solvent (DCM) and a PTACCy selective solvent (MeOH). Both solvents were used individually the solvent vapor annealing of PS-b-PTACCy thin films and *in situ* GISAXS experiments were conducted to capture the impact of each solvent on the film morphology.

6.4.1 Nonselective solvents: vapor annealing with DCM.

Following the procedure outline in section 6.2, we performed *in-situ* GISAXS using pure DCM as the annealing solvent. In the absence of an N_2 overhead flow, 2 mL of DCM was injected into the annealing cell, the cell was sealed, and the experiment was initiated. The results of the PS-*b*-PTACCy film thickness during the solvent vapor annealing experiments are summarized in Figure 6.4.1.1. The light purple, black, and pink data points are the GOF, ϕ_s, and h respectively are the plotted as a function of experimental time. Due to the high DCM vapor pressure, the PS-b-PTACCy swells rapidly after solvent injection and reaches a swollen-state equilibrium in ~ 10 minutes. It should be noted that at $\phi_s > 0.5$ the solvent vapor pressure in the chamber reached the saturation limit as began to condense on the cell walls. This effect is evident with close inspection of the GOF. When $\phi_s > 0.5$ the GOF displayed significant deviated from unity which arises from condensation on the quartz window. To combat this effect, at $\phi_s > 0.5$, short bursts of N_2 overhead flow were used to dry the solvent from the top of cell and minimally impact the swollen PS-b-PTACCy film below. Once a swollen-state equilibrium state was achieved, determined by an unchanging PS-b-PTACCy film structure and a constant ϕ_s, an N_2 overhead flow of 0.5 LPM was used to completely dry the film.

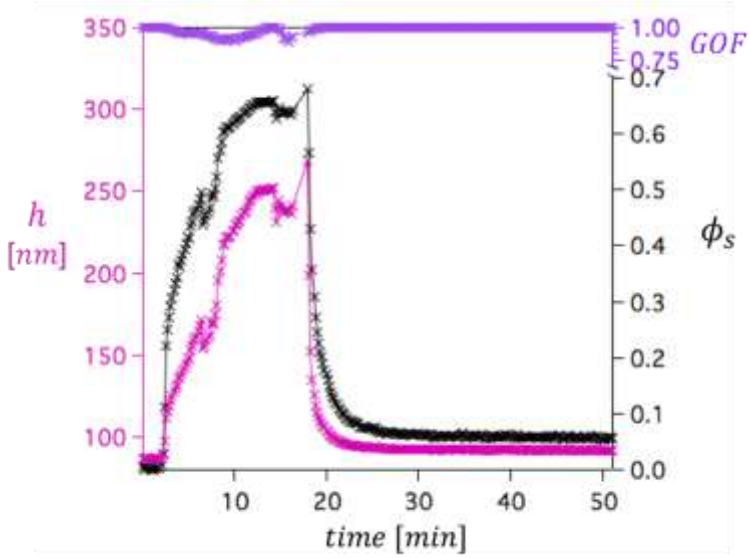

Figure 6.4.1.1. A plot of h vs. time using a nonselective solvent. 1mL of DCM was injected into the *in-situ* annealing chamber and the goodness of fit (GOF), film thickness (h) and the volume fraction of solvent in the film (ϕ_s) are plotted *vs.* experiment time.

During *in-situ* GISAXS experiment the PS-b-PTACCy d, GB/d and ϕ_s were tracked as a function of experimental time. Figure 6.4.1.2 plots the ϕ_s, d, and GB/d in black, red, and blue connected crosses respectively on the same time scale. At the start of the experiment, when the film begins to swells with DCM, the d increases suggesting that the assembled lattice is expanding. In contrast, the GB/d decreases with increasing ϕ_s indicating that the PS-b-PTACCy film is approaching the ODT. At ϕ_s ~0.5 the PS-b-PTACCy film has completely dissolved indicated by the loss of all in-plane structure ($d = 0, GB/d = 0$). For all $\phi_s > 0.5$ the disordered state persists until the evaporation step begins.

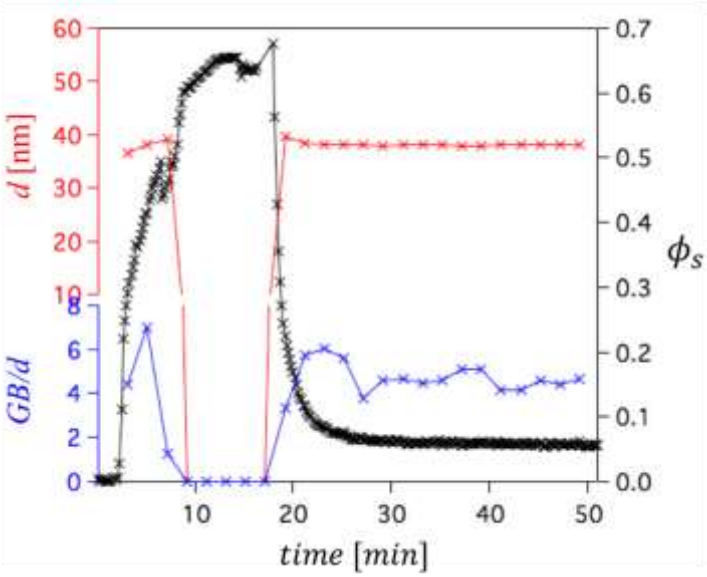

Figure 6.4.1.2. A summary of the PS-*b*-PTACCy film morphology during solvent vapor annealing with a nonselective solvent. 1mL of DCM was injected into the *in-situ* annealing chamber and the black, red, and blue data points represent ϕ_s, PS-*b*-PTACCy CN-BCP periodicity (d), and the normalized average grainsize (GB/d) are plotted as a function experimental time respectively.

In summary, the introduction of a nonselective solvent initially expands the film structure, presumably to incorporate the additional volume, then increases the miscibility between the PS and PTACCy blocks causing dissolution. This can be thought of as an ODT driven by solvent compatibilization.

6.4.2 Selective solvents: vapor annealing with methanol.

Following the same procedure outline in section 6.2, an *in-situ* GISAXS experiment was preform using pure MeOH as the annealing solvent. In the absence of an N_2 overhead flow, 2 mL of MeOH was injected into the annealing cell, the cell was sealed, and the experiment was initiated. It is important to keep in mind that the MeOH only swells the PTACCy phase of the assembly. In fact, MeOH is good solvent for the PTACCy block as the alcohol motif is known to form a hyperadduct with the chlorine counterion creating a more favorable ion pair[18,141,142]. Figure 6.4.2.1 summarized the PS-*b*-PTACCy film solvent vapor annealing experiment. The light purple, black,

and pink data points are the interferometer GOF, ϕ_s, and h respectively are the plotted *vs.* experimental time.

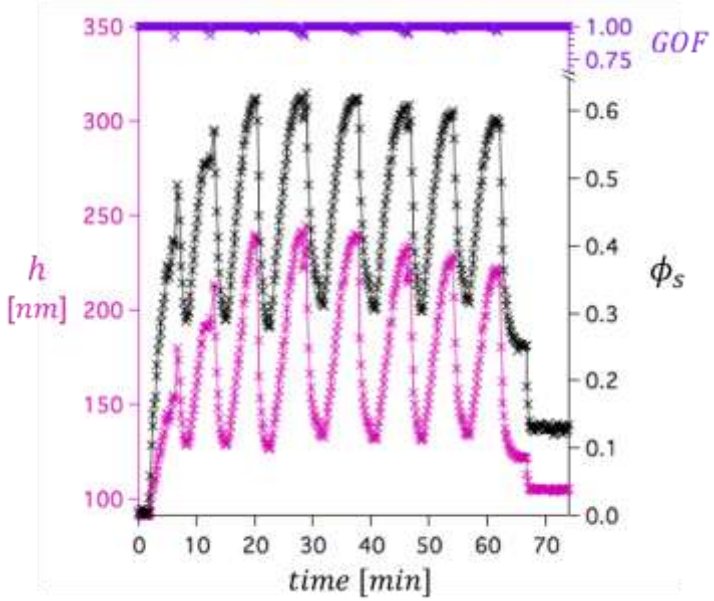

Figure 6.4.2.1. A plot of h vs. time using a selective solvent. 2mL of Methanol was injected into the *in-situ* annealing chamber and the goodness of fit (GOF), film thickness (h) and the volume fraction of solvent in the film (ϕ_s) are plotted as a function of experiment time. The large swings in solvent volume fraction was achieved through a periodic modulation of an overhead N_2 flow.

Upon the introduction of solvent into the annealing chamber, the film swells rapidly reaching a large ϕ_s. Instead of maintaining a constant ϕ_s, the N_2 overhead flow is periodically applied to cycle the PS-b-PTACCy through a large range of ϕ_s akin the experiment conducted in section 6.3. This experimental protocol was applied to probe the reversibility of theordered swollen-state morphology observed at $\phi_s > 0.38$. Figure 6.4.2.2 summarizes the PS-b-PTACCy film structure during solvent vapor annealing with MeOH. The PS-b-PTACCy d, GB/d, and ϕ_s are plotted *vs.* experimental run time using red, blue, and black crosses respectively. At the start of the experiment, The PS-b-PTACCy film structure appears to undergo two ODT transitions with increasing ϕ_s. The first ODT marks the loss of the original PS-*b*-PTACCy dry film ordering and the second ODT signifies the formation of an ordered swollen state morphology. Through repeat

cycling ϕ_s we determine the ODT between the ordered swollen state and disordered swollen film to occur at $\phi_s = 0.38$. One consideration to keep in mind is that d represents a measure of the domain spacing in the plane of the film and suggests that the film structure is changing to accommodate the increasing effective PTACCy volume fraction. In contrast, the GB/d remains constant across all ϕ_s and also does not improve with solvent cycling. Therefore, the selective solvent is not solely responsible for enhancement in ordering of the swollen state with increased solvent cycling, but, it is most-likely the driving force behind the formation of the swollen state structure. It should be noted that at time = 18 min the scattering position on the film was moved by 1 mm and is likely the cause for the sharp drop in GB/d. After 8 solvent cycles the film was evaporated down to dry PS-b-PTACCy film and the results film structure was probed.

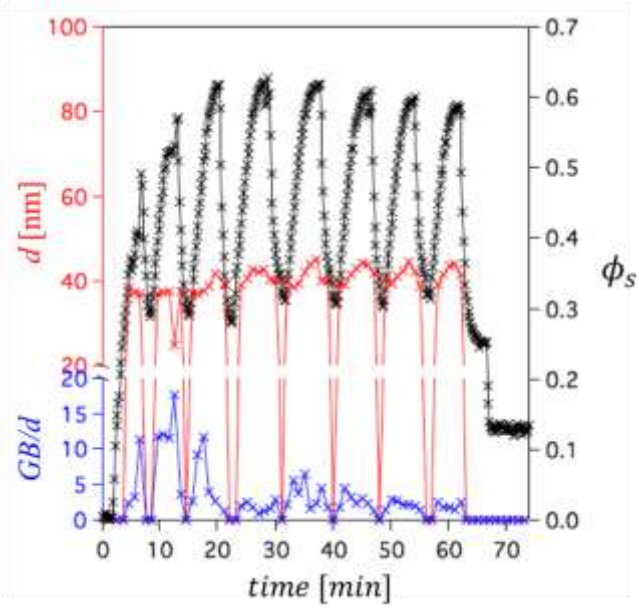

Figure 6.4.2.2. A summary of the PS-b-PTACCy film morphology during solvent vapor annealing with a selective solvent. 2mL of Methanol was injected into the *in-situ* annealing chamber and the black, red, and blue data points represent ϕ_s, PS-*b*-PTACCy CN-BCP periodicity (d), and the normalized average grainsize (GB/d) are plotted as a function experimental time respectively. The large swings in solvent volume fraction was achieved through a periodic modulation of an overhead N_2 flow.

In summary, as ϕ_s increases, the structure initially dissolves and then organizes into an ordered swollen state when $\phi_s > 0.38$. The origin of the disordered regime separating the ordered dry and swollen state assemblies is unknown at this time, however, we propose possible mechanism for this observed process pathway in the following section.

6.5 Pathway engineering assemblies: Annealing through an ordered swollen state

Sections 6.3 and 6.4 were devoted to breaking down the optimal annealing conditions (1:1 (v/v) DCM: MeOH) and analyzing the roles of each solvent plays in the solvent vapor annealing process. Figure 6.5.1 summarizes the PS-*b*-PTACCy solvent annealing process pathway dependence on solvent type (nonselective, selective, and solvent mixtures are represented by DCM, MeOH, and DCM/MeOH mixture respectively) . The plot on the left are morphology diagrams that track the PS-*b*-PTACCy structure as a function of ϕ_s. For the nonselective solvent, we find that after a critical ϕ_s ($\phi_{s,crit}$) all ordering is lost and does not recover as ϕ_s increases. This $\phi_{s,crit}$ represents an ODT for this solvent type and not a result of a possible contrast matching within the swollen film. The DCM scattering length density ($\rho_{SLD,DCM} = 1.14 \times 10^{-5}\ A^{-2}$) which larger than both $\rho_{SLD,PS} = 9.52 \times 10^{-6}\ A^{-2}$ and $\rho_{SLD,PTACCy} = 9.70 \times 10^{-6}\ A^{-2}$. Provided that DCM solvates both blocks equally, we expect to maintain contrast between the PS and PTACCy blocks during the solvent vapor annealing experiment in the swollen state.

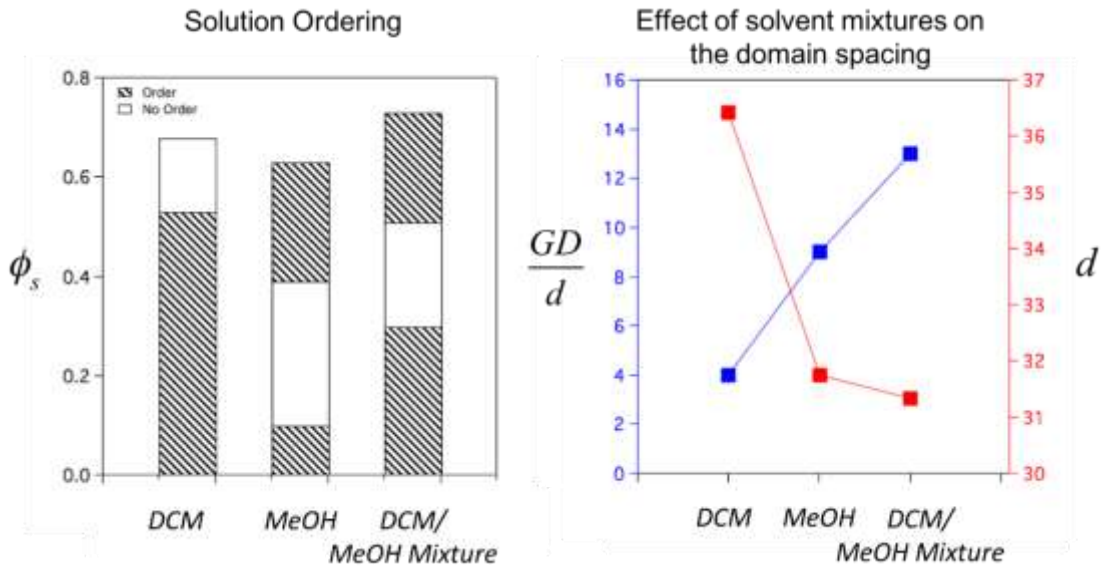

Figure 6.5.1. PS-b-PTACCy solution morphology diagrams. (Left) a summary of the PS-*b*-PTACCy CN-BCP structure as a function of increasing ϕ_s for the nonselective (DCM), the selective (MeOH), and the optimized annealing mixture (DCM/MeOH). (Right) the PS-b-PTACCy periodicity and normalized average grainsize after annealing with the three different solvent types.

Vapor annealing with methanol, a PTACCy selective solvent, guides the PS-b-PTACCy thin film through a completely different processing pathway. As shown in Figure 6.5.1, at low amounts of swelling, ϕ_s = 0.15, the PS-b-PTACCy thin-film appears to undergo a similar order-disorder transition as seen in the nonselective solvent case where the film loses all in-plane ordering. However, at ϕ_s = 0.38 the film undergoes a second transition into an ordered swollen-state which is believe to arise from the selective nature of the annealing solvent. As ϕ_s increases the ordered swollen state persists indicating the ordered structure is stable at large ϕ_s. This result might be expected since selective solvents are known to drive the formation of BCP micelles[143–145], however, an unexpected result is the loss of ordering between $\phi_s = 0.15 - 0.38$. Due to the insufficient contrast between the PS and PTACCy blocks, we are unable to observe an signature of a form factor in the disordered regime. Therefore, we are unable to confirm if there is a complete loss of structure as well as ordering. An important consideration to keep in mind is that is the

$\beta_{SLD,MeOH} = 7.58 \times 10^{-6}\, A^{-2}$ and lower than both $\beta_{SLD,PS} = 9.52 \times 10^{-6}\, A^{-2}$ and $\beta_{SLD,PTACCy} = 9.70 \times 10^{-6}\, A^{-2}$ which means that as PTACCy swells with methanol, the system will go through a contrast match point (CMP). The methanol CMP is estimated to occur at $\phi_s = 0.09$ assuming a volumetric weighting of the scattering length density in the solvated PTACCy block. The estimated CMS is close to the order-disorder transition, however, does not explain the lack of signal throughout the disordered regime as we expect to have sufficient contrast. Therefore, we suspect that the observed disordered regime is in reality a transitional state between the ordered cylindrical dry state and the ordered micellular structure in the swollen film. Finally, the PS-*b*-PTACCy solvent vapor annealing morphology mapping for the optimal annealing conditions (*i.e.* the mixture of DCM/MeOH) combines the phenomena observed from both the nonselective and selective solvents. Similar to the selective solvent case, for the optimal annealing conditions contains the same disordered transitional regime except at a higher ϕ_s. This is thought to occur from a shift in the CMS point to a higher ϕ_s due to the nonselective solvation of both blocks from the DCM and the miscibility between MeOH and DCM.

Figure 6.5.2 analyzes the final kinetically trapped morphologies provide by the three different processing pathways. Annealing with DCM yields the largest PS-*b*-PTACCy periodicity (d, red date points) and the smallest hexagonal grainsize (GB/d, blue date points). Interestingly, the DCM/MeOH mixture produced the most ordered kinetically trapped structure with $GB/d \sim 13$ and a d that is very similar to the MeOH annealed sample. The stark contrast in d between the PS-*b*-PTACCy films annealed with MeOH (pure MeOH and DCM/MeOH mixture) and without (pure DCM) suggests that perhaps the solvent identity may have a significant influence on the periodicity. Additionally, the similarity between the d of the samples annealed with MeOH most-likely occurs from the order of solvent remove in PS-b-PTACCy film during evaporation. The

boiling points of DCM and MeOH are 39.8°C and 64.6°C respectively, and therefore the DCM is expected to evaporate first leaving the MeOH to exit the film last and ultimately determine the final d of the assembly. The origin of the larger GB/d obtained from annealing with the optimal annealing conditions is known at this time.

6.6 Effect of dielectric medium of thin-film organization

In this final section we will explore the impact of solvent dielectric constant (ε_r) on the PS-*b*-PTACCy CN-BCP thin-film self-assembly. Specifically, we kinetically trap the PS-*b*-PTACCy films in non-equilibrium structures through rapid solvent evaporation that reflects the impact of the annealing solvent on the assembly. The Table 6.6.1 provides a list of all solvents chosen for this study. The annealing solvent's ε_r range from $\varepsilon_r = 4.8 - 38.3$ which are all greater than the intrinsic PTACCy ε_r, 2.5 – 3. Therefore, simply adding solvent into the PS-*b*-PTACCy films will not only mediate segmental interactions but also improve dielectric screening capabilities of the PTACCy block.

$$l_B = \frac{e^2}{4\pi\varepsilon_o\varepsilon_r k_B T} \tag{6.6.1}$$

Considering the Bjerrum length, l_B, a length in which coulombic interaction between point source point elementary charges (e) are equivalent to thermal energy ($k_B T$) for a given dielectric medium ($\varepsilon_o\varepsilon_r$), can be calculated using Eq (6.6.1). We used this length scale in Chapter 2 and 3 in the treatment of ionic interactions in bulk self-assembly PS-b-PTACCy CN-BCPs, and here we will use the same treatment to gain qualitative insight into the extent of screening provided by each annealing solvent. First, the maximum amount of dielectric screening from each solvent can be calculated using difference in Bjerrum length (Δl_B) between the dry ($l_{B,PTACCy}$) and fully solvated ($l_{B,solvent}$) PTACCy block.

$$\Delta l_B = l_{B,PTACCy} - l_{B,solvent} = \frac{e^2}{4\pi\varepsilon_o k_B T}\left(\frac{1}{\varepsilon_{r,PTACCy}} - \frac{1}{\varepsilon_{r,solvent}}\right) \quad (6.6.2)$$

The calculated change in Bjerrum length for each annealing solvent is provided in Table 6.6.1. This analysis assumes that a fully solvated PTACCy block taken on the ε_r of the annealing solvent and ignores the dielectric heterogeneities.[55,82] Solvents with the largest ε_r provide largest departure from the dry-state PTACCy dielectric medium and are predicted to display the most dramatic changes in CN-BCP self-assembly.

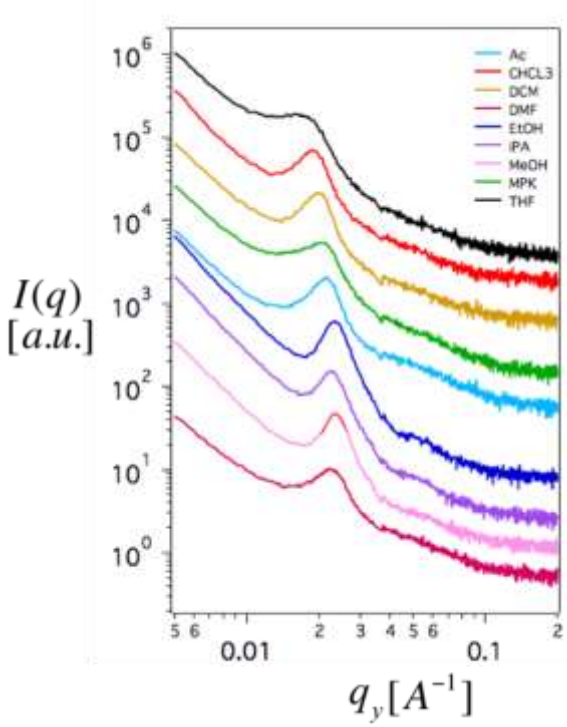

Figure 6.6.1. In-plane linecuts plotting $I(q)$ vs.q_y for PS-b-PTACCy films annealing with a variety of different solvents. The primary bragg reflection for each trace was fit to a gaussian distribution.

Similarly, to the *in-situ* GISAXS experiments discussed previously, 1 mL of solvent was loaded into the annealing chamber and the PS-*b*-PTACCy film structure and thickness was monitored as a function of annealing time. Each experiment was performed on the same PS-*b*-PTACCy film ($h = 40$nm) in the order of increasing annealing solvent dielectric constant. For each annealing experiment, the PS-b-PTACCy film was allowed to achieve an equilibrium swollen

film thickness and then condensed rapidly down using a high overhead N_2 flow rate (0.5 LPM). After complete drying, the film structure was probed using GISAXS a horizontal linecuts was taken at the yoneda peak. Figure 6.6.1 plots the horizontal linecuts intensity $I(q)$ vs. q_y for each annealing solvent. The traces are vertically shifted to highlight the trend of increasing domain spacing. It should be noted that separate PS-*b*-PTACCy films were chosen for a single solvent vapor annealing using the same annealing chamber and a variety of the same annealing solvents (DCM, chloroform, acetone, MeOH, ethanol, iPA) and a similar domain periodicity was found.

Table 6.6.1. A list of all annealing solvents and their dielectric properties.

Solvent	ε_r	$l_B\ [nm]$	$\Delta l_B\ [nm]$
chloroform	4.8	11.6	7.0
tetrahydrofuran	7.5	7.4	11.1
dichloromethane	9.1	6.1	12.5
2-Pentanone	15.5	3.4	15.0
isopropyl alcohol	17.9	3.1	15.5
acetone	20.7	2.9	15.9
ethanol	24.5	2.6	16.0
methanol	32.7	1.7	16.9
dimethyformamide	38.3	1.5	17.1

The primary bragg reflection for each horizontal linecut was fit to a gaussian distribution and the peak position (q^*) and width (Δq) was obtained. The periodicity of the PS-*b*-PTACCy assembly was determined using $d = 2\pi\sqrt{4/3}/q^*$ which takes into account the hexagonal geometry. The relationship was utilized for all solvents except THF, in this case $d = 2\pi/q^*$ was used due to the observed parallel cylinder orientation. Figure 6.6.3 summarized the impact of annealing solvent ε_r on the PS-*b*-PTACCy d and GB/d. Figure 6.6.3 (Left) plots the d *vs.* annealing solvent ε_r and we find a monotonically decreasing relationship. In fact, through simply adjusting the annealing solvent ε_r the PS-*b*-PTACCy d can be modulated by ~ 8 nm which represents 25% of the domain

spacing obtained from the optimal annealing conditions. The data was fit to a $d \sim \varepsilon_r^{\nu}$ power law, shown by the solid red line and we find the following scaling relationship.

$$d \sim \varepsilon_r^{0.53}$$

Interestingly, we do not obtain the expected exponent predicted by equation 6.6.2. If the domain spacing was determined by electrostatic interactions, we would expect $d \sim \varepsilon_r^{-1}$. Therefore, we speculate a different mechanism of dielectric screening of ionic interactions governs the PS-b-PTACCy is present during solvent vapor annealing. In the swollen state we might expect a significate degree of ion dissociation and perhaps these dissociated ions might also contribute to screening ionic interactions. The Debye screen length[146–148] (λ_D) is a parameter to capture this effects and contains a $\lambda_D \sim \varepsilon_r^{-0.5}$ dependence – a relationship akin to what was found for PS-b-PTACCy CN-BCPs.

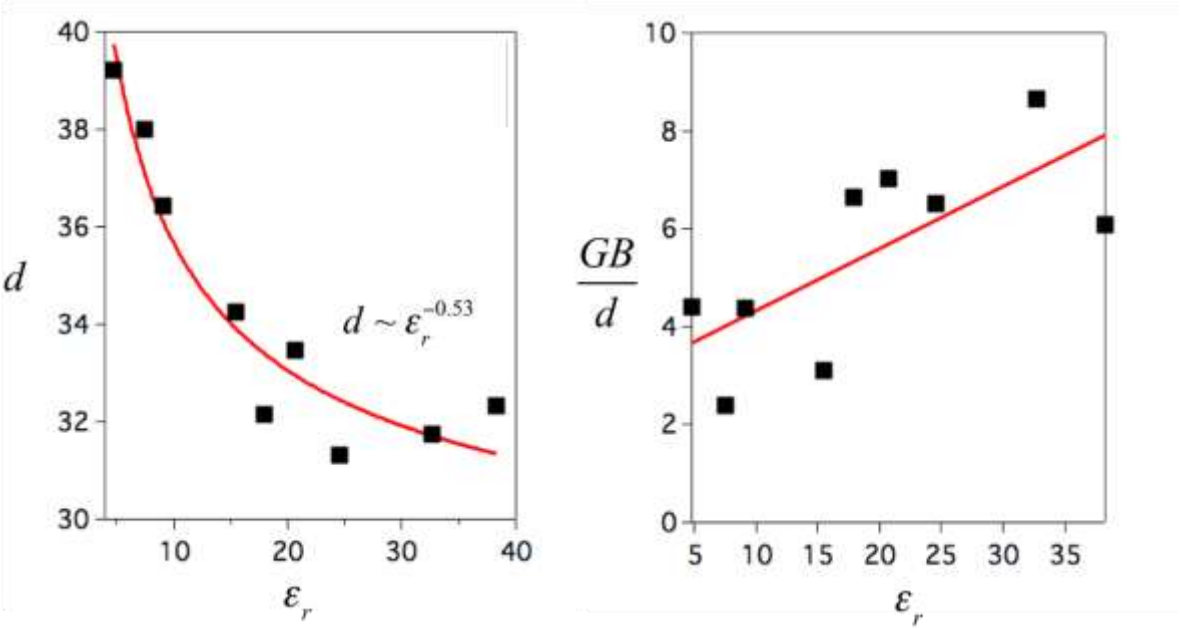

Figure 6.6.3. The impact of annealing solvent dielectric constant on the PS-b-PTACCY thin-film morphology. (Left) the PS-b-PTACCy CN-BCP periodicity dependence on ε_r is plotted. The data set was fit to a power law (solid red line) and the relationship $d \sim \varepsilon_r^{-0.53}$ is observed. (Right) the normalized average grainsize dependence on ε_r is presented. A linear fit (solid red line) is plotted to highlight the increasing grainsize trend with decreasing ε_r.

Next, we explore the impact of the annealing solvent ε_r on GB/d. The GB/d is obtained using the peak width of the primary bragg reflection and Figure 6.3.3 (right) plots GB/d *vs.* annealing solvent ε_r. Unlike d, we find GB/d increases monotonically with increasing annealing solvent ε_r. This result is complimentary to the previous findings. The inhibition of the PTACCy strong ionic interactions allow PTACCy chains to relax (lowering d) and the film morphology more closely approach an equilibrium assembly (larger GB/d). The red line is a linear fit through the data with a y intercept at $y = 0$ and used to elucidate the increasing trend in GB/d with increasing ε_r.

Chapter 7: Conclusion and future work

7.1 Role of ionic interactions in charge – neutral diblock copolymer self-assembly

We provide a comprehensive summary of the CN-BCP literature and present two distinct morphology diagrams with quantitatively different morphological behavior. Conventional, hard cationic CN-BCPs display a morphology diagram that can be adequately describe by the BCP SSL. However, for the large, highly delocalized cationic CN-BCPs (*i.e.* PTACCy and S-Phos) a completely new morphology diagram emerges that cannot be described by any readily accessible theoretical model. We postulate the two separate morphology diagrams are directly related to the order of magnitude differences in ion correlation length scale. This postulate is supported by the dramatically different PTACCy dielectric constant ($\varepsilon_r \sim 2.5 - 3$) compared to that of other hard polyelectrolyte cationic motifs ($\varepsilon_r \sim 12 - 120$). In addition to the CN-BCP morphology, strong ionic interactions have a significant impact on the polyelectrolyte chain conformation. Using a suite of detailed experiments coupled with salt doping experiments show the extended, rod-like PTACCy chain conformation originates from strong electrostatic interactions, and when compared with literature, PS-*b*-PTACCy chains have a more extended conformation. To provide a definitively conclusion for these experimental results we performed thermodynamic calculations and geometric arguments that are discussed in Chapter 3. We believe that these experimental findings will aid the rational design of CN-BCPs that enable the exploration of charge transport through geometrically frustrated ionic matrices.

7.2 Thermodynamic and packing parameter rationalization for electrostatically guided PS-b-PTACCy self-assembly

The PS-*b*-PTACCy bulk morphology diagram presents a description of copolymer microphase segregation that is contradicts the traditional BCP paradigm. The observed large C_N

phase space for CN-BCPs with exceptionally low static dielectric constants suggest that strong ionic interactions play an important role in this process. In the literature, rod-coil diblock copolymers form predominately morphologies with planar-like interfaces[77–79], however for PS-*b*-PTACCy these structures are highly suppressed. To rationalize these conflicting results, we considered the competition between electrostatic repulsons, from polarized ion pairs, and interfacial energy on the interfacial curvature. We find the low PTACCy static dielectric constant drive the stability of a convex interfacial curvature and stabilize the C_N morphology from strong repulsive ionic interactions. Additionally, we adequately described the shifted C_N – LAM transition in the form of a matrix chain frustration parameter, λ, when the impact of a diminishing ϕ_{CN-BCP} on the C_N morphology is considered. As the ϕ_{CN-BCP} approaches C_N – LAM transition, λ approaches unity indicting the PTACCy matrix chains are frustrated to fill space within the structure, and, as a mechanism to alleviate the PTACCy matrix chain frustration, form the LAM morphology. Finally, we present a generalized scaling model derived from molecular surfactant self-assembly principles to capture the CN-BCP morphological behavior. To do this, we defined $l_B \geq l_{head}\sqrt{N_{head}}$ as a criterion to bifurcate the CN-BCP morphology diagram into two regimes. This criterion changes with the polyelectrolyte electrostatic strength (l_B) creating a third axes to the morphology diagram that mapped using the dimensionless parameter, $\Lambda = l_B/b_{head}$. Using knowledge of the CN-BCP physical properties, the generalized packing parameter model was fit to the two different CN-BCPs morphology diagrams presented in chapter 2. The packing parameter model showed excellent agreement with both CN-BCP morphology diagrams yielding reasonable estimations of Λ considering the strength of ionic interactions. Overall, the simplistic nature of the packing parameter model can be used as a guiding light for the design of CN-BCPs with asymmetric morphology diagrams.

7.3 Conductivity Trade-Off in Polymer Electrolyte Separators

We investigated ion transport through a series of hydrated PS-*r*-sPS separators with increasing c_f for a fixed PS molecular weight. We find the separator water volume fraction, ϕ_{H_2O}, plays an intimate role in the ion transport properties of hydrated polymer electrolyte separators. If the ϕ_{H_2O} is considered, increasing $c_{f,swollen}$ increases Ψ^m but reduces in κ. This finding translates into an inverse relationship between $\Psi^m$and κ with increasing ϕ_{H_2O} and is thought to an underlying mechanism behind the $\Psi^m - \kappa$ tradeoff[37]. A summary of the $\Psi^m - \kappa$ tradeoff is presented and the measured PS-*r*-sPS separators are compared to other polymer electrolyte separators in the literature. We find polymer rigidity (*i.e.* backbone T_g) to impact the $\Psi^m - \kappa$ tradeoff and an increase in polymer electrolytes chain rigidity can prevent the separator from achieving ideal Ψ^m. Finally, we utilize dilute solution theory to simulate D_{Li} and t_c^m and find quantitative agreement with the experiential data. At high ϕ_{H_2O} the D_{Li} approaches the Mackie and Meares prediction with exceptionally high κ and mixed salt transference $t_c^m < 1$. To optimize ion transport through swollen polymer separators it is critical to develop structure – property relationships that enable navigation of the $\Psi^m - \kappa$ tradeoff. The concrete understanding of the material properties affecting this trade-off will promote the development of more affordable and efficient sustainable storage devices.

7.5 Two-dimensional self-assembly of PS-b-PTACCy CN-BCPs.

We utilized a modular synthetic strategy to prepare well-defined PS-*b*-PTACCy CN-BCPs that were spun coated into thin films. We investigate the fundamental differences between bulk and thin film PS-*b*-PTACCy self-assembly over the same ϕ_{CN-BCP} and N phase space. The morphology diagram was constructed for a constant PS-b-PTACCy film thickness ($h = 40$nm) and we observe an extended C_N morphology space akin to the bulk PS-*b*-PTACCy morphology

diagram. Interestingly, at this film thickness we do not observe the LAM morphology but instead goes through an order – disorder transition (ODT) at $\phi_{CN-BCP} = 0.4$ determined using GISAXS and AFM. Two separate PS-b-PTACCy CN-BCPs were used to explore the PS-*b*-PTACCy morphology film thickness dependence. Far from the ODT ($\phi_{CN-BCP} > 0.4$) we find the film thickness has an insignificant impact on the PS-b-PTACCy morphology – *i.e.* no variations in structure or domain orientation. However, close to the ODT we find a strong domain orientation thickness dependence which is a hallmark of confinement driven by a finite swollen state film thickness. To our knowledge, this is the first reporting of confinement effects in CN-BCP thin films and we leveraged this phenomenon to reversibly access both C_N domain orientations (perpendicular and parallel to the substrate interface) in a single film.

7.5 *In situ* GISAXS scattering investigation of PS-*b*-PTACCy thin-film self-assembly

We investigate the influence of solvents on the PS-b-PTACCy thin film self-assembly and attempt to decouple these effects from the PS-b-PTACCy morphology. To do this, we prepare PS-*b*-PTACCy thin films and utilized solvent vapor annealing to organize the CN-BCPs into kinetically trapped nonequilibrium structures. Atomic force microscopy coupled with grazing incidence small angle x-ray scattering (GISAXS) was utilized to determine the film morphology and completely map the processing pathway to the final ordered state. We found nonselective and selective solvents provide PS-b-PTACCy thin film with different kinetic processing pathways. The nonselective solvents induce an order – disorder transition with increase solvent volume fraction in the thin film, while the selective solvents drive the CN-BCPs into an ordered swollen stated. These pathways can be thought of as an effective mediation of the segmental interactions causing miscibility between the PS and PTACCy block and an increase in the effective PTACCy volume fraction respectively. Finally, we utilized a variety of annealing solvents spanning a

dielectric range of $\varepsilon_r = 4.8 - 38.3$ to structure PS-*b*-PTACCy thin-films. All annealing solvents produce the same final dry state PS-b-PTACCy morphology (C_N) however the domain periodicity and hexagonal grainsize are significantly affected. As the annealing ε_r increases, the domain periodicity decreases and the hexagonal grainsize increases suggesting that screen electrostatic interactions allows PTACCy chains to relax and the PS-b-PTACCy morphology to approach an equilibrium structure.

References

(1) Kim, S. H.; Hong, K.; Xie, W.; Lee, K. H.; Zhang, S.; Lodge, T. P.; Frisbie, C. D. *Adv. Mater.* **2013**, No. 25, 1822–1846.

(2) Hickner, M. A. *Materials Today*. Elsevier Ltd 2010, pp 34–41.

(3) Armand, M.; Tarascon, J. *Nature* **2008**, *451* (February), 2–7.

(4) Bouchet, R.; Maria, S.; Meziane, R.; Aboulaich, A.; Lienafa, L.; Bonnet, J.-P.; Phan, T.; Bertin, D.; Gigmes, D.; Devaux, D.; Denoyel, R.; Armand, M. *Nat. Mater.* **2013**, *12* (5), 452–457.

(5) Hallinan, D. T.; Balsara, N. P. *Annu. Rev. Mater. Res* **2013**, *43*, 503–525.

(6) Lodge, T. P. *Science (80-.).* **2008**, *321*, 4–6.

(7) Schulze, M. W.; McIntosh, L. D.; Hillmyer, M. A.; Lodge, T. P. *Nano Lett.* **2014**, *14* (1), 122–126.

(8) Timachova, K.; Villaluenga, I.; Cirrincione, L.; Gobet, M.; Bhattacharya, R.; Jiang, X.; Newman, J.; Madsen, L. A.; Greenbaum, S. G.; Balsara, N. P. **2018**.

(9) Timachova, K.; Watanabe, H.; Balsara, N. P. *Macromolecules* **2015**, *48* (21), 7882–7888.

(10) Chintapalli, M.; Chen, X. C.; Thelen, J. L.; Teran, A. A.; Wang, X.; Garetz, B. A.; Balsara, N. P. *Macromolecules* **2014**, *47* (15), 5424–5431.

(11) Fustin, C. A.; Guillet, P.; Schubert, U. S.; Gohy, J. F. *Adv. Mater.* **2007**, *19* (13), 1665–1673.

(12) Whittell, G. R.; Manners, I. *Adv. Mater.* **2007**, *19* (21), 3439–3468.

(13) Kulbaba, K.; Manners, I. *Macromol. Rapid Commun.* **2001**, *22* (10), 711–724.

(14) Rider, D. A.; Cavicchi, K. A.; Vanderark, L.; Russell, T. P.; Manners, I. *Macromolecules* **2007**, *40* (10), 3790–3796.

(15) Li, J.; Zhao, Y.; Tan, H. S.; Guo, Y.; Di, C. A.; Yu, G.; Liu, Y.; Lin, M.; Lim, S. H.; Zhou, Y.; Su, H.; Ong, B. S. *Sci. Rep.* **2012**, *2*, 1–9.

(16) Loo, W. S.; Galluzzo, M. D.; Li, X.; Maslyn, J. A.; Oh, H. J.; Mongcopa, K. I.; Zhu, C.; Wang, A. A.; Wang, X.; Garetz, B. A.; Balsara, N. P. *J. Phys. Chem. B* **2018**, *122* (33), 8065–8074.

(17) Sing, C. E.; Zwanikken, J. W.; Olvera de la Cruz, M. *Nat. Mater.* **2014**, *13* (7), 694–698.

(18) Bandar, J. S.; Tanaset, A.; Lambert, T. H. *Chem. - A Eur. J.* **2015**, *21* (20), 7365–7368.

(19) Wallace, A. J.; Jayasinghe, C. D.; Polson, M. I. J.; Curnow, O. J.; Crittenden, D. L. *J. Am. Chem. Soc.* **2015**, *137* (49), 15528–15532.

(20) Montoto, E. C.; Cao, Y.; Hernández-Burgos, K.; Sevov, C. S.; Braten, M. N.; Helms, B. A.; Moore, J. S.; Rodríguez-López, J. *Macromolecules* **2018**, *51* (10), 3539–3546.

(21) Freyer, J. L.; Brucks, S. D.; Gobieski, G. S.; Russell, S. T.; Yozwiak, C. E.; Sun, M.; Chen, Z.; Jiang, Y.; Bandar, J. S.; Stockwell, B. R.; Lambert, T. H.; Campos, L. M. *Angew. Chemie - Int. Ed.* **2016**, *55* (40), 12382–12386.

(22) Jiang, Y.; Freyer, J. L.; Cotanda, P.; Brucks, S. D.; Killops, K. L.; Bandar, J. S.; Torsitano, C.; Balsara, N. P.; Lambert, T. H.; Campos, L. M. *Nat. Commun.* **2015**, *6*, 5950.

(23) Armand, M.; Endres, F.; MacFarlane, D. R.; Ohno, H.; Scrosati, B. *Nat. Mater.* **2009**, *8* (8), 621–629.

(24) Green, M. D.; Choi, J. H.; Winey, K. I.; Long, T. E. *Macromolecules* **2012**, *45* (11), 4749–4757.

(25) Choi, J. H.; Ye, Y.; Elabd, Y. A.; Winey, K. I. *Macromolecules* **2013**, *46* (13), 5290–5300.

(26) Elabd, Y. A.; Hickner, M. A. *Macromolecules* **2011**, *44* (1), 1–11.

(27) Weber, R. L.; Ye, Y.; Schmitt, A. L.; Banik, S. M.; Elabd, Y. A.; Mahanthappa, M. K. *Macromolecules* **2011**, *44* (14), 5727–5735.

(28) Chintapalli, M.; Timachova, K.; Olson, K. R.; Mecham, S. J.; Devaux, D.; Desimone, J. M.; Balsara, N. P. *Macromolecules* **2016**, *49* (9), 3508–3515.

(29) Gomez, E. D.; Panday, A.; Feng, E. H.; Chen, V.; Stone, G. M.; Minor, A. M.; Kisielowski, C.; Downing, K. H.; Borodin, O.; Smith, G. D.; Balsara, N. P. *Nano Lett.* **2009**, *9* (3), 1212–1216.

(30) Panday, A.; Mullin, S.; Gomez, E. D.; Wanakule, N.; Chen, V. L.; Hexemer, A.; Pople, J.; Balsara, N. P. *Macromolecules* **2009**, *42* (13), 4632–4637.

(31) Logan, B. E.; Elimelech, M. *Nature*. 2012, pp 313–319.

(32) Długołe, P.; Gambier, A.; Wessling, M. **2009**, *43* (17), 6888–6894.

(33) Arora, P.; Zhang, Z. *Chem. Rev* **2004**, *104* (10), 4419–4462.

(34) Dunn, B.; Kamath, H.; Tarascon, J. M. *Science*. 2011, pp 928–935.

(35) Tanaka, M.; Fukasawa, K.; Nishino, E.; Yamaguchi, S.; Yamada, K.; Tanaka, H.; Bae, B.; Miyatake, K.; Watanabe, M. *J. Am. Chem. Soc.* **2011**, *133*, 10646–10654.

(36) Tanaka, Y. *Desalination* **2012**, *301*, 10–25.

(37) Geise, G. M.; Hickner, M. A.; Logan, B. E. *ACS Appl. Mater. Interfaces* **2013**, *5* (20), 10294–10301.

(38) Wang, Z.; Wang, D.; Jin, J. *Macromolecules* **2014**, *47* (21), 7477–7483.

(39) Chung, T. S.; Jiang, L. Y.; Li, Y.; Kulprathipanja, S. *Prog. Polym. Sci.* **2007**, *32* (4), 483–507.

(40) Sanders, D. F.; Smith, Z. P.; Guo, R.; Robeson, L. M.; McGrath, J. E.; Paul, D. R.; Freeman, B. D. *Polym. (United Kingdom)* **2013**, *54* (18), 4729–4761.

(41) Robeson, L. M. *J. Memb. Sci.* **2008**, *320* (1–2), 390–400.

(42) Robeson, L. M.; Burgoyne, W. F.; Langsam, M.; Savoca, a. C.; Tien, C. F. *Polymer (Guildf).* **1994**, *35* (23), 4970–4978.

(43) Robeson, L. M. *J. Memb. Sci.* **1991**, *62* (2), 165–185.

(44) Geise, G. M.; Paul, D. R.; Freeman, B. D. *Prog. Polym. Sci.* **2014**, *39* (1), 1–42.

(45) Chakrabarty, T.; Prakash, S.; Shahi, V. K. *J. Memb. Sci.* **2013**, *428*, 86–94.

(46) Hosseini, S. M.; Madaeni, S. S.; Khodabakhshi, A. R. *Sep. Sci. Technol.* **2012**, *47* (3), 455–462.

(47) Kamcev, J.; Galizia, M.; Benedetti, F. M.; Jang, E. S.; Paul, D. R.; Freeman, B. D.; Manning, G. S. *Phys. Chem. Chem. Phys.* **2016**, *18* (8), 6021–6031.

(48) Kamcev, J.; Paul, D. R.; Manning, G. S.; Freeman, B. D. *ACS Appl. Mater. Interfaces* **2017**, *9* (4), 4044–4056.

(49) Fan, H.; Yin, N. *J. Memb. Sci.* **2019**, *573* (October 2018), 668–681.

(50) Kim, S. A.; Jeong, K.; Yethiraj, A.; Mahanthappa, M. K. **2017**, *114* (16), 4072–4077.

(51) Rubatat, L.; Li, C.; Nyka, A. **2008**, *41* (21), 8130–8137.

(52) Moore, H. D.; Saito, T.; Hickner, M. A. *J. Mater. Chem.* **2010**, *20* (30), 6316–6321.

(53) Guler, E.; Zhang, Y.; Saakes, M.; Nijmeijer, K. *ChemSusChem* **2012**, *5*, 2262–2270.

(54) Ma, B.; Nguyen, T. D.; Pryamitsyn, V. A.; De La Cruz, M. O. *ACS Nano* **2018**, *12*, 2311–2318.

(55) Jadhao, V.; Solis, F. J.; Olvera De La Cruz, M. *J. Chem. Phys.* **2013**, *138* (5), 054119.

(56) Yuan, J.; Antila, H. S.; Luijten, E. *ACS Macro Lett.* **2019**, *8* (2), 183–187.

(57) Chu, W.; Qin, J.; De Pablo, J. J. *Macromolecules* **2018**, *51* (5), 1986–1991.

(58) Geise, G. M.; Falcon, L. P.; Freeman, B. D.; Paul, D. R. *J. Memb. Sci.* **2012**, *423–424*,

195–208.

(59) Elabd, Y. A.; Napadensky, E. *Polymer (Guildf).* **2004**, *45* (9), 3037–3043.

(60) Moore, H. D.; Hickner, M. A. **2010**, 6316–6321.

(61) Rubatat, L.; Li, C.; Nyka, A. **2008**, 8130–8137.

(62) Klein, R. J.; Zhang, S.; Dou, S.; Jones, B. H.; Colby, R. H.; Runt, J. *J. Chem. Phys.* **2006**, *124* (14), 144903.

(63) Griffin, P. J.; Freyer, J. L.; Han, N.; Geller, N.; Yin, X.; Gheewala, C. D.; Lambert, T. H.; Campos, L. M.; Winey, K. I. *Macromolecules* **2018**, *51* (5), 1681–1687.

(64) Harris, M. A.; Heres, M. F.; Coote, J.; Wenda, A.; Strehmel, V.; Stein, G. E.; Sangoro, J. *Macromolecules* **2018**, *51* (9), 3477–3486.

(65) Choi, U. H.; Ye, Y.; Salas, D.; Cruz, D.; Liu, W.; Winey, K. I.; Elabd, Y. A.; Runt, J.; Colby, R. H. *Macromolecules* **2014**, No. 47, 777–790.

(66) Choi, U. H.; Mittal, A.; Price, T. L.; Gibson, H. W.; Runt, J.; Colby, R. H. *Macromolecules* **2013**, *46* (3), 1175–1186.

(67) Choi, U. H.; Lee, M.; Wang, S.; Liu, W.; Winey, K. I.; Gibson, H. W.; Colby, R. H. *Macromolecules* **2012**, *45* (9), 3974–3985.

(68) Choi, U. H.; Mittal, A.; Price, T. L.; Gibson, H. W.; Runt, J.; Colby, R. H. *Macromolecules* **2013**, *46* (3), 1175–1186.

(69) Bates, F. S.; Fredrickson, G. H. *Annu. Rev. Phys. Chem.* **1990**, *41* (1), 525–557.

(70) Zhang, W.; Liu, Y.; Jackson, A. C.; Savage, A. M.; Ertem, S. P.; Tsai, T.; Seifert, S.; Beyer, F. L.; Liberatore, M. W.; Herring, A. M.; Coughlin, E. B. *Macromolecules* **2016**, *49*, 4714–4722.

(71) Scalfani, V. F.; Wiesenauer, E. F.; Ekblad, J. R.; Edwards, J. P.; Gin, D. L.; Bailey, T. S.

Macromolecules **2012**, *45* (10), 4263–4276.

(72) Sudre, G.; Inceoglu, S.; Cotanda, P.; Balsara, N. P. *Macromolecules* **2013**, *46*, 1519–1527.

(73) Cotanda, P.; Sudre, G.; Modestino, M. A.; Chen, X. C.; Balsara, N. P. *Macromolecules* **2014**, *47* (21), 7540–7547.

(74) Park, M. J.; Balsara, N. P. *Macromolecules*. 2008, pp 3678–3687.

(75) Goswami, M.; Kumar, S. K.; Bhattacharya, A.; Douglas, J. F. *Macromolecules* **2007**, *40* (12), 4113–4118.

(76) Knychała, P.; Banaszak, M.; Balsara, N. P. *Macromolecules* **2014**, *47* (7), 2529–2535.

(77) Chen, J. T.; Thomas, E. L. .; Ober, C. K. .; Mao, G. *Science (80-.).* **1996**, *273*, 343–346.

(78) Olsen, B. D.; Segalman, R. A. *Macromolecules* **2005**, *38* (24), 10127–10137.

(79) Olsen, B. D.; Segalman, R. A. *Macromolecules* **2006**, *39* (20), 7078–7083.

(80) Olsen, B. D.; Segalman, R. A. *Macromolecules* **2007**, *40* (19), 6922–6929.

(81) Tenneti, K. K.; Chen, X.; Li, C. Y.; Tu, Y.; Wan, X.; Zhou, Q.; Sics, I.; Hsiao, B. S. *J. Am. Chem. Soc.* **2005**, No. 14, 15481–15490.

(82) Kwon, H. K.; Ma, B.; Olvera De La Cruz, M. *Macromolecules* **2019**, *52* (2), 535–546.

(83) Wu, H.; Li, H.; Solis, F. J.; Olvera De La Cruz, M.; Luijten, E. *J. Chem. Phys.* **2018**, *149* (16), 164701.

(84) Wang, Z.-G. *J. Phys. Chem. B* **2008**, *112* (50), 16205–16213.

(85) Helfand, E.; Sapse, A. M.; Helfand, E.; Sapse, A. M. **1975**, *1327* (62).

(86) Helfand, E.; Tagami, Y. *J. Chem. Phys.* **1972**, *56* (7), 3592–3601.

(87) Teran, A. A.; Balsara, N. P. *J. Phys. Chemisry B* **2014**, *118*, 4–7.

(88) Kennemur, J. G.; Yao, L.; Bates, F. S.; Hillmyer, M. A. *Macromolecules* **2014**, *47* (4), 1411–1418.

(89) Cushen, J. D.; Otsuka, I.; Bates, C. M.; Halila, S.; Fort, S.; Rochas, C.; Easley, J. A.; Rausch, E. L.; Thio, A.; Borsali, R.; Willson, C. G.; Ellison, C. J. *ACS Nano* **2012**, *6* (4), 3424–3433.

(90) Zha, W.; Han, C. D.; Lee, D. H.; Han, S. H.; Kim, J. K.; Kang, J. H.; Park, C. *Macromolecules* **2007**, *40* (6), 2109–2119.

(91) Sinturel, C.; Bates, F. S.; Hillmyer, M. A. *ACS Macro Lett.* **2015**, *4* (9), 1044–1050.

(92) Wanakule, N. S.; Virgili, J. M.; Teran, A. A.; Wang, Z. G.; Balsara, N. P. *Macromolecules* **2010**, *43* (19), 8282–8289.

(93) Israelachvili, J. *Colloids Surfaces A Physicochem. Eng. Asp.* **1994**, *91* (94), 1–8.

(94) Nagarajan, R. *Langmuir* **2002**, No. 18, 31–38.

(95) Nagarajan, R. *Adv. Colloid Interface Sci.* **2017**, *244*, 113–123.

(96) Tan, N. C. B.; Liu, X.; Briber, R. M. *Polymer (Guildf).* **1995**, *36* (10), 1969–1973.

(97) Zawodzinski, T. A.; Derouin, C.; Radzinski, S.; Sherman, R. J.; Smith, V. T.; Springer, T. E.; Gottesfeld, S. *J. Electrochem. Soc.* **1993**, *140* (4).

(98) Geise, G. M.; Freeman, B. D.; Paul, D. R. *J. Memb. Sci.* **2013**, *427*, 186–196.

(99) Vardner, J. T.; Ling, T.; Russell, S. T.; Perakis, A. M.; He, Y.; Brady, N. W.; Kumar, S. K.; West, A. C. *J. Electrochem. Soc.* **2017**, *164* (13), 2940–2947.

(100) Geise, M.; Willis, C. L.; Doherty, C. M.; Hill, A. J.; Bastow, T. J.; Ford, J.; Winey, K. I.; Freeman, B. D.; Paul, D. R. *Ind. Eng. Chem. Res.* **2013**, No. 52, 1056–1068.

(101) Kim, O.; Kim, H.; Choi, U. H.; Park, M. J. *Nat. Commun.* **2016**, *7*, 1–8.

(102) Zugmann, S.; Fleischmann, M.; Amereller, M.; Gschwind, R. M.; Wiemhöfer, H. D.; Gores, H. J. *Electrochim. Acta* **2011**, *56* (11), 3926–3933.

(103) Walls, H. J.; Zawodzinski, T. A. *Electrochem. Solid-State Lett.* **2000**, *3* (7), 321–324.

(104) Dai, H. L.; Sanderson, S.; Davey, J.; Uribe, F.; Zawodzinski, T. A. In *PROCEEDINGS OF THE SYMPOSIUM ON LITHIUM POLYMER BATTERIES*; ELECTROCHEMICAL SOCIETY INC, 1997; pp 111–120.

(105) Vardner, J. T.; Edziah, J.-J. S.; West, A. C. *J. Electrochem. Soc.* **2019**, *166* (6), A848–A855.

(106) Doughty, H. W. *J. Am. Chem. Soc.* **1924**, *46*, 2707–2709.

(107) Güler, E.; Elizen, R.; Vermaas, D. A.; Saakes, M.; Nijmeijer, K. *J. Memb. Sci.* **2013**, *446*, 266–276.

(108) Vrentas, J. S.; Duda, J. L. *J. Polym. Sci. Polym. Phys. Ed.* **1979**, *17* (6), 1085–1096.

(109) Vrentas, J. S.; Duda, J. L.; Ling, H. C. *J. Memb. Sci.* **1989**, *40* (1), 101–107.

(110) Macinnes, D. A.; Longsworth, L. G. *Chem. Rev.* **1932**, *11* (2), 171–230.

(111) Kidd, B. E.; Forbey, S. J.; Steuber, F. W.; Moore, R. B.; Madsen, L. A. **2015**.

(112) Hou, J.; Zhang, Z.; Madsen, L. A. **2011**, 4576–4582.

(113) Mackie, J. S.; Meares, P. *Proc. R. Soc. London, Ser. A* **1955**, *232* (1191), 498–509.

(114) Kamcev, J.; Paul, D. R.; Manning, G. S.; Freeman, B. D. *Macromolecules* **2018**, *51* (15), 5519–5529.

(115) Bang, J.; Kim, B. J.; Stein, G. E.; Russell, T. P.; Li, X.; Wang, J.; Kramer, E. J.; Hawker, C. J. *Macromolecules* **2007**, *40* (19), 7019–7025.

(116) Xu, T.; Goldbach, J. T.; Misner, M. J.; Kim, S.; Gibaud, A.; Gang, O.; Ocko, B.; Guarini, K. W.; Black, C. T.; Hawker, C. J.; Russell, T. P. *Macromolecules* **2004**, *37* (8), 2972–2977.

(117) Segalman, R. A.; Hexemer, A.; Hayward, R. C.; Kramer, E. J. *Macromolecules* **2003**, *36* (9), 3272–3288.

(118) Segalman, R. A.; Hexemer, A.; Kramer, E. J. *Phys. Rev. Lett.* **2003**, *91* (19), 196101.

(119) Segalman, R. A. *Mater. Sci. Eng. R Reports* **2005**, *48* (6), 191–226.

(120) Kawasaki, T.; Araki, T.; Tanaka, H. *Phys. Rev. Lett.* **2007**, *99* (21), 2–5.

(121) Sinturel, C.; Morris, M.; Hillmyer, M. a. *Macromolecules* **2013**, *45*, 1562–1569.

(122) Phillip, W. A.; Hillmyer, M. A.; Cussler, E. L. *Macromolecules* **2010**, *43* (18), 7763–7770.

(123) Gu, X.; Gunkel, I.; Hexemer, A.; Russell, T. P. *Macromolecules* **2016**, *49* (9), 3373–3381.

(124) Cavicchi, K. A.; Russell, T. P. *Macromolecules* **2007**, *40* (4), 1181–1186.

(125) Cavicchi, K. A.; Berthiaume, K. J.; Russell, T. P. *Polymer (Guildf).* **2005**, *46* (25), 11635–11639.

(126) Ham, S.; Shin, C.; Kim, E.; Ryu, D. Y.; Jeong, U.; Russell, T. P.; Hawker, C. J. *Macromolecules* **2008**, *41* (17), 6431–6437.

(127) Kellogg, G. J.; Walton, D. G.; Mayes, A. M.; Lambooy, P.; Russell, T. P.; Gallagher, P. D.; Satija, S. K. *Phys. Rev. Lett.* **1996**, *76* (14), 2503–2506.

(128) Russell, T. P.; Lambooy, P.; Kellogg, G. J.; Mayes, A. M. *Phys. B Phys. Condens. Matter* **1995**, *213–214* (C), 22–25.

(129) Morkved, T. L.; Lu, M.; Urbas, a. M.; Ehrichs, E. E.; Jaeger, H. M.; Mansky, P.; Russell, T. P. *Science (80-.).* **1996**, *273* (5277), 931–933.

(130) Thurn-Albrecht, T.; Derouchey, J.; Russell, T. P.; Jaeger, H. M. *Macromolecules* **2000**, *33* (9), 3250–3253.

(131) Xu, T.; Kim, H. C.; DeRouchey, J.; Seney, C.; Levesque, C.; Martin, P.; Stafford, C. M.; Russell, T. P. *Polymer (Guildf).* **2001**, *42* (21), 9091–9095.

(132) Mansky, P.; Derouchey, J.; Russell, T. P.; Mays, J.; Pitsikalis, M.; Morkved, T.; Jaeger, H.

Society **1998**, *9297* (98), 4399–4401.

(133) Knoll, A.; Horvat, A.; Lyakhova, K. S.; Krausch, G.; Sevink, G. J. A.; Zvelindovsky, A. V; Magerle, R. *Phys. Rev. Lett.* **2002**, *89* (3), 035501.

(134) Boker, A.; Knoll, A.; Elbs, H.; Abetz, V.; Muller, A. H. E.; Krausch, G. *Macromolecules* **2002**, *35* (4), 1319–1325.

(135) Tsarkova, L.; Knoll, A.; Krausch, G.; Magerle, R. *Macromolecules* **2006**, *39* (10), 3608–3615.

(136) Wu, S. *J. Phys. Chem.* **1970**, *74* (3), 632–638.

(137) Gu, X.; Gunkel, I.; Hexemer, A.; Gu, W.; Russell, T. P. *Adv. Mater.* **2014**, *26* (2), 273–281.

(138) Jung, Y. S.; Ross, C. A. *Adv. Mater.* **2009**, *36* (23), 2540–2545.

(139) Gotrik, K. W.; Hannon, a F.; Son, J. G.; Keller, B.; Alexander-Katz, a; Ross, C. a. *ACS Nano* **2012**, *6* (9), 8052–8059.

(140) Park, M. J.; Bang, J.; Harada, T.; Char, K.; Lodge, T. P. *Macromolecules* **2004**, *37* (24), 9064–9075.

(141) Weiss, R.; Schwab, O.; Hampel, F. *Chem. Eur. J.* **1999**, *3* (5).

(142) Bandar, J.; Lambert, T. *Synth.* **2013**, *45* (18), 2485–2498.

(143) Riess, G. *Prog. Polym. Sci.* **2003**, *28* (7), 1107–1170.

(144) Mai, Y.; Eisenberg, A. *Chem. Soc. Rev.* **2012**, *41* (18), 5969–5985.

(145) Jain, S.; Bates, F. S. *Science (80-.).* **2003**, *300* (April), 9–11.

(146) Tadmor, R.; Hernández-Zapata, E.; Chen, N.; Pincus, P.; Israelachvili, J. N. *Macromolecules* **2002**, *35* (6), 2380–2388.

(147) Dobrynin, A. V; Colby, R. H.; Rubinstein, M. *Macromolecules* **1995**, *28* (6), 1859–1871.

(148) Manning, G. S. *J. Chem. Phys.* **1969**, *51* (8), 3249.